ABSTRACT

Title of dissertation: AN EXPERIMENTAL INVESTIGATION OF HYPERSONIC BOUNDARY-LAYER TRANSITION ON SHARP AND BLUNT SLENDER CONES

Richard Edward Kennedy
Doctor of Philosophy, 2019

Dissertation directed by: Associate Professor Stuart Laurence
Department of Aerospace Engineering

Understanding the instabilities leading to the laminar-to-turbulent transition of a hypersonic boundary layer is a key challenge remaining for the design of efficient hypersonic vehicles. In the present study, experiments are performed in three different facilities at freestream Mach numbers between 6 and 14 to characterize instability mechanisms leading to transition on a 7° half-angle slender cone. Second-mode instability waves are visualized using a high-speed schlieren setup with the camera frame rate and spatial resolution optimized to allow individual disturbances to be tracked. In order to facilitate quantitative time-resolved measurements, a method of calibrating the schlieren system and novel image-processing algorithms have been developed. Good agreement is observed between the schlieren measurements, surface pressure measurements, and parabolized stability equation computations of the second-mode most-amplified frequencies and N factors. The high-frequency-resolution schlieren signals enable a bispectral analysis that reveals phase locking of

higher harmonic content leading to nonlinear wave development. Individual disturbances are characterized using the schlieren wall-normal information not available from surface measurements.

Experiments are also performed to investigate the effect of nose-tip bluntness. For moderate to large bluntness nose tips, second-mode instability waves are no longer visible, and elongated structures associated with nonmodal growth appear in the visualizations. The nonmodal features exhibit strong content between the boundary-layer and entropy-layer edges and are steeply inclined downstream. Simultaneously acquired surface pressure measurements reveal high-frequency pressure oscillations typical of second-mode instability waves associated with the trailing edge of the nonmodal features.

AN EXPERIMENTAL INVESTIGATION OF HYPERSONIC BOUNDARY-LAYER TRANSITION ON SHARP AND BLUNT SLENDER CONES

by

Richard Edward Kennedy

Dissertation submitted to the Faculty of the Graduate School of the
University of Maryland, College Park in partial fulfillment
of the requirements for the degree of
Doctor of Philosophy
2019

Advisory Committee:
Professor Stuart Laurence, Chair/Advisor
Professor James Baeder
Professor Christopher Cadou
Professor Johan Larsson, Dean's Representative
Professor Kenneth Yu

Acknowledgments

I would first like to thank my advisor, Professor Stuart Laurence, for giving me the opportunity to work on an exciting and fulfilling research project. I am grateful for his unwavering support, guidance, and extreme patience, which have been invaluable to my development as a researcher. I would also like to thank Professors Christopher Cadou, Johan Larsson, James Baeder, and Kenneth Yu for serving on my committee.

I was very fortunate to collaborate with multiple research groups, and the success of this work hinged on support from many people within the greater hypersonics community. Dr. Eric Marineau served as a mentor and subject-matter expert during the experimental campaigns at AEDC Tunnel 9, which would not have been a success without the help of Mike Smith, who patiently taught me the minutia of the optics hardware. The collaboration with Drs. Joe Jewell, Matt Borg, and Roger Kimmel was critical to the success of multiple experimental campaigns at the Air Force Research Lab.

I am grateful for both the technical and personal support afforded to me by my labmates from the High-Speed Aerodynamics and Propulsion Lab at UMD. I am equally indebted to my friends and colleagues at Caltech and École Polytechnique. I am particularly grateful for the friendship of Ryan McMullen, who not only helped me survive the first year at GALCIT, but also helped me navigate the challenges associated with living in France, including, but not limited to, the gym limiting use of their single barbell to 10 A.M. – 12 P.M. on Saturdays. My time at SUNY

Buffalo was the perfect blend of academic rigor and fun, and my success was in large part from my friends. Additional thanks to my undergraduate research advisor, Professor Matthew Ringuette, for introducing me to experimental fluid mechanics. The Duanesburg crew has encouraged me from New York throughout the entire process, and I am thankful to have such old friends.

Obviously none of this would have been possible without the love and support of my family, especially my parents. Thank you for always encouraging me without pushing me, and always having a big meal ready for me when I come home. Finally, a special thank you to Amelia for supporting me throughout my time at UMD. If I had gotten nothing else out of my sinuous graduate school experience, it all would have still been worth it to meet you. I look forward to our future together.

Financial support was provided by a National Defense Science and Engineering Graduate Fellowship sponsored by the Air Force Office of Scientific Research, and an Ann G. Wylie Semester Dissertation Fellowship through the University of Maryland Graduate School.

Table of Contents

List of Tables

List of Figures

List of Abbreviations

Acronyms

AEDC	Arnold Engineering Development Complex
AFRL	Air Force Research Laboratory
AoA	Angle of Attack
BOS	Background-Oriented Schlieren
DNS	Direct Numerical Simulation
FLDI	Focused Laser Differential Interferometer
HRN	High-Reynolds-Number Facility
LST	Linear Stability Theory
LT	Ludwieg Tube
PSD	Power Spectral Density
PSE	Parabolized Stability Equations
T9	Hypervelocity Tunnel 9
N Factor	Integrated Spatial Amplification Rate

Variables

b^2	Bicoherence
F	Dimensionless Frequency
f_0	Fundamental/Most-Amplified Second-Mode Frequency
h	Enthalpy
M	Mach Number
n	Index of Refraction
R	Stability Reynolds Number
R_N	Nose Radius
Re/m	Freestream Unit Reynolds Number
r	Calibration Lens Vertical Coordinate
s	Streamwise Coordinate
T	Temperature
t	Time
u	Velocity
X_{SW}	Entropy-Layer Swallowing Length
y	Wall-Normal Coordinate
δ	Boundary-Layer Thickness based on u_{99}
ε	Light-Ray Deflection Angle
θ	Structure Angle
κ	Gladstone-Dale Constant

ξ Spanwise Coordinate
ρ Density
σ Standard Deviation

Chapter 1: Introduction

1.1 Motivation

Significant technological progress combined with political pressures has led to a renewed interest in hypersonics in the past decade. One of the highest priority interests coming from the US Department of Defense is the development of a maneuverable air-breathing hypersonic vehicle. By its nature, an air-breathing vehicle must cruise at low enough altitudes to sustain efficient combustion, introducing challenges associated with the higher density gas in this regime compared to the upper atmosphere. Among the most impacted flow properties are drag, skin friction, and notably, the increased heat transfer associated with laminar-to-turbulent transition of the boundary layer on the vehicle surface.

At hypersonic Mach numbers (generally Mach 5 or greater), the transition-to-turbulence of the boundary layer results in an increase of heat transfer of up to five times or greater which, combined with the desired flight duration of tens of minutes, leads to much higher thermal loading. The heat transfer and thermal management therefore become critical design criteria for vehicles operating in this regime. At present, this is dealt with by sizing the thermal protection system over the entire vehicle to meet the safety factors required for turbulent boundary-layer heating rates

at the expense of adding a substantial amount of mass and reducing operational efficiency. This requirement is necessary largely due to the lack of a reliable method for predicting the transition location. Understanding the underlying physics of the transition process, particularly the growth of instabilities within the boundary layer that ultimately lead to transition, is thus critical for the design and development of efficient hypersonic flight vehicles.

1.2 Review of Hypersonic Boundary-Layer Transition Previous Work

The study of laminar-to-turbulent transition dates back to the seminal works of Lord Rayleigh and Osborne Reynolds in the late 1800s, the former developing the theoretical framework around the instability of jets and the latter experimentally recording the behavior of water flow at different flow rates in pipes. Transition in a bounded flow was examined by Tollmien (1929) and Schlichting, who described viscous waves that formed when a disturbance entered the flow and grew to finite amplitudes that, if large enough, would lead to the breakdown to turbulence. The first experimental measurement of these now-termed Tollmien-Schlichting or T-S waves came from Schubauer and Skramstad (1948) who, using hot-wire anemometry, measured harmonic oscillations in a laminar boundary-layer on a flat plate at zero angle of attack in low-speed flow.

Early progress in boundary-layer stability theory relied on a normal-mode approach that considers the asymptotic behavior of disturbances. The analysis begins with decomposing the flow quantities into a basic flow plus an infinitesimal

disturbance. The equations are further simplified by treating the boundary layer as a parallel flow, i.e., the streamlines are everywhere parallel to each other and parallel to any bounding surface. Strictly speaking, growing boundary layers are not parallel flow, but it has been shown that, to leading asymptotic approximation, the parallel-flow assumption is valid (Reshotko, 1976). By formulating the problem this way, the equations admit disturbances of the form

$$Q'(\mathbf{x}, t) = q(y)\exp[i\alpha(x\cos\psi + z\sin\psi - ct)], \tag{1.1}$$

where α is the wavenumber, ψ is the plane wave propagation angle with respect to x, and c is the phase velocity of the disturbance. The computed eigenvalues determine which, if any, disturbances are unstable, and the basic flow is subsequently labeled stable or unstable depending on whether the disturbances grow or decay in time.

Mack (1975) developed a theoretical framework based on the normal-mode approach for hypersonic boundary-layer stability, defining the "second-mode" instability, the dominant higher-frequency mode present for sharp, slender bodies at zero angle of attack when the edge Mach number is sufficiently large. Figure 1.1 presents the first-(T-S waves) and second-mode-instability spatial amplification rates as functions of boundary-layer-edge Mach number. Federov and Tumin (2011) note that Mack's definition of the second mode is inconsistent with conventional usage of the term normal modes; nonetheless, this nomenclature has remained in use in the community and is employed in this thesis. In contrast to T-S waves, the second-mode instability is acoustic in nature, primarily characterized by fluctu-

ations in density, and the second-mode waves possessing the highest amplification rates are two-dimensional. Mack's theory predicted the most-amplified second-mode frequency to be proportional to $1/\delta$ where δ is the local boundary-layer thickness. A number of experimental studies including those from Demetriades (1960, 1977), Kendall (1975), and Stetson and Kimmel (1992) confirmed the existence and behavior of the high-frequency second mode. Following these, parametric studies by Stetson (1983) and Stetson and Kimmel (1992) measured the effects of nose-tip bluntness, angle of attack, wall temperature, freestream unit Reynolds number, and Mach number on hypersonic boundary-layer stability. More recently, Federov (2011) presented a comprehensive overview focusing on the character of second-mode waves developing on slender bodies at zero incidence and the role of boundary-layer receptivity on initiating disturbances on the path to amplification and breakdown to turbulence. A more in-depth examination of individual studies most relevant to this thesis are presented in the following introduction sections.

1.2.1 Instability Measurement Technique Review

Works from Reshotko (1976), Pate (1971), Schneider (2001) and others, have demonstrated that freestream conditions affect transition location; thus, measurements of the second-mode instability waves themselves rather than mean transition-location measurements are required for computational validation. The original measurements of Kendall (1975), Demetriades (1960, 1977), and Stetson et al. (1983) were all made using hot-wire anemometry. The technique worked well in resolv-

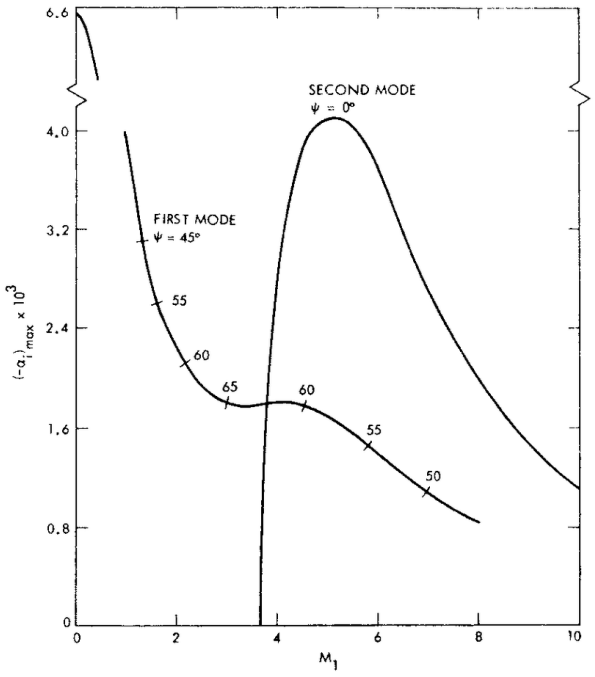

Figure 1.1: "Effect of Mach number on the maximum spatial amplification rate of first and second-mode waves... Insulated wall, wind-tunnel temperatures," Mack (1975).

ing the second-mode fundamental frequency content, but required a specific type of testing facility; namely, the facility needed to be capable of running sufficiently long to allow the probe to be traversed over the test time, and the hot-wires could not be used to make measurements in shock tunnels due to the harsh conditions. Demetriades (1977), in line with the results of Mack, measured the frequency of the instability as $f \propto KU_E/(2\delta)$ where U_E is the boundary-layer edge velocity, K is a constant of proportionality typically in the range $0.6-1.0$, and δ is the boundary-layer thickness.

Recent works have relied on commercially available PCB piezo-electric pressure sensors that can be mounted on the model surface and have a manufacturer-quoted resonant frequency of over 1 MHz. In practice, Ort and Dosch (2019) showed the

mounting method and internal dynamics have significant influence on the sensitivity and frequency response at and above 300 kHz. Fujii et al. (2011), Wagner et al. (2013), Marineau et al. (2014, 2017, 2019), and Casper et al. (2014), among others, successfully used these sensors to measure second-mode instability wave frequencies and growth rates. Fast-response atomic layer thermopile heat-flux gauges developed by Roediger et al. (2009) have been used to measure second-mode frequencies and growth rates, and are the subject of ongoing research and development focused on reducing the sensor footprint to eliminate spatial filtering effects.

Due to the two-dimensional structure and relatively high-frequencies of second-mode waves, optical techniques are well suited for nonintrusive measurements of these disturbances on a slender cone geometry. Potter and Whitfield (1965) recorded the first schlieren images of second-mode instability waves; these appeared as rope-like structures developing in laminar boundary layers. Sample schlieren images are shown in figure 1.2. Recent progress in high-speed electronics, particularly cameras, has led to a renewed interest in using optical techniques for quantitative boundary-layer measurements. The first studies using these techniques implemented a focusing schlieren setup described by Weinstein (1993). VanDercreek et al. (2010) used this system to visualize non-time-resolved images of second-mode waves in the boundary layer of a 7° half-angle slender cone at Mach 10 and employed a related deflectometry setup to measure instability-wave frequencies that showed good agreement with those from a pressure sensor at the same streamwise location. Hofferth et al. (2013) used a similar focused-schlieren-deflectometry technique to measure second-mode waves in a low-disturbance freestream environment. A high signal-to-noise ratio

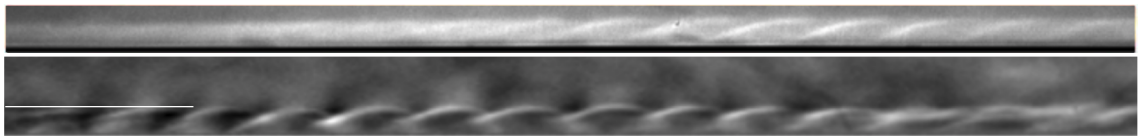

Figure 1.2: Schlieren images of a second-mode wavepacket developing on a cone at Mach 6 (Laurence et al., 2016) (top) and Mach 14 (Kennedy et al., 2017) (bottom). The white line in the bottom image indicates the boundary-layer thickness.

and bandwidth of up to 1 MHz allowed them to measure higher harmonics of the fundamental instability and identify nonlinear origins using a bispectral analysis, but the measurements were limited to one streamwise location per experiment due to the use of a single fiber-optic cable and photodiode system.

Laurence et al. (2012) recognized that, by recording schlieren images at sufficiently high frame rates, they could track individual instability features within the boundary layer and use image-processing techniques to compute properties including the dominant wave frequencies. Following their initial work, Laurence et al. (2014, 2016) built upon the technique by using a pulse-burst laser to record image pairs of second-mode waves with the camera set to a lower frame rate but higher spatial resolution. From these visualizations, they were able to calculate propagation speeds, spatial frequency content, and structure angles for second-mode disturbances. The two-dimensional schlieren images have the added advantage of allowing information extraction at different heights in the boundary layer. Similar visualization experiments were performed by Casper et al. (2016) and Grossir et al. (2014). While these schlieren techniques are reasonably easy to implement, one drawback is that most schlieren systems lack a calibration and require integrating the density-gradient disturbance information to acquire the density disturbance. As an alternative, re-

searchers have begun using focused laser differential interferometry (FLDI). The FLDI system provides a direct measurement of density disturbance, and was used by Parziale (2013) and Parziale et al. (2015) to obtain quantitative measurements of instability amplification rates in the T5 hypervelocity shock tunnel at Caltech. Again, however, the technique has limited spatial measurement density and requires a highly precise installation.

1.2.2 Studies on Second-Mode Wave Development

A significant number of stability experiments in blow-down facilities using hot-wire anemometry were performed shortly after the discovery of higher transition modes by Mack. Stetson and Kimmel (1992) combined much of the data and provided a comprehensive overview of the key findings. In all the experiments performed at Mach numbers greater than 5, large-amplitude density fluctuations dominated the transition process and, in line with the theory, instability frequencies were highly tuned to the boundary-layer thickness, decreasing with increasing streamwise location. As shown in figure 1.3, Stetson et al. (1983) observed the most-amplified disturbances had a wavelength of roughly twice the boundary-layer thickness and fluctuation energy was primarily contained within the upper half of the waves. Among the key unexpected findings of the experiments included the identification of a higher harmonic peak in the frequency spectra that was not predicted by the linear stability theory. The harmonic had a frequency of approximately twice the fundamental, and appeared at streamwise locations where the fundamental en-

ergy content had been significantly amplified. Kimmel and Kendall (1991) explored this phenomenon further, performing a bispectral analysis that showed the generation of harmonics to be closely linked to nonlinear wave propagation. Amplification rates computed from the hot-wire measurements agreed well with the linear-stability results in the regime where the nonlinear interactions were not present, but began to deviate shortly after their appearance. Their findings spurred further investigations including those of Chokani (2005), Bountin et al. (2008), and Hofferth et al. (2013), who explored the phenomenon using a variety of measurement techniques in a Mach-6 freestream. In all cases, nonlinear interactions were shown to play a large role in wave growth near the onset of transition, and provided valuable information on energy distribution within the wave. The work of Hofferth et al. (2013) was notable in that, by using a high-bandwidth deflectometry technique, they resolved higher harmonic interactions at $3f_0$ and $4f_0$, frequency content that was previously unidentifiable due to measurement limitations. Kimmel et al. (1996) further elucidated the wave structure by computing the coherence between spanwise displaced hot-wire measurements to reveal the waves had a limited spanwise extent of less than roughly 4δ and decreased with increasing unit Reynolds number.

More recently, Marineau et al. (2019) combined and analyzed data from a series of experiments on a similar 7° half-angle slender, sharp-nose cone geometry in freestreams of Mach 5 – 14. Using wave amplitudes measured by high-speed PCB pressure sensors in 11 different facilities, they showed that second-mode growth rates can be predicted using parabolized stability equations, specifically using computations from the STABL software suite. When scaled using the parameters defined

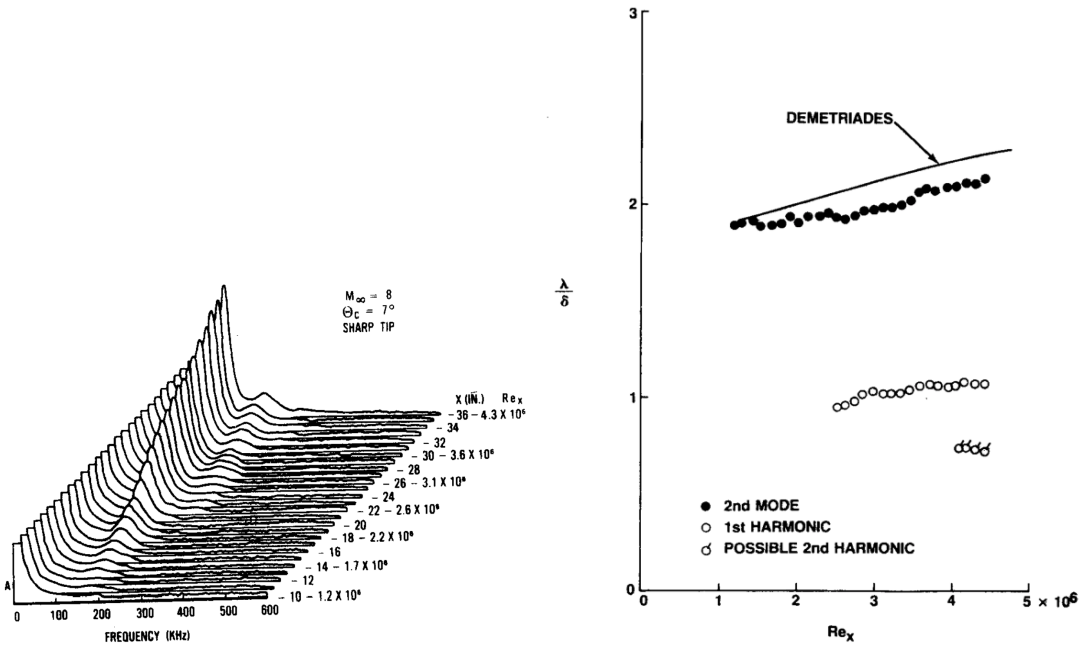

Figure 1.3: Hot wire measurements (Stetson et al., 1983) of fluctuation spectra (left) and fluctuation wavelength (right).

in Stetson et al. (1983), the slope of the maximum integrated amplification rates (N factors) measured by the PCB sensors collapsed onto the growth rate predicted by the PSE solutions. Transition N factors achieved by the waves were shown to increase with increasing unit Reynolds number at each Mach number. Marineau et al. (2019) further showed the initial disturbance amplitude, A_0, to scale inversely to the unit Reynolds number, relating the freestream conditions to the onset of wave development. Experimental confirmation of transition N factors changing as a function of freestream condition was particularly notable as it proved that the use of a single transition N factor as a transition location predictor is inaccurate.

The implementation of new measurement systems discussed in §1.2.1 has also led researchers to focus on characterizing individual disturbances. Experiments by Casper et al. (2014) at Mach 6 examined the pressure footprints of individual nat-

ural and artificially generated disturbances that grew into second-mode instability wavepackets. Nonlinear growth was observed in the wavepackets, and breakdown was observed to begin at the core of the waves where the amplitudes were the largest. High-frequency pressure fluctuations remained present around the core throughout the process. The two-dimensionality of the waves holds throughout the initial growth stages before substantial nonlinear growth and breakdown of the core causes significant three-dimensionality to appear. DNS by Sivasubramanian and Fasel (2014) supported these experimental findings by showing the wavepackets have a two-dimensional pressure footprint that becomes increasingly curved at the edges during the nonlinear growth stages.

Laurence et al. (2016) used their non-intrusive schlieren measurement techniques to characterize individual waves at different stages of development in a Mach 6 and Mach-8 reflected-shock wind tunnel, specifically focusing on using wall-normal information available in the schlieren image data. Wavepacket wall-normal energy distributions revealed the fundamental frequency energy to have a single peak distribution at $y/\delta = 0.7 - 0.75$ and develop a second peak near the boundary-layer edge. The structure angles showed the waves begin pointed upstream before rapidly folding over as they reach the boundary-layer edge, resulting in an overall sickle-like shape. In addition to exploring disturbances in low-enthalpy conditions ($h_0 \approx 3.3\,\mathrm{MJ/kg}$), Laurence et al. (2016) performed experiments at higher enthalpy ($h_0 \approx 11.9\,\mathrm{MJ/kg}$). The notable difference in the high-enthalpy case was large-amplitude disturbance energy located at the wall, and was attributed to a change in the density eigenfunction due to the highly-cooled wall. Parziale et al. (2015), who also recorded

measurements in a high-enthalpy reflected-shock tunnel, noted a similar peak at the wall. Using their FLDI system, they also measured second-mode frequencies and, in line with Laurence et al. (2016), observed the normalized frequencies to be lower than those measured by Demetriades (1977) and Stetson (1983) in cold-flow facilities but in line with the results of Bitter and Shepherd (2015) based on wall-temperature ratio and edge Mach number.

1.2.3 Impact of Nose-Tip Bluntness

Although nose bluntness is recognized to have a dramatic impact on stability, a fairly limited amount of experimental data exist describing the high-frequency instabilities that develop over blunt geometry cases. This is primarily due to the difficulty in generating the freestream conditions capable of causing natural laminar-to-turbulent transition on a blunt geometry, combined with the complex measurement environment. Stetson (1983) performed a number of experiments using surface-mounted thermocouples and pressure sensors to measure the mean transition location on a 8° half-angle cone at zero incidence in a Mach-6 freestream. The cone model used an interchangeable nose tip to test model configurations with nose-tip radii ranging from nominally sharp to 15 mm. The experimental results showed that, as the nose-tip radius is increased, the onset of transition shifts downstream. However, at sufficiently high nose-tip bluntnesses, this trend reverses and the transition location moves upstream with increasing nose-tip bluntness, a process termed transition reversal. Jewell and Kimmel (2016) analyzed the experimental results of

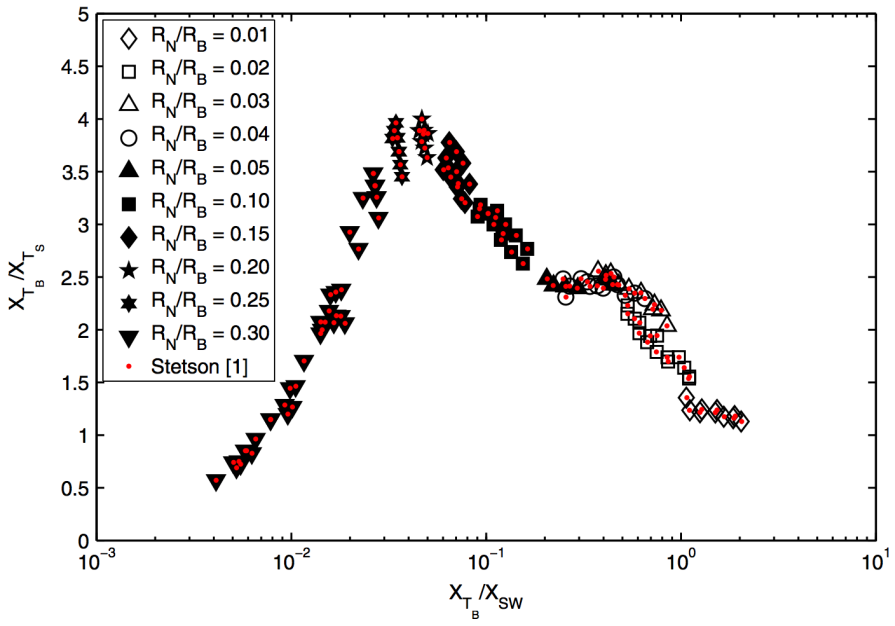

Figure 1.4: "Nose-tip bluntness normalized by swallowing length vs the transition location ratio", Jewell and Kimmel (2016) showing data from Stetson (1983). $X_{\mathrm{T_B}}$ and $X_{\mathrm{T_S}}$ are the streamwise coordinate of transition for the blunt and sharp-nose cones, respectively, and X_{SW} is the computed entropy-layer swallowing length.

Stetson (1983) using the STABL computational fluid dynamics code package (see §4.3). They confirmed the movement of the transition front as shown in figure 1.4, and showed that increasing the nose-tip bluntness and entropy-layer swallowing length results in a monotonic decrease in the N factors associated with the second-mode instability. Oblique modes were shown to not be responsible for the transition-reversal behavior, and thus, the reversal is not explained by linear stability theory. Experimental measurements using high-speed pressure transducers by Marineau et al. (2014) showed a similar suppression of second-mode growth for cases where the entropy-layer swallowing length was downstream of the transition onset location.

Due to the failure of the normal-mode stability theory to predict the exper-

imentally observed behavior, researchers turned to nonmodal stability theory as a potential path for modeling the instability mechanisms. As described by Schmid (2007), nonmodal stability theory considers the full evolution operator (i.e. the response behavior of the governing equations to input variables) allowing the short-term disturbance evolution to be captured. This is in contrast to the normal-mode analysis which, by construct, assumes the disturbances have an exponential time and space dependence and only captures their asymptotic behavior. By making no a priori selection of a time horizon or perturbation shape, the full disturbance behavior can be modeled, including large transient disturbance amplification caused by the superposition of decaying nonorthogonal eigenvectors. These large amplification transients can often dominate the flow dynamics, even when the basic flow is asymptotically stable. Since the disturbance evolution does not assume an exponential form, lower spatial amplification rates are typically observed for features experiencing nonmodal amplification when compared to the exponentially growing second-mode waves. Additionally, use of the full equations also allows for finite amplitude disturbances, including freestream noise, to be accounted for using external forcing terms, whereas only infinitesimal disturbances are admitted in the normal-mode analysis.

To better understand the growth mechanisms present in the blunt-nose geometries, Paredes et al. (2019a) computationally investigated nonmodal-growth mechanisms as a possible cause of the transition-reversal phenomenon. Stationary disturbances initiated within the nose-tip vicinity were found to undergo nonmodal amplification that increased with increasing nose-tip bluntness. These nonmodal-

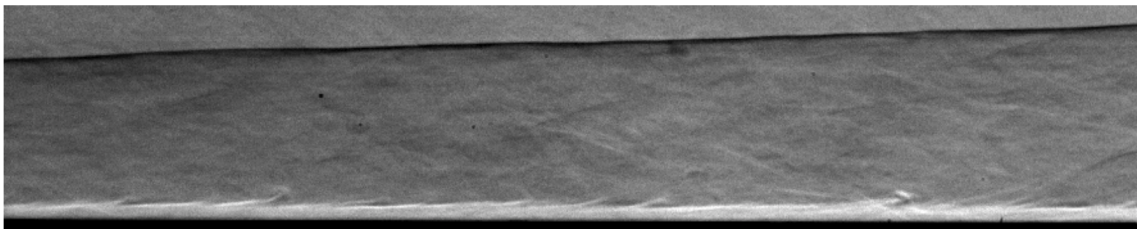

Figure 1.5: Schlieren image of nonmodal features (Grossir et al., 2014).

growth features were significantly amplified while first-mode, second-mode, and entropy-layer modal instability amplification was minimal. Paredes et al. (2019b) showed that, unlike second-mode waves that appear as rope-like structures within the boundary layer, planar and oblique nonmodal-growth features are expected to experience a peak in disturbance magnitude outside the boundary-layer edge. LIF-based schlieren images captured of the boundary layer over a 7° half-angle cone with a 4.75 mm radius nose tip in a Mach-11.8 freestream by Grossir et al. (2014), shown in figure 1.5, captured elongated structures that have content extending out beyond the boundary-layer edge, in qualitative agreement with the computations of Paredes et al. (2019a); however, their visualization system did not have sufficient temporal resolution to capture individual features as they evolved.

1.3 Scope of Current Work

The aim of the present study is to characterize the disturbances associated with boundary-layer transition on a slender body in hypersonic freestreams. Data are collected in three facilities—AEDC Tunnel 9, the AFRL Mach-6 Ludwieg Tube, and the AFRL Mach-6 High-Reynolds-Number wind tunnel—to compare the insta-

bility development in different freestream conditions. A particular highlight is a comprehensive set of experiments performed in AEDC Tunnel 9 at Mach 14, since extremely limited measurements were previously available above Mach 10. A 7° half-angle cone geometry with interchangeable sharp and blunt nose tips is used as the test geometry. In an effort to extend current measurement capabilities, we develop a unique calibrated high-speed schlieren imaging system and image-processing routines to reconstruct time-resolved signals. Particular focus is placed on using the visualizations to compute quantitative characteristics including second-mode-wave N factors and nonlinear interactions involving high-frequency harmonic content. Surface pressure measurements and schlieren visualizations are simultaneously acquired to characterize individual instability features. The work is intended to be a resource for future stability and transition work, and to provide experimental data for computational validation.

In chapter 2 the facilities and test articles are described. In chapter 3, a calibrated schlieren system is presented and characterized. Novel image-processing techniques used to reconstruct time-resolved signals from the schlieren images and post-processing techniques relevant to the unique calibrated schlieren signals are examined in chapter 4. In chapter 5, results from each experimental campaign using the sharp-nose geometry are presented, including both time-averaged and individual disturbance behavior. In chapter 6, we present results acquired using model configurations with a range of finite-radius nose tips. Finally, in chapter 7, we present the major conclusions and the project is summarized.

Chapter 2: Facility and Model

2.1 Facilities

Experiments in the present study were conducted in three facilities: Arnold Engineering Development Complex Hypervelocity Tunnel 9, the Air Force Research Laboratory Mach-6 Ludwieg Tube at Wright-Patterson Air Force Base, and the Air Force Research Laboratory Mach-6 High-Reynolds-Number wind tunnel at Wright-Patterson Air Force Base. Data were collected in multiple facilities to examine boundary-layer transition at a variety of Mach numbers and unit Reynolds numbers that no single facility could produce. The following sections present the basic working principles of each facility and draw attention to their unique capabilities in the context of the present investigation.

2.1.1 AEDC Tunnel 9

AEDC Tunnel 9 is a national-scale blowdown hypersonic wind tunnel located in White Oak, MD. The facility is primarily used for test and evaluation studies. Tunnel 9 is capable of testing at freestream Mach numbers of 7, 8, 10, 14, and 18 with freestream unit Reynolds numbers ranging from 0.177×10^6 to 158.8×10^6 per

meter. The test section has a diameter of 1.5 meters and possesses a system capable of pitching the model at rates of up to 80 degrees per second, allowing the model to experience a large range of flow configurations during a single test. A schematic of the facility is seen in figure 2.1.

Prior to a run, the vacuum sphere, nozzle, and test section are pumped down to a pressure of less than 140 Pa. Nitrogen in vertical gas heaters is compressed and heated to the pressure and temperature required to produce the desired freestream condition. The high and low pressure sides are isolated by a pair of metal diaphragms upstream of the throat. Once the desired reservoir conditions are reached, the diaphragms are burst, causing the test gas to expand into the test cell. During the run time, the stagnation conditions are maintained by pumping cold nitrogen into the heater. Due to the amount of time required to evacuate the 30.5-m diameter vacuum sphere and evaluate the facility between runs, the number of experiments per day is limited to between one and two. Additional information on the facility can be found in Marren and Lafferty (1998).

For the data presented in this study, one experiment was performed with the Mach-10 nozzle installed and five experiments were performed with the Mach-14 nozzle. Unit Reynolds numbers were varied from 1.74×10^6 to 12.10×10^6 per meter by adjusting the reservoir pressure. All runs were performed with stagnation enthalpies of 2 MJ/kg or less. Steady-flow test times range from 0.6 seconds to 3 seconds for the highest to lowest unit-Reynolds-number cases, respectively. Small variations in flow variables can occur over the course of the test time. The extent of this variation is generally less than 2% for the freestream velocity and is accounted

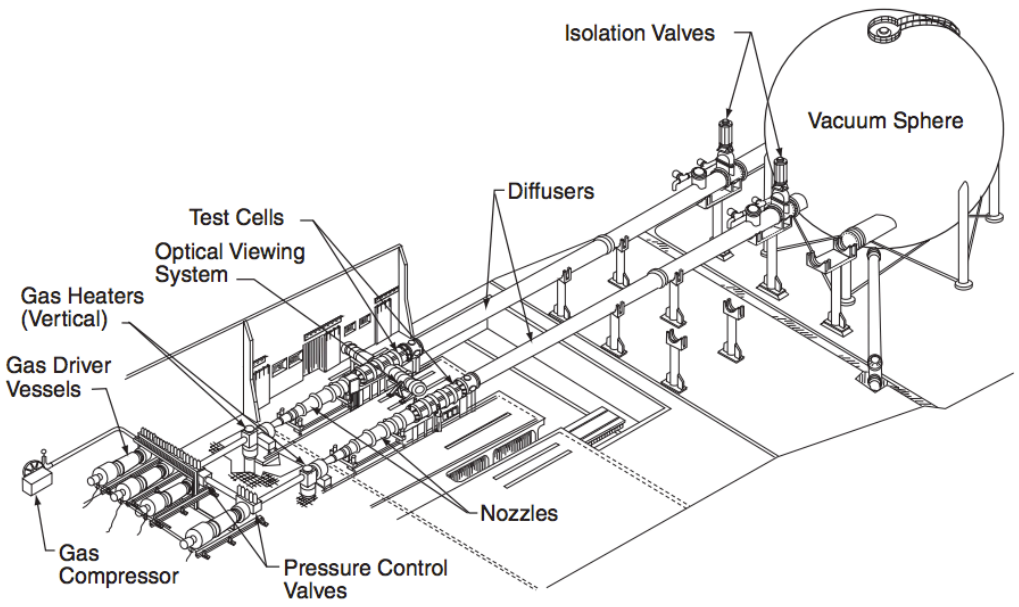

Figure 2.1: Schematic of AEDC Tunnel 9 (Marren and Lafferty, 1998).

for in the measurement acquisition.

2.1.2 AFRL Mach-6 Ludwieg Tube

The Air Force Research Laboratory Mach-6 Ludwieg Tube (LT) is an impulse facility recently constructed by the Aerospace Systems Directorate of the Air Force Research Laboratory in Dayton, OH. It is primarily a research facility designed to provide hands-on access for engineers to conduct basic research in fluid dynamics, instrumentation development and related disciplines. The 0.762-meter diameter nozzle exit generates a free jet that enters a test chamber of approximately 1.27 meters in diameter. The facility is capable of testing at freestream unit Reynolds numbers up to 34.4×10^6 per meter, with a steady-flow test time of approximately 100 ms and a turn-around time of 12 minutes. Air is used as the test gas. A schematic of the facility is shown in figure 2.2.

The driver and driven sections are separated by a fast-acting valve with the option to use a diaphragm for testing low stagnation pressure conditions. For all the experiments in the current study, actuation was achieved using the fast valve. Prior to an experiment, the test section is pumped to a vacuum and the driver section is filled with air heated to 500 K at pressures between 689 kPa and 4 MPa. Once the gas on the driver side reaches the desired conditions, the fast-acting valve is opened, causing an expansion wave train to move upstream in the driver tube. Conditions are constant after the passage of the expansion wave, providing a period of steady stagnation conditions until the wave train reflects from the most upstream end of the driver tube and returns to the region of the nozzle contraction. The stagnation pressure is sufficiently high after the first expansion wave passage to result in an additional period of uniform flow succeeding the initial test period. Figure 2.3 shows the pressure in the driver tube measured during a fast-valve run. About 80 ms of quasi-steady pressure is obtained after the valve-opening transient, and the pressure during this time is reasonably flat, with a drop of about 0.2%. Additional information on tunnel operations and specifications can be found in Kimmel et al. (2017).

In the current investigation, freestream unit Reynolds numbers are set between 4.90×10^6 and 22.71×10^6 per meter for individual runs by adjusting the reservoir pressure between 689 kPa and 3.48 MPa. The freestream Mach number is 6.14, and the freestream temperature and velocity are 54 K and 901 – 904 m/s for all experiments. The reservoir conditions are measured directly and freestream conditions are computed as described in Kimmel et al. (2017).

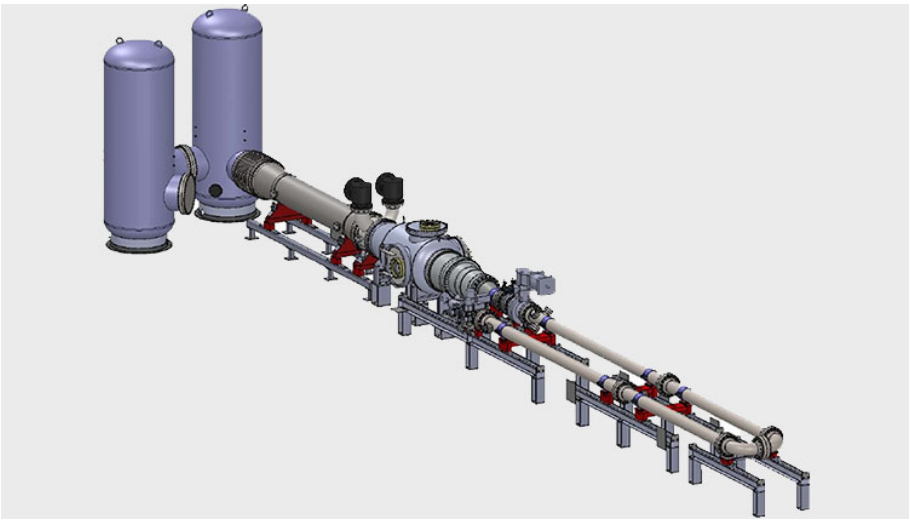

Figure 2.2: Rendering of the AFRL Mach-6 Ludwieg Tube (Kimmel et al., 2017).

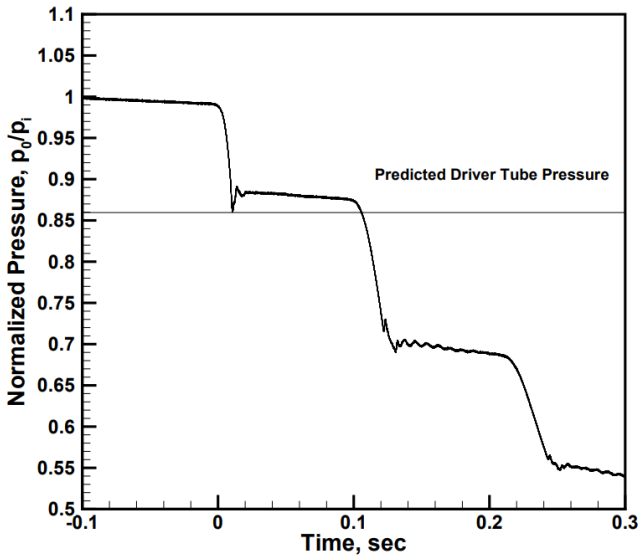

Figure 2.3: Stagnation pressure measured in the driver section during a run in the AFRL LT (Kimmel et al., 2017).

2.1.3 AFRL Mach-6 High-Reynolds-Number Wind Tunnel

The Air Force Research Laboratory Mach-6 High-Reynolds-Number wind tunnel is a blowdown facility that operates at a reservoir temperature of 611 K and a reservoir pressure range of 4.83 to 14.48 MPa, corresponding to unit Reynolds numbers of 30.7×10^6 to 92.1×10^6 per meter. A free-jet test core of approximately 25.4 cm is produced by a contoured axisymmetric nozzle with a physical exit diameter of 31.2 cm (Stetson, 1983). The freestream Mach number, temperature, and velocity are 5.9, 76.7 K, and 1038 m/s, respectively. The air supply allows for run times of 100 s at the maximum reservoir pressure of 14.48 MPa.

The sequence of operation begins with high-pressure air generated by compressors and held in a bottle field being released into the heater vessel. Prior to the initiation of a test, the model is retracted into the bottom of the test cabin. When the heater reaches the desired run stagnation pressure, a valve is opened and flow is established in the wind tunnel. After establishment of steady freestream conditions, the model is injected into the test region and data are recorded. Prior to termination of the test, the model is retracted into the bottom of the test cabin. Injection and retraction times are each approximately two seconds. Additional information on the facility can be found in Fiore and Law (1975). In the present study, data are presented for four experiments performed at reservoir pressures of 4.87 MPa – 8.96 MPa.

2.2 Test Article

A 7° half-angle slender cone is used as the test article for all the experiments in the present investigation. The model geometry was chosen because of its canonical nature and the wealth of experimental and numerical data available for comparison. Two different cone models are used: one for the Tunnel 9 campaign and one for the AFRL campaigns. Significant instrumentation was added to the AFRL cone between the earlier High-Reynolds-Number facility experimental campaign and the Ludwieg Tube campaign. Additionally, the AFRL cone is equipped with interchangeable nose tips of varying bluntness.

2.2.1 Tunnel 9 Model

The Tunnel 9 test article is a 1.550 m long, 7° half-angle slender cone with a sharp nose tip. Figure 2.4 shows the model installed in the test section. The cone was constructed in three sections with base diameters of 0.127 m, 0.254 m, and 0.381 m. The cone is equipped with a variety of flush-mounted surface sensors for measuring boundary-layer instabilities. Fast-response pressure measurements were made using PCB model 132-A31 piezo-electric transducers. Pressure taps provided mean static measurements of the surface pressure, while temperature sensitive paint and thermocouples provided mean heat-transfer measurements from which transition locations were determined. Figure 2.5 shows a flattened view of the surface instrumentation layout. All the data presented in the current study were collected from the windward side, 180°-meridian ray, denoted "N", unless noted otherwise.

Figure 2.4: Cone model installed in Tunnel 9 test section.

Additionally, for the Mach-14 tests, a spanwise array comprising five PCB sensors circumferentially spaced 6.4 mm apart was installed at the downstream location $s = 0.775$ m. The high-frequency pressure fluctuations measured by the PCB sensors are recorded with a HBM Genesis 16t high-speed data system that acquired 14-bit data at 10 MHz. Additional information on the data acquisition and reduction equipment used at Tunnel 9 can be found in Marineau et al. (2017).

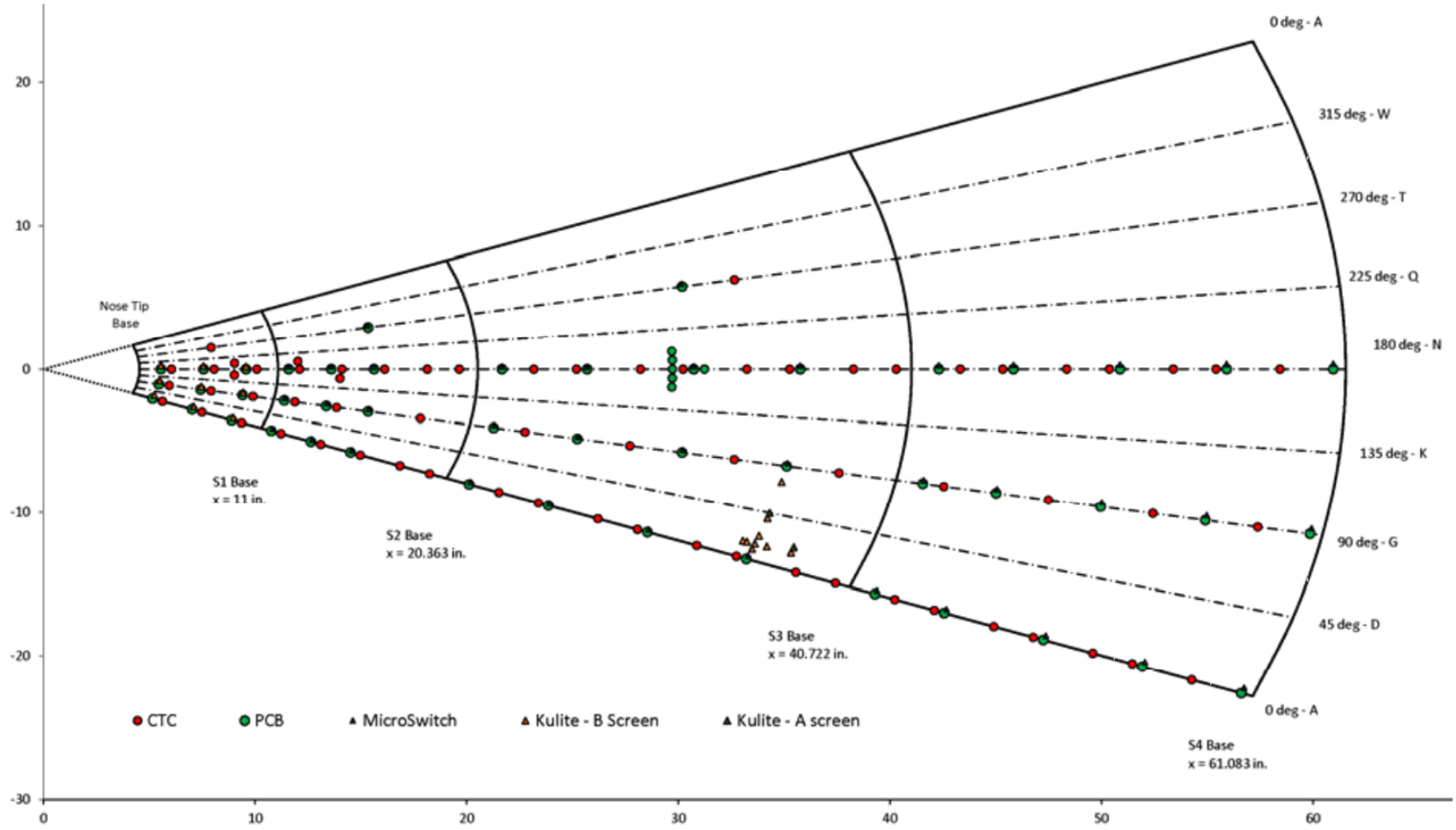

Figure 2.5: Tunnel 9 cone instrumentation layout.

2.2.2 AFRL Model

The AFRL test article is a 7° half-angle, slender cone with an interchangeable nose section. With the sharp nose installed, the cone length is 414 mm (16.3 inches). Five nose tips of different radii ranging from nominally sharp to 5.08 mm were tested and, for consistency, the surface coordinate s used hereinafter refers to the streamwise distance measured from the tip of the sharp-nose configuration. For the High-Reynolds-Number facility experiments, which were chronologically the first set of experiments to occur, the surface instrumentation was limited to coaxial thermocouples capable of measuring mean heat flux. All the data presented in the current study were acquired with the cone installed at zero incidence ($\pm 0.5°$) to the freestream.

Prior to the Ludwieg Tube experiments in March 2018, the cone was instrumented with 8 PCB model 132A and 132B piezo-electric pressure sensors for measuring high-frequency (>11 kHz) pressure fluctuations. As shown in figure 2.6, six of the PCB sensors lie along a single streamwise ray corresponding to the schlieren plane of visualization. The two additional PCB sensors are placed adjacent to the sensor located at $s = 316$ mm and offset in the circumferential direction by 5.715 mm on either side relative to this plane. The three-sensor-wide array allows for measurements of the spanwise extent of pressure disturbances. Prior to the start of all experiments, the model was at room temperature.

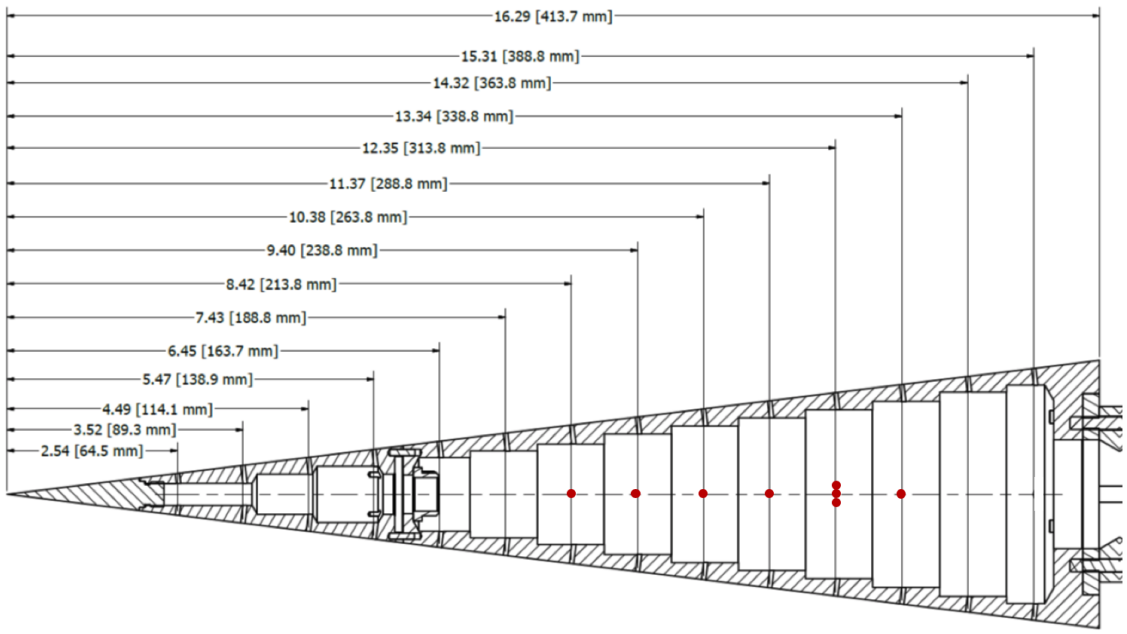

Figure 2.6: AFRL LT cone instrumentation layout. The red dots indicate PCB sensors.

Chapter 3: High-Speed Schlieren Measurement Technique

3.1 Experimental Setup

A conventional Z-type schlieren system, similar to the one shown in figure 3.1, was used to produce the visualizations for each experimental campaign. Illumination was provided by a Cavilux HF pulsed-diode laser that emitted pulses of 20 – 50 ns duration at 810 nm, released from a 1.5 mm diameter fiber-optic cable. The Cavilux HF provides low-coherence light, making it a highly suitable light source for high-speed imaging. Mirrors were used to collimate the light to pass through the test section and refocus the light on the other side, and a knife-edge cutoff placed parallel to the facility floor was used to visualize the density gradients approximately normal to the cone surface. A Phantom v2512 high-speed camera mounted parallel to the cone surface recorded the visualizations, with the exception of the Tunnel 9 Mach-10 images which were recorded with a Phantom v710. Two methods were used to focus the test section image plane into the camera. For the Tunnel 9 experiments where the boundary-layer thickness was 5 – 7 mm, a standard Nikon lens was mounted on the front of the camera. For both AFRL campaigns, in which the boundary layer was significantly thinner, a free-standing biconvex lens with a 1 – 2 m focal length (depending on the required magnification) was used to focus the image into the

camera. The camera frame rate was typically set to be slightly above one half of the fundamental frequency of the second-mode disturbances as predicted by the PSE calculations; this was determined to be an adequate tradeoff between having sufficient pixel density in the boundary layer, the total field of view, and capturing the evolution of a wavepacket in time. The magnification was set to capture $10-15$ pixels across the boundary-layer thickness. Special attention was taken to modify the viewing location with the test conditions in order to visualize the behavior of the waves within the boundary layer from initial onset through to breakdown to turbulence. Further details on the specifications for each experimental setup is provided in §5. For the Tunnel 9 Mach-14 experiments, the setup had the additional constraint that the cone was pitching over the steady test time. To capture the cone in the field of view over the pitch sequence, the vertical extent of the viewing area was increased at the expense of magnification. When possible, the entire set of visualizations captured for a given experimental condition was saved; this resulted in 25,000 – 50,000 images from each AFRL LT experiment and 100,000+ images for each of the Tunnel 9 and AFRL High-Reynolds-Number facility experiments.

3.2 Schlieren Calibration

3.2.1 Introduction

A calibration of the schlieren system was performed prior to each experiment to enable quantitative measurements. Calibration of the system is required due to the nonlinear schlieren response of the light rays generated by the circular light

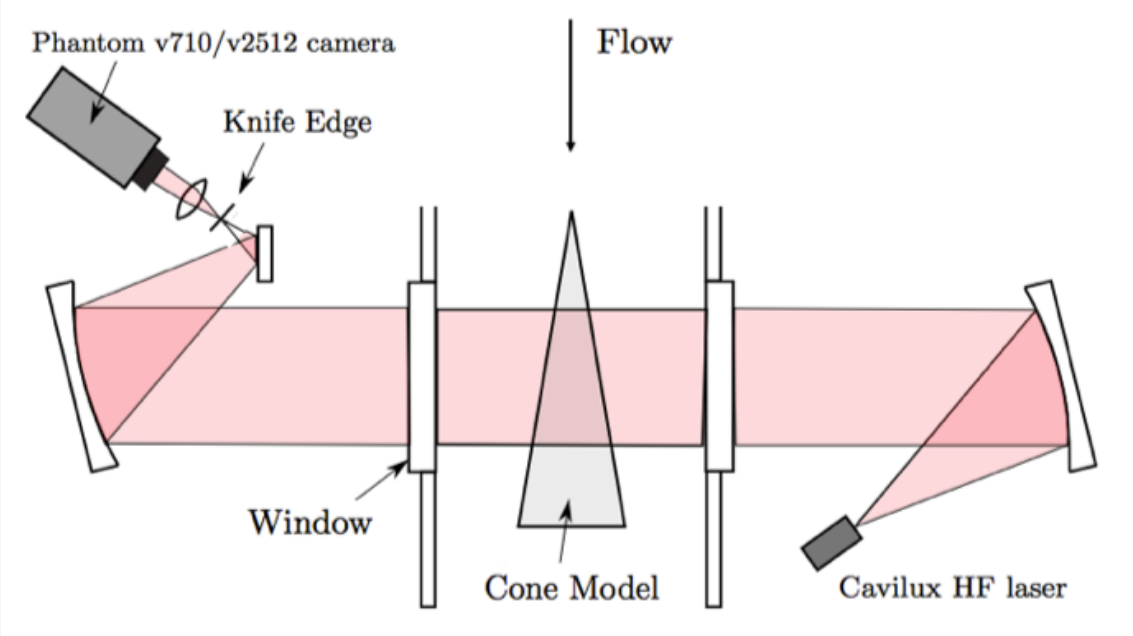

Figure 3.1: Schematic of schlieren setup installed in wind tunnel.

source. A number of studies including those of Elsinga et al. (2004) and Hargather and Settles (2012) have been dedicated to developing calibrated schlieren techniques, with the most promising techniques being rainbow schlieren, Schardin's calibrated schlieren technique using a weak lens, and background-oriented schlieren (BOS).

In the rainbow schlieren technique, quantification of light refraction is achieved through the use of a color cutoff filter in place of a knife edge. The color filter causes the light to take on the hue of the location on the filter it passes through, generating the mapping from color to light-ray refraction angle. A color camera is then used to capture the images. In the calibrated schlieren technique, a weak lens with a known density gradient is placed in the field of view of a standard schlieren setup to provide a calibration of light deflection angle to a grayscale pixel intensity. The technique can be used on any standard schlieren setup since it requires no modification of the

schlieren components. Background-oriented schlieren is distinct from the previous two techniques. A random dot background pattern is placed behind the test section; a camera is then focused onto the pattern and records a flow-off image. Once flow begins and density disturbances appear, the pattern displacement due to the refractive-index spatial distribution in the flow is computed using a cross-correlation and used to derive the location and magnitude of the disturbances.

While reasonably good results have been achieved in the literature using each method in a bench-top setting, it is important to consider the limitations of each technique in a hypersonic wind tunnel. First, the high-speed Phantom camera available for each experimental campaign is monochromatic, eliminating the possibility of using rainbow schlieren. We also consider the need for flexible and fast installation in multiple facilities. The BOS system requires correctly sized pattern dots in order to avoid spatially filtering features; too small and the dots will not move a full pixel between frames; too large and the dots will compress but not translate. This would require multiple grids per experimental campaign as the length scale of features in the boundary layer are a strong function of the freestream conditions. Additionally, Elsinga et al. (2004) encountered post-processing difficulty when using BOS in a wind tunnel as the background pattern, mounted to the far window, experienced movement due to tunnel vibration, which increased the signal noise. Given these constraints, along with the ease and speed of implementation of the lens calibration technique, the latter was chosen for the current studies. Finally, we note that if the light is emitted from a rectangular source, such as the LED used by Laurence et al. (2014), calibration is not required as the schlieren response should be linear. Use of

an LED in the current system, however, is impractical due to limitations on pulse frequency and duty cycle.

3.2.2 Calibration Process

Following the calibration method of Hargather and Settles (2012), a weak lens was placed within the schlieren field of view prior to each experiment and used as the calibration object. The lens is plano-convex with a focal length of either 5 m or 10 m and a diameter of 25.4 mm. The calibration process works as follows. First, the calibration lens is placed within the schlieren system field of view. Depending on the radial location where the parallel light rays pass through the lens, they will be refracted by an angle ranging from zero at the center of the lens to a maximum ε_R at the lens radius. For a weak lens, i.e. $r \ll f$, the relationship between r and ε is defined as

$$\frac{r}{f} = \tan\varepsilon \approx \varepsilon. \tag{3.1}$$

For a two-dimensional field (as provided by the non-focused schlieren system), the deflection angle ε can then be related to the density gradient as

$$\varepsilon_y = \frac{1}{n}\int \frac{\partial n}{\partial y} dl = \frac{L}{n_\infty}\frac{\partial n}{\partial y} = \frac{\kappa L}{n_\infty}\frac{\partial \rho}{\partial y}, \tag{3.2}$$

where L is the integrated light-path length,

$$n = \kappa\rho + 1, \tag{3.3}$$

ρ is the density of the test gas, and κ is the Gladstone-Dale constant. The light ray deflection angle, ε_y can be related to f and r as

$$\varepsilon_y = \varepsilon - \varepsilon_0 = \frac{1}{f}(r - r_0). \tag{3.4}$$

Next, the schlieren image of the lens is used to generate a unique mapping of grayscale values to the r coordinate. Figure 3.2 shows a schlieren visualization with the weak lens in the field of view. A pixel-intensity gradient is present across the lens face due to the known lens density-gradient profile. Pixel intensities are extracted for each row across the lens face and the results from several pixel columns are averaged together to smooth any imperfections present in the optics. This process is repeated with the lens in several different locations within the field of view to account for any non-uniformity in the flow-off schlieren background intensity. The optical center of the lens is defined based on the mean schlieren background intensity, and the vertical coordinate of the center of the lens is set to r_0 (see §3.2.3 for more details regarding the definition of the lens center). Finally, a fourth-order polynomial is fit to the pixel intensity versus vertical location data points to generate the mapping function. The right plot in figure 3.2 shows the pixel intensities and polynomial fit.

3.2.3 Sensitivity Analysis

Experiments were performed to characterize the weak calibration lens and quantify the effect of alignment of the lens within the schlieren system on the resulting calibration. Limited setup time and space within hypersonic wind tunnels often leads to sub-optimal data-acquisition conditions and motivates the importance

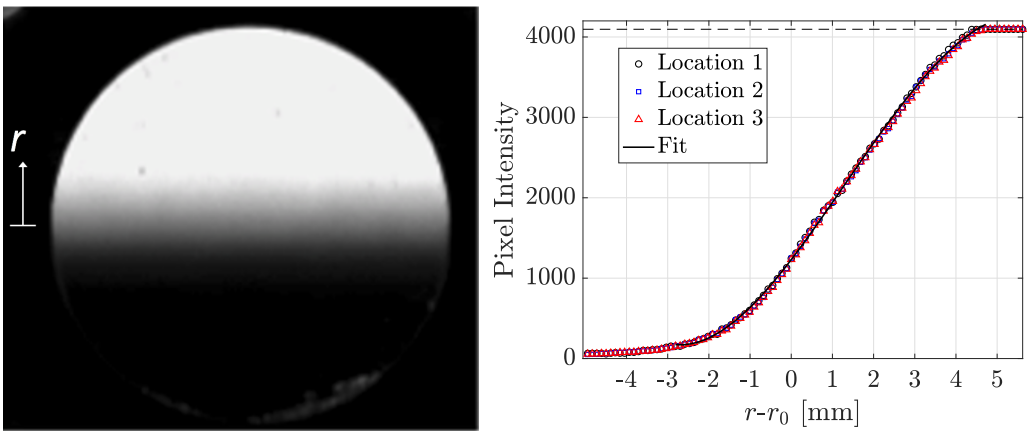

Figure 3.2: Schlieren image of calibration lens (left). Example calibration curve generated from the lens at 3 different locations in the schlieren field of view (right). The dashed line indicates the maximum pixel intensity of the 12-bit image.

of understanding the limitations of the lens calibration method. We begin by considering the subtle but important definition of the center of the calibration lens. Two definitions exist: the geometric center and the optical center. The geometric center of the lens is defined as the point equidistant from every point on the lens edge, whereas the optical center is defined as the location on the lens face where the pixel intensity is equal to the schlieren background intensity (here, 92% of the background intensity is used due to the absorption of the NBK-7 lens for 810 nm light). In theory, the geometric center of the lens and optical center of the lens should align. However, due to manufacturing tolerances for lenses with extremely large focal length to diameter ratios, the optical center is typically offset from the geometric center by approximately 0.1% of f, which for the 10 m-lens case corresponds to a distance of 10 mm, or slightly less than half the diameter of the lens. Figure 3.3 illustrates the effect of rotating the lens about the axis parallel to the schlieren system. The optical center and pixel-intensity gradient region shifts vertically depending on the

rotation angle, indicating that the optical center is offset from the geometric center. In figure 3.3, we observe the curve fit generated from the upper left and lower left images of the lens. Although the optical center is shown to shift vertically between these two orientations, when r_0 is set to the background image intensity, the curves align to within the experimental measurement error. From this observation it is concluded that the misalignment does not significantly impact the calibration curve and the calibration technique is minimally affected so long as the calibration image is captured with the lens oriented to have close agreement between the geometric and optical centers. Experiments using a 5-m focal length, 25.4 mm-diameter lens yielded similar behavior; however, a smaller movement of the optical center with respect to the geometric center was observed as a result of the manufacturing error being a percentage of the focal length. The offset between the geometric and optical center was also confirmed for both lenses using laser differential interferometer measurements.

Variations in the sensitivity of the schlieren system are most easily observed using the calibration lens by increasing the laser light source pulse width while maintaining a constant schlieren background intensity by increased knife-edge cutoff. Since the sensitivity of the schlieren system is proportional to the amount of light cut off by the knife edge (i.e. $s{=}f/A$ where f is the mirror focal length and A is the area of the light not cut off), the system with the longest pulse width at a constant background should be the most sensitive. The increased sensitivity causes the pixel gradient to occur over a smaller vertical region anchored around the optical center of the lens, as the same density gradient will cause a larger change in pixel intensity.

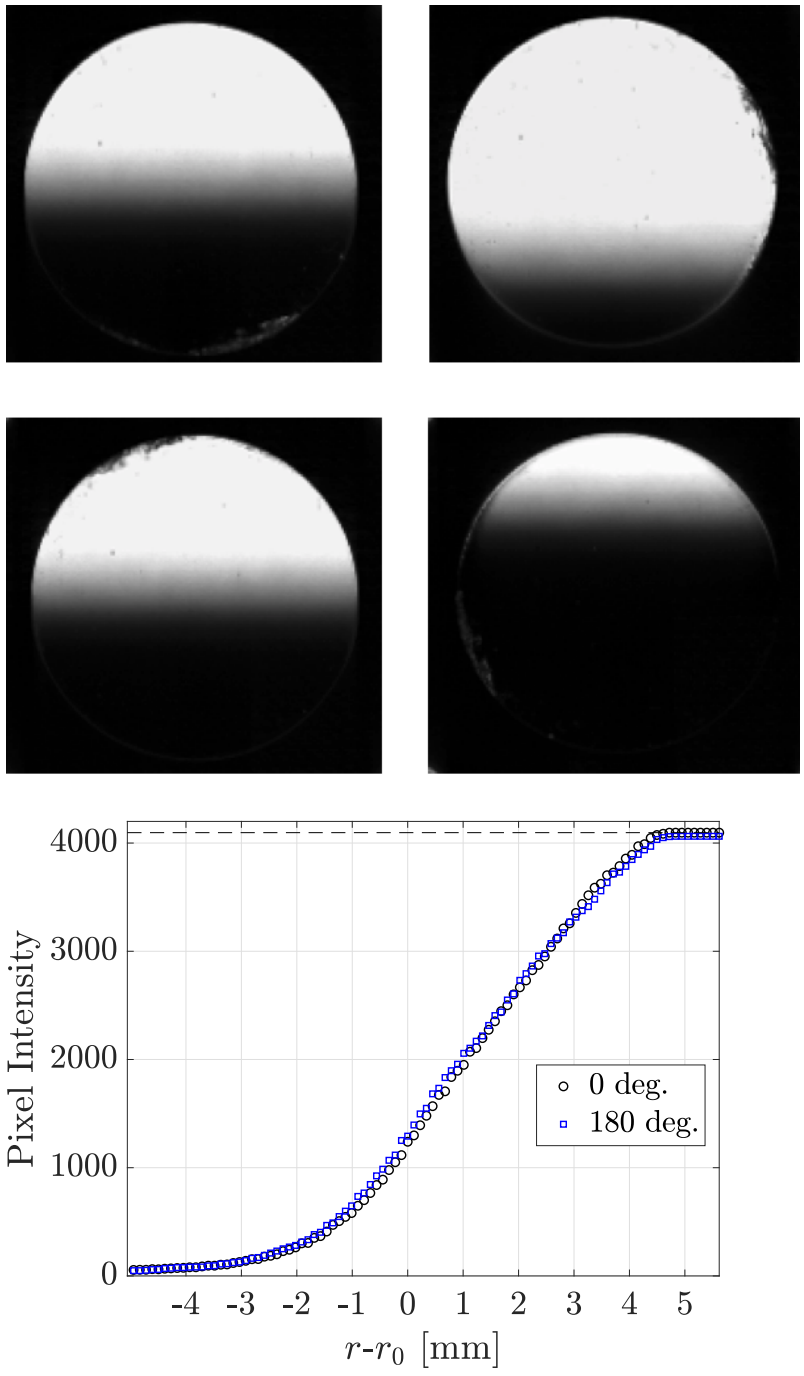

Figure 3.3: Schlieren images of the calibration lens at a rotation angle of 0°, 90°, 180°, and 270° (top: top left, top right, bottom left, bottom right). Calibration curves generated from the 0° and 180° images (bottom). The dashed line indicates the maximum pixel intensity of the 12-bit image.

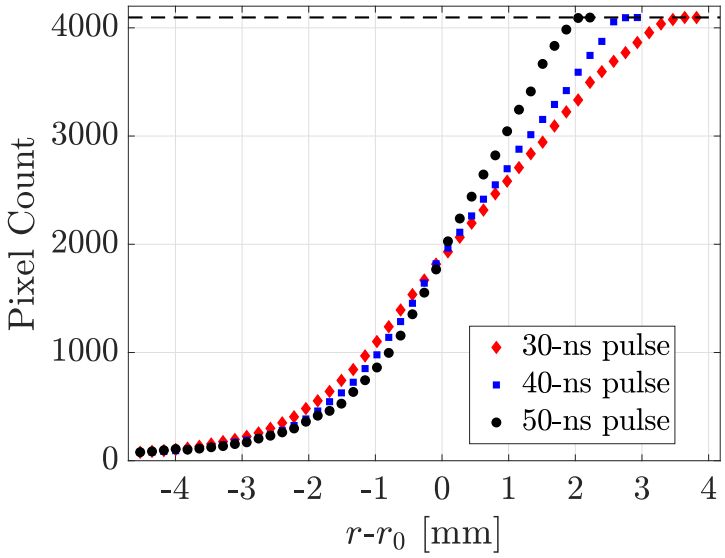

Figure 3.4: Calibration curves for different sensitivity schlieren setups. The dashed line indicates the maximum intensity of the 12-bit image.

Figure 3.4 shows calibration curves generated for three different sensitivity schlieren configurations. Steeper calibration curve slopes indicate a more sensitive schlieren setup.

In addition to characterizing the lens, experiments were conducted to quantify the effect of misalignment of the lens within the schlieren system. The first series of experiments examined misalignment along the schlieren optical axis. The calibration lens was placed in the 0° orientation shown in the top left of figure 3.3 and rotated in 5 degree increments to a maximum 10° misalignment between the lens and schlieren optical axis. The calibration curves generated for each configuration are shown in the top plot of figure 3.5 and very little difference is observed between the calibration curves for each configuration. Given the consistency in the curves, a slight offset in the relative tilt angle of the lens that may be expected due to human error is concluded to have minimal impact on the calibration.

We now consider the translation of the lens along the schlieren optical axis. During the calibration procedure, it is preferred to place the lens in the center of the test section in sharp focus, yet often this proves challenging given the combination of limited test section access and strict run procedures. To explore the implications of the lens being slightly out of focus, calibration curves are generated from images of the lens placed at the sharp focus and located at 0.3048 m and 0.6096 m towards the camera. The curves are presented in the lower plot of figure 3.5. Excellent agreement is observed between the curves below a pixel count of 3000, while a difference of approximately 10% is observed for the highest intensities. Therefore, slight error may be present in calibrating the brightest features, but in general the schlieren sensitivity is set such that the dynamic range does not exceed $80-90\%$ of the entire measurement range. We therefore conclude that the effect of the lens being slightly out of focus is minimal.

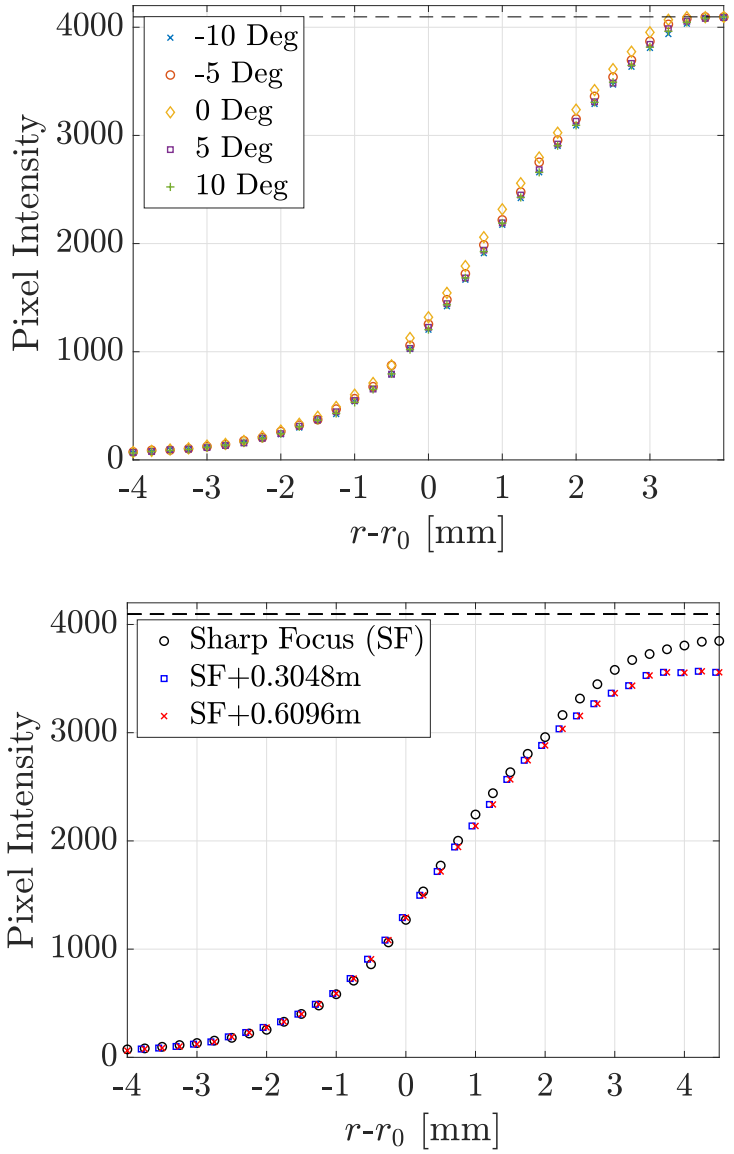

Figure 3.5: Calibration curves generated from images with the lens oriented at angles offset from the schlieren optical axis (top). Calibration curves generated with the lens translated along the schlieren optical axis (bottom). Positive distance is towards the camera side of the schlieren setup. The dashed line indicates the maximum intensity of the 12-bit image.

Chapter 4: Analysis

In this chapter, the pixel-intensity time-reconstruction technique is described, and the post-processing routines applied to the experimental data collected for each campaign are outlined. Definitions of the most important second-mode measurements are provided in the context of the unique high-speed schlieren data.

4.1 Pixel Intensity Time Reconstruction

The calibrated schlieren technique that was employed throughout this work measures disturbance intensity over a finite spatial interval at a specified instant in time, rather than a time series at a specific location. In order to facilitate a time-averaged analysis, time-resolved pixel-intensity signals at specific locations are reconstructed using the spatial data available in the schlieren images. The reconstruction technique relies on the periodicity of the second-mode disturbances, a constant wavepacket propagation speed, and a camera frame rate equal to roughly one-half of the fundamental second-mode frequency or greater. The high camera frame rates relative to the fundamental second-mode frequencies ensures that individual disturbance features are captured in multiple frames and do not evolve significantly between sequential visualizations. The reconstruction procedure is summarized in

figure 4.1. Consider the pixel intensity at a specific location (x_0, y_0) in two consecutive images, at times t_1 and $t_2 = t_1 + \delta t$. The intensity values are known exactly at times t_1 and t_2, but it is desired to reconstruct the intermediate values. If we assume the flow structures to be frozen and propagating horizontally at a speed U_{prop} (for which we will use the average wavepacket propagation speed - see §5), then we have two possibilities available for these intermediate values: the pixel intensities between $x_0 - U_{prop}\delta t$ and x_0 in the first image, and those between x_0 and $x_0 + U_{prop}\delta t$ in the second (figure 4.1, middle plot). Since the first interval will be more appropriate for times close to t_1 and the second for times close to t_2, we take a linearly weighted average of the two, with the resulting composite signal matching exactly the known points at t_1 and t_2 (figure 4.1, bottom plot). In general, $U_{prop}\delta t$ will not correspond to an integer number of pixels, and thus interpolation will be required in generating this composite signal. By repeating for all image pairs of interest, a reconstructed temporal signal is obtained with an effective sampling frequency of $f_{eff} = U_{prop}/\delta x$, where δx is the visualized distance between neighboring pixels. In the experimental results of the present study, f_{eff} ranges from 3 –10 MHz.

The reconstruction is applied to produce time-resolved pixel-intensity signals at 60 – 100 evenly spaced streamwise locations in the field of view. The streamwise density of reconstruction locations is chosen as a tradeoff between computational time and information addition; while signals can be reconstructed at every streamwise pixel, in practice the inter-pixel distance is not large enough to observe a significant change in wave frequency or amplitude. In the wall-normal direction, the signals are reconstructed at the location corresponding to the largest disturbance

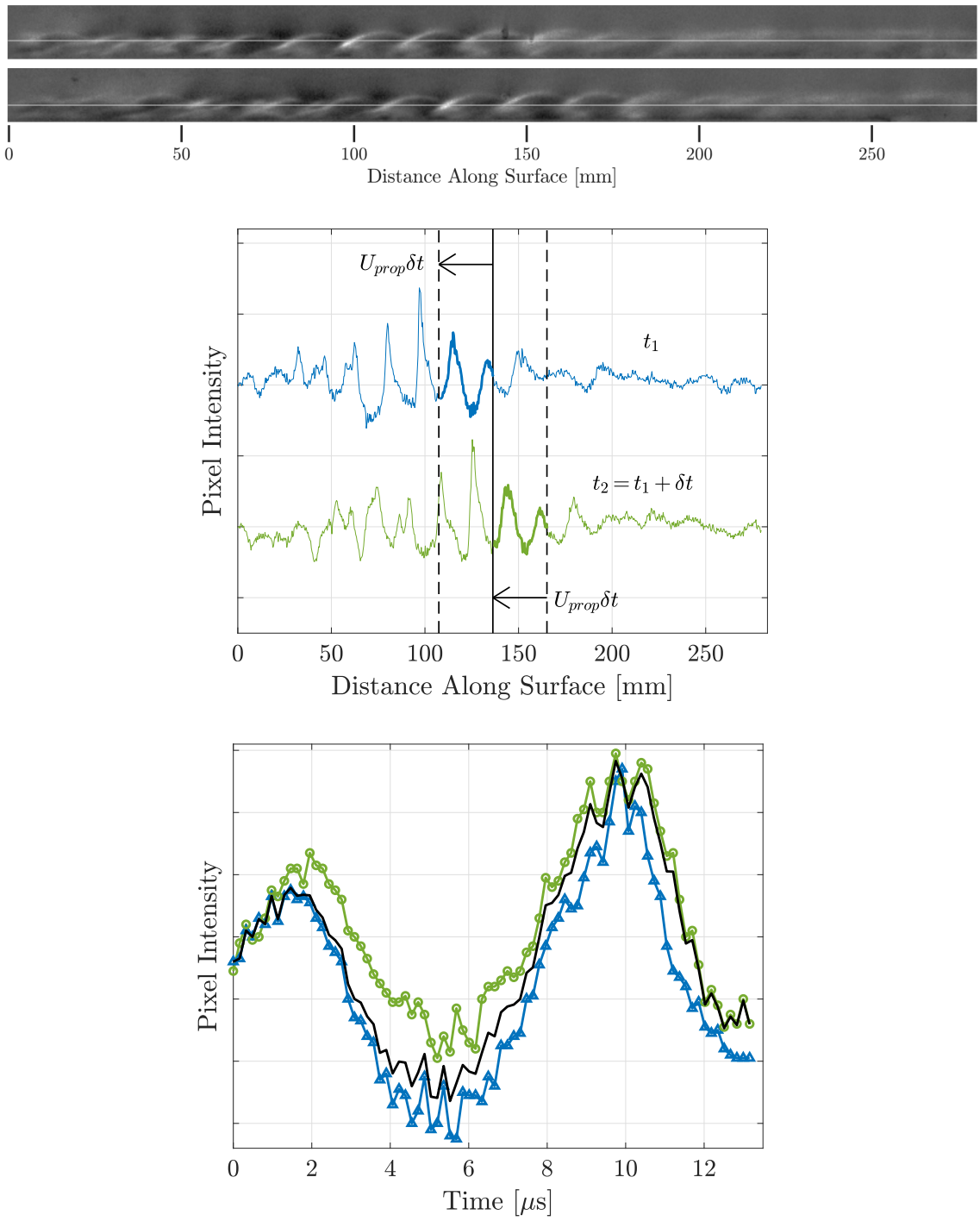

Figure 4.1: Enhanced schlieren images at times t_1 and t_2 (top); the white lines indicate the row of pixel intensities plotted in the middle plot. Schematic showing pixel intensities corresponding to the same segment of a wavepacket at times t_1 and $t_2 = t_1 + \delta t$ (middle); direction of arrow indicates increasing time t. Linear weighting of signals (-△-, t_1 signal; -◯-, t_2 signal; —, weighted signal) to generate reconstructed signal (bottom).

amplitude. In general, this location does not lie directly in the center of a pixel, and thus interpolation is used to generate the signal at the fixed y/δ location, taking into account the boundary-layer height downstream. Typically, 3000 – 8000 schlieren visualizations are used to generate the time-reconstructed signals, as this provides an adequate signal record length for computing frequency spectra.

4.2 Experimental Data Processing

Processing the schlieren visualization data begins with applying the techniques outlined in §4.1. In order to facilitate the pixel-intensity time reconstruction, it is necessary to first calculate the wavepacket propagation speeds for each individual experimental condition. Wavepacket propagation speeds are calculated using the correlation techniques described in Laurence et al. (2016). Because of the enormous number of images gathered per data set, the images are first processed by a feature-detection algorithm that identifies the presence and, if applicable, location of a wavepacket (Shumway and Laurence, 2015). The images are then bandpass filtered around the second-mode fundamental wavelength, and a cross-correlation is applied to image pairs throughout the sequence. Propagation speeds are computed from 7000 – 10,000 wavepackets and the error is typically 3 – 5% of u_p based on the 95% confidence interval. Computing propagation speeds of harmonic content yields similar results. Figure 4.2 shows a histogram of computed wavepacket propagation speeds from the AFRL LT run 30. Results for individual experiments are presented in their respective section of §5.

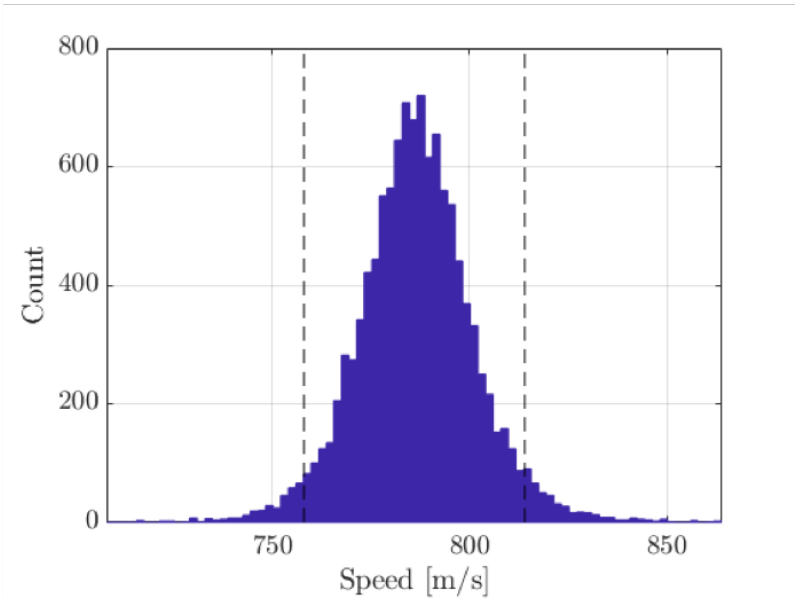

Figure 4.2: Histogram of computed wavepacket propagation speeds. The dashed lines indicate 2σ.

Once the propagation speeds are computed, the calibration and time reconstruction techniques can be applied. As described in §4.1, the signals are reconstructed at the wall-normal location of maximum disturbance intensity at 60–100 locations in the streamwise direction, where the number of streamwise locations is dictated by the image size. Spectra are computed from the time signals using Welch's method with 50% overlapping Hann or Blackman windows; the window size in each case is dictated by the length of the individual signal. The PCB sensor signals are processed in a similar fashion. Figure 4.3 shows a comparison of the power spectral density computed from the PCB and reconstructed schlieren signals at the same streamwise location collected from the Tunnel 9 Mach-14 run 4119. Good agreement is observed in the location and width of the fundamental and harmonic peaks at approximately 120 and 240 kHz. The power associated with the reconstructed signal at the lower end of the frequency spectrum is significantly

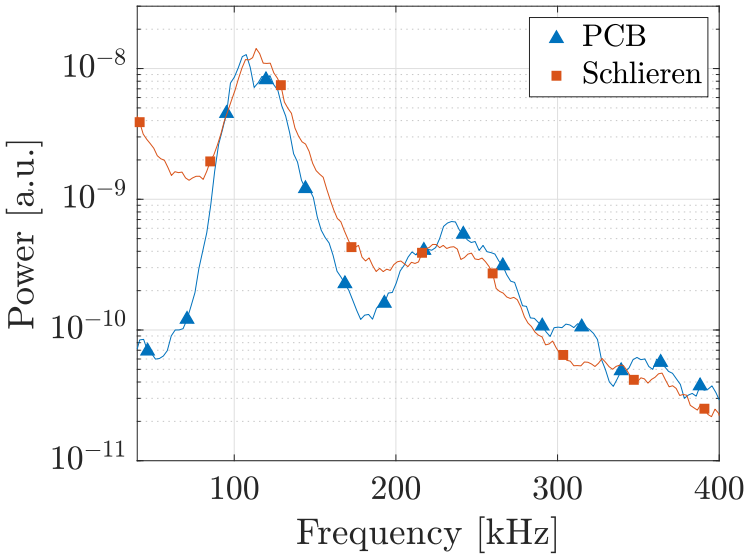

Figure 4.3: Power spectrum computed from PCB and schlieren signal at the same downstream location for Tunnel 9 Run 4119.

larger in the schlieren PSD, likely due to large wavelength structures from the nozzle wall in the visualization path. This increased power at frequencies less than 50 kHz is observed in all the schlieren spectra.

We note that, as described in §4.1, the reconstructed composite signal is generated by linearly interpolating between the signals of two images. This interpolation process alters the frequency-domain signature of the signal, specifically introducing narrow-band high-power regions that are clearly visible at frequencies of integer multiples of approximately the camera acquisition rate. In figure 4.4, we show the power spectra computed from a reconstructed signal. In general, their narrow bandwidth keeps the spikes from influencing any information extracted from the signal power spectra. However, in order to eliminate any influence of these artifacts, a band-stop filter is applied to the reconstructed signals in post-processing to remove the spikes.

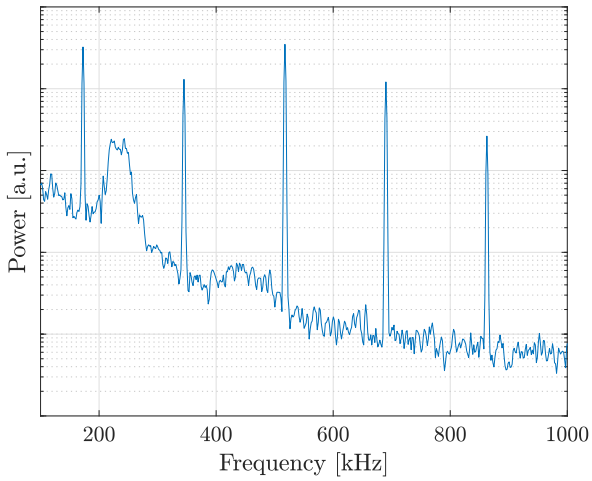

Figure 4.4: PSD computed from reconstructed signal with no band-stop filter applied.

4.2.1 Second-Mode Frequencies and N Factors Definition

Using the computed spectra, a quadratic function is fitted to the second-mode most-amplified frequency peak and used to identify the most-amplified second-mode fundamental frequency, f_0, and its amplitude. Following Stetson et al. (1983), the dimensionless frequency is defined as

$$F = \frac{2\pi f}{u_\infty Re/m}, \tag{4.1}$$

and the stability Reynolds number is defined as

$$R = \sqrt{Re_s}, \tag{4.2}$$

where Re is the Reynolds number based on the freestream conditions, and s is the cone surface coordinate. Maximum second-mode N factors are computed as

$$N(f, s_i) = \frac{1}{2}\ln(\mathrm{PSD}(f, s_i)) + c, \tag{4.3}$$

where $\mathrm{PSD}(f, s_i)$ is defined as the peak power of the most-amplified second-mode frequency at streamwise location s_i, and c is the intercept identified by vertically shifting the schlieren measurements to match the PSE results. Vertically shifting the schlieren N factors by a value c is required as the most upstream measurement location of the schlieren visualizations is downstream of the second-mode neutral point. Although the schlieren data successfully measure the relative growth of the wave amplitudes, without anchoring to the PSE results, the absolute value of the N factors is meaningless. Comparison of growth rates between two downstream locations is made possible by assuming the change in boundary-layer height is negligible between the measurement locations. As mentioned in §1.2, growing boundary layers are not strictly parallel, but the assumption is valid to leading asymptotic approximation and is thus commonly employed. Applying this assumption, the ratios of the density and density gradient disturbance amplitudes are equal, i.e., $\rho^{'}(s_2)/\rho^{'}(s_1) = \rho^{'}_{y}(s_2)/\rho^{'}_{y}(s_1)$, where prime denotes disturbance and subscript y denotes the derivative with respect to y. In the linear-growth regime, pressure and density are expected to scale proportionally; this relationship was demonstrated by Chang et al. (1997) who, using PSE-Chem, showed the disturbance growth rate calculated from the total kinetic energy of the disturbance to be equal to the growth rate calculated from other flow variables. Computing the slope of the linear portion of the schlieren N-factor curve is performed using a weighted least-squares method,

weighing the data points proportionally to the wave amplitudes.

As the second-mode most-amplified frequencies have been shown to scale with $1/\delta$, f_0 decreases with increasing streamwise location. The definition of N factor presented in equation 4.3 implicitly assumes (incorrectly) that the disturbance initial amplitudes, A_0, are constant across the range of second-mode frequencies. Figure 4.5 from Duan et al. (2019) shows freestream pitot-pressure fluctuations acquired in multiple facilities. The data suggest that the freestream disturbance spectrum relevant to second-mode-dominated boundary-layer transition may be modeled with a constant-slope model of $\Phi \sim f^{-3.5}$. In the most-impacted measurements of the present work (i.e., conditions with the largest range of observed second-mode frequencies), this results in $\Delta N \approx 0.4$. While not negligible, this change in N factor falls within the range of the experimental error and no correction is made for the initial disturbance amplitudes over the fairly narrow range of f_0 for each experiment. Equation 4.3 can also be used to compute N factors as a function of both frequency and streamwise location, allowing the shift in frequency and growth of higher harmonics to be observed. Due to the difference in initial amplitudes discussed above, the absolute value of harmonic N factors should not be considered, but relative growth of the same frequency bands remains meaningful. Further quantification of the error present in the frequency and amplitude calculations is found in §5.4.

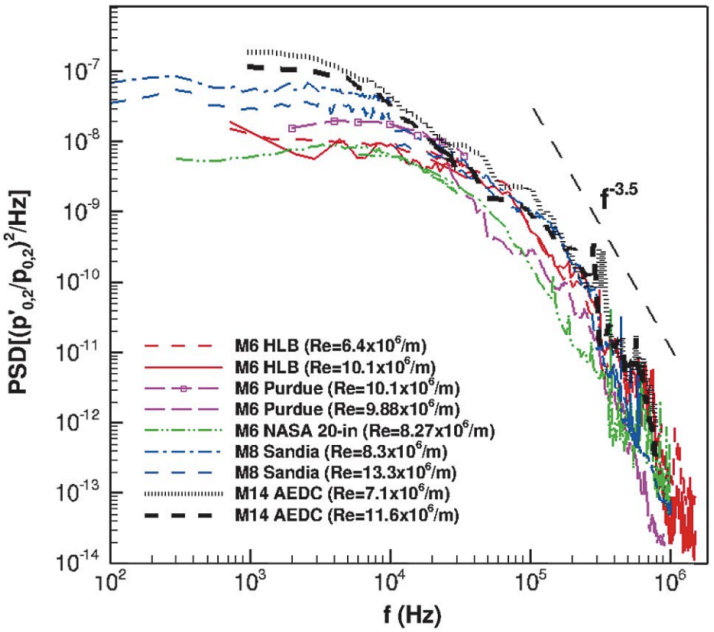

Figure 4.5: "Power spectral density of freestream pitot-pressure fluctuations measured in multiple high-speed facilities," (Duan et al., 2019).

4.2.2 Bispectral Analysis

The measurement resolution of the time-reconstructed schlieren signals, at roughly an order of magnitude greater than the second-mode most-amplified frequencies, reveals higher harmonics in the signals and allows for higher-order spectral techniques to be implemented in an effort to characterize their origins. The development of nonlinear interactions in second-mode waves has previously been investigated using a bispectral analysis. Using this method, Kimmel and Kendall (1991) identified nonlinear interactions responsible for the generation of a first harmonic at a frequency of approximately twice the second-mode fundamental [1]. Simi-

[1]The use of first harmonic to represent a frequency of $2f_0$, second harmonic for $3f_0$, and so on, is the commonly used nomenclature in the high-speed boundary-layer transition literature and will be used in the present work.

lar analyses by Chokani (2005) and Hofferth et al. (2013) revealed these interactions to be present in second-mode waves developing in a quiet-flow Mach-6 freestream as well. In addition to interactions leading to the first harmonic, Bountin et al. (2008) observed subharmonic resonance with detuning and potential interactions with disturbances in the first-mode frequency range.

The most commonly used technique to quantify these nonlinear interactions is to compute the signal bicoherence. The bicoherence, b^2, is defined as a normalized bispectrum. The bispectrum, a third-order cumulant spectrum, measures the extent of statistical dependencies of three spectral components by examining the phase coherence, if any, between them. Using the normalization formulated by Kim and Powers (1979), the b^2 value is bounded between 0 and 1, indicating no phase coupling and full phase coupling, respectively. In practice, noise inherent to the experimental measurements reduces the maximum b^2 values to less than 1. For a continuous signal, the bicoherence is defined as

$$b^2(f_1, f_2) = \frac{|E[X(f_1)X(f_2)X^*(f_1+f_2)]|^2}{E[|X(f_1)X(f_2)|^2]E[|X(f_1+f_2)|^2]}, \tag{4.4}$$

where E is the expectation operator, $X(f)$ is the Fourier transform of a segment of the time-series record, and * indicates the complex conjugate. The discrete bicoherence for M signals of length L, is computed using the discrete Fourier transform as

$$b^2(f_1, f_2) = \frac{|\frac{1}{M}\sum_{i=1}^{M} X(f_1)^{(i)}X(f_2)^{(i)}X^*(f_1+f_2)^{(i)}|^2}{\left[\frac{1}{M}\sum_{i=1}^{M}|X(f_1)^{(i)}X(f_2)^{(i)}|^2\right]\left[\frac{1}{M}\sum_{i=1}^{M}|X(f_1+f_2)^{(i)}|^2\right]}. \tag{4.5}$$

As described by Kimmel and Kendall (1991), the choice of record length, L, can

have a large effect on the measured b^2 values, as added noise can cause the relative phase of components to drift during long record lengths, artificially lowering the measured bicoherence. Choosing the record length becomes a tradeoff between frequency resolution and keeping the record length short enough to avoid the decoupling influence of the noise. Analysis performed on the current data showed changing record lengths up to a maximum of 256 points for the AEDC Tunnel 9 and AFRL LT data and 512 points for the AFRL HRN data to have no impact on the computed b^2 values. A record length of 256 and 512 points was thus used to compute the bicoherence for the Tunnel 9 and AFRL LT data and the AFRL HRN data, respectively.

Symmetries inherent to equation 4.5 result in all the unique interactions lying between two triangular regions. Interactions between $(0,0)$, $(f_N/2, f_N/2)$, and $(f_N, 0)$, where f_N is the Nyquist frequency, are sum interactions, and those between $(0,0)$, $(f_N, 0)$, and $(f_N, -f_N)$ are difference interactions. Figure 4.6 shows a sample bicoherence plot where phase locking of fundamental frequency content at f_0 leads to growth of a first harmonic at $2f_0$. Using the nomenclature of Chokani (2005), interactions are presented as $f_1 + f_2 \rightarrow (f_1 + f_2)$, where $\rightarrow$ denotes "generates by phase-locked interaction". A strong sum interaction observed at $f_0 + f_0 \rightarrow 2f_0$, for example, indicates a disturbance at f_0 reinforcing itself and transferring energy to the first harmonic at $2f_0$. The difference interaction $2f_0 - f_0 \rightarrow f_0$ shows energy exchange between content at the fundamental frequency and the first harmonic. In §5, the bicoherence is presented at specific experimental conditions where nonlinear wave growth is observed.

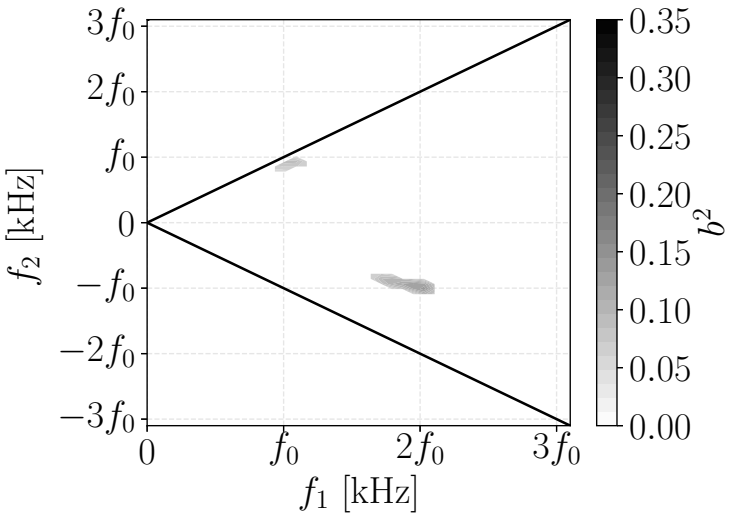

Figure 4.6: Sample bicoherence plot from AFRL LT Run 9. The solid lines indicate planes of symmetry.

4.3 PSE-Chem

Computational analysis is performed using the STABL software suite described by Johnson et al. (1998), Johnson (2000), Johnson and Candler (2005) and implemented in Jewell (2014) and Wagnild et al. (2010). First, the mean flow over the cone at zero incidence is computed by means of the reacting, axisymmetric Navier-Stokes equations with a structured grid, using a version of the NASA Data Parallel-Line Relaxation (DPLR) code (Wright et al., 1998). This flow solver employs a second-order-accurate finite-volume formulation. Although the computation includes chemistry, the impact of chemical reactions is negligible, as the local maximum temperature remains sufficiently low for all the experiments. Sutherland's law is used to calculate viscosity. Grids for each configuration were generated using STABL's built-in grid generator, and mean flow solutions were examined to ensure

that a sufficient number of points were placed in the boundary layer for each stagnation pressure. The wall-normal span of the grid increases down the length of the cone, allowing for the shock to be fully contained within the grid for all cases tested. The grid is clustered at the wall as well as at the nose in order to capture the gradients in these locations. The stability analyses for the zero-incidence cone are then performed using the PSE-Chem solver, which is also part of the STABL software suite. PSE-Chem solves the reacting, two-dimensional, axisymmetric, linear parabolized stability equations to predict the amplification of disturbances as they interact with the boundary layer. As the temperatures remain sufficiently low, chemistry and molecular vibration effects are omitted. The N factor is computed using the disturbance kinetic energy as

$$N = \int_{s_0}^{s} \sigma ds, \tag{4.6}$$

$$E = \int_{\Omega} \overline{\rho}\Big(|\hat{u}|^2 + |\hat{v}|^2 + |\hat{w}|^2\Big) dV, \tag{4.7}$$

$$\sigma = -Im(\alpha) + \frac{1}{2E}\frac{dE}{ds}, \tag{4.8}$$

where E is the disturbance kinetic energy, σ is the growth rate, and α is the streamwise wave number.

For the Tunnel 9 angle of attack data, the mean flow solutions are computed using US3D, an implicit unstructured finite-volume solver developed at the University of Minnesota. The stability analyses are conducted using the STABL-3D LST

code. The use of the LST code instead of the PSE-Chem results in slightly lower predicted growth rates due to the inability to account for the changing height of the boundary layer.

For all the computational results, following Marineau et al. (2017), a linear function is used to fit the maximum N factor versus stability Reynolds number results, and a function of the form $f = g/R^h$, where g and h are constants, is used to fit the most-amplified second-mode frequency versus stability Reynolds number results for comparison to the experimental measurements. Additionally, for the blunt-nose experiments performed in the AFRL LT, estimates of the entropy-layer swallowing length, X_{SW} defined by Rotta (1966), are computed using a procedure based on Stetson (1983) to provide an empirically-based estimate of the extent of the entropy-layer influence.

Chapter 5: Sharp-Nose Results

In this chapter, the experimental data collected with sharp-nose cones in each facility are explored. Results from each experimental campaign are presented and compared in an effort to quantify the effect of facility characteristics and freestream conditions on second-mode instability-wave development.

5.1 AEDC Tunnel 9 Experiments[1]

5.1.1 Test Conditions

Data are presented for six experiments performed in AEDC Tunnel 9. Five of the experiments were performed with the Mach-14 nozzle installed and one was performed at Mach 10. A description of the freestream and reservoir conditions is presented in table 5.1. During the steady test time of the tunnel, the model was either held at zero incidence or initially held at zero incidence for several hundred milliseconds and then pitched continuously up to 10°. In the cases where the cone pitched, the relevant test times are reduced to $0.15-0.3$ seconds at zero incidence, depending on the conditions (the shortest test time for the highest unit Reynolds number). The time period over which the model is considered to be at a specified

[1]This material is adapted from Kennedy et al. (2017, 2018a,b)

T9 Run #	M_∞	Re_∞/m [1/m$\times 10^6$]	p_0 [MPa]	h_0 [MJ/kg]	p_∞ [Pa]	ρ_∞ [g/m^3]	T_∞ [K]	u_∞ [m/s]	AoA [deg]
4123	13.35	1.74	14.2	1.74	40.9	3.02	45.7	1841	0
4120	13.49	2.57	20.7	1.76	59.0	4.39	45.3	1852	0–10
4119	13.69	3.62	30.2	1.79	82.0	6.14	45.3	1867	0–10
4118	14.00	7.19	72.7	1.80	174.1	12.3	47.8	1838	0–10
4117	14.40	12.10	124.6	2.00	263.1	19.4	45.7	1974	0–10
4017	9.44	1.96	72.7	1.80	174.1	12.3	47.8	1321	0

Table 5.1: Reservoir (subscript 0) and computed freestream (subscript ∞) conditions for the Tunnel 9 experiments. AoA refers to the model angle of attack.

T9 Run #	Resolution [pixels]	Frame Rate [f.p.s]	Scale [pixels/mm]	Location s [m]	Wave Behavior
4123	1152×176	121,739	3.11	0.73 – 1.04	Linear Growth
4120	1024×368	65,016	1.61	0.73 – 1.22	Linear to Nonlinear Growth
4119	1024×320	72,041	1.61	0.73 – 1.22	Linear Growth to Breakdown
4118	1024×288	42,000	1.61	0.73 – 1.22	Nonlinear Growth to Breakdown
4117	–	–	–	–	–
4017	1280×128	76,009	2.55	1.27 – 1.55	Linear Growth to Breakdown

Table 5.2: Camera parameters used for the different experimental conditions.

nonzero angle of attack is defined as the time when the model is within $\pm 0.1^\circ$ of the specified angle (i.e., 1° corresponds to the model at $0.9^\circ - 1.1^\circ$ angle of attack). Visualizations from the Mach-14 experiments were collected using the calibrated high-speed schlieren system, while the Mach-10 data were acquired during an earlier experimental campaign prior to the development of the current high-speed schlieren setup. No visualization data were recorded for run 4117 as the boundary layer was fully turbulent by the most upstream location of the test section windows, but PCB data upstream of the transition location were recorded. Table 5.2 provides information on the schlieren visualization setup, and sample schlieren visualizations are seen in figure 5.1.

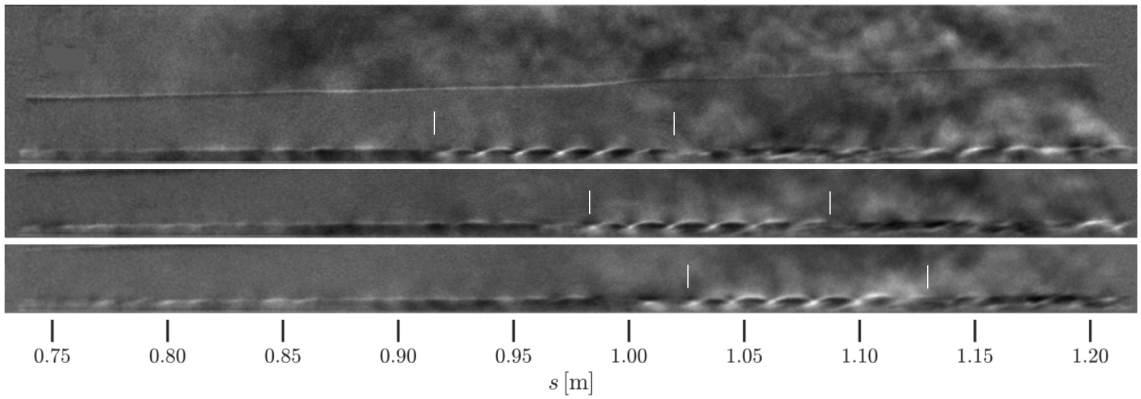

Figure 5.1: Enhanced image sequence showing the propagation and development of a second-mode wavepacket for run 4120. The white markers indicate the approximate extent of a wavepacket in the first image and have been translated downstream in subsequent images using the mean wavepacket propagation speed.

T9 Run #	u_p [m/s]	95% confidence [m/s]	u_p/u_e	Wavepackets Analyzed
4123	1637	85	0.90	7742
4120	1671	56	0.92	10000
4119	1706	60	0.93	8906
4017	1170	72	0.89	3265

Table 5.3: Wavepacket propagation speeds.

5.1.2 Time-Averaged Results

5.1.2.1 Zero Incidence

We begin by examining the mean wavepacket propagation speeds for each condition, computed using the techniques of §4.2. Table 5.3 shows the calculated speeds. The Taylor-Maccoll solution is used to compute the flow velocity at the cone surface and, assuming this surface velocity to correspond to the boundary-layer edge velocity u_e, $u_p/u_e = 0.89 - 0.93$ for these experiments. These values are slightly higher than those reported by Laurence et al. (2016), but lower than those reported in the hot-wire measurements of Stetson and Kimmel (1992).

The high-speed schlieren setup described in §3.1 was used to collect the data for the Mach-14 experiments. Time-averaged measurements are made using the time-signal reconstructed from $5000-8000$ images in the steady-flow period for runs 4123, 4120, and 4119. The temporal reconstruction is not applied to the run 4118 data as the waves are at a very late stage of development and beginning to breakdown to turbulence as they enter the field of view.

The maximum N factors calculated from the schlieren signals, PCB measurements, and PSE solutions are plotted versus stability Reynolds number in figure 5.2. The PCB measurements are plotted for each ray of sensors on the cone. In general, the slopes of the PSE, PCB, and schlieren curves agree well, with the slope of the schlieren measurements within 10% of the PSE results until saturation is reached. A significant amount of scatter is present in the PCB measurements, and we note that the schlieren measurements are approximately 20 times more spatially dense. As shown in the middle and bottom plots, N factors calculated from the schlieren signals saturate at larger R values than their PCB counterparts, resulting in greater transition N factors (good agreement is seen for the regions of linear growth at lower unit Reynolds numbers). Only the most downstream locations are included for run 4123 (top plot) as the upstream second-mode waves were too weak to provide an adequate signal.

Figure 5.3 shows the development of the second-mode disturbances as a function of frequency and streamwise location. The N factors generated from the PCB sensor data are calculated similarly with interpolation between the (rather sparse) sensor locations. For run 4120, the N factors calculated from the schlieren signals

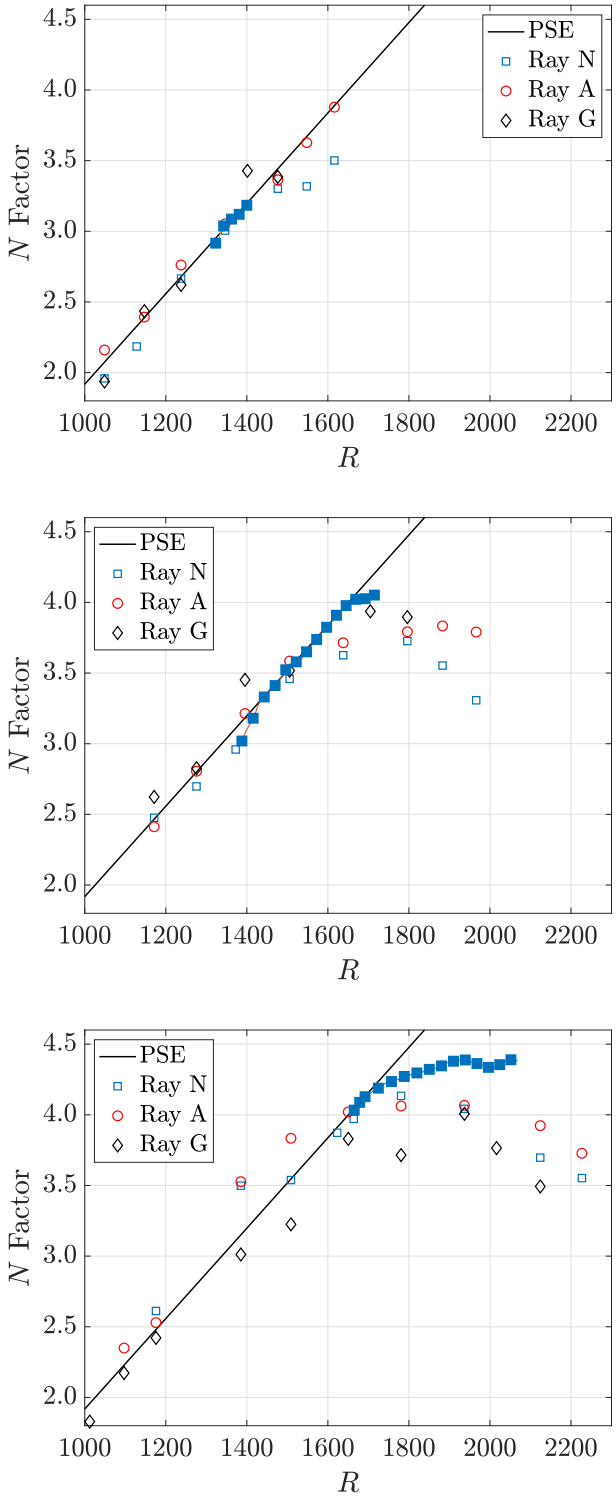

Figure 5.2: N factors calculated for the most-amplified second-mode frequencies for run 4123 (top), run 4120 (middle), and run 4119 (bottom). The filled symbols are schlieren measurements and the open symbols are PCB measurements. Markers are shown for every fifth schlieren data point.

match well with those calculated from the PCB signals in the linear-growth regime. As anticipated, the fundamental frequency band broadens for the schlieren N factors with increasing streamwise distance. Growth of a first harmonic occurs in the same frequency range in both the schlieren and PCB measurements. At any given streamwise location, the ratio between the N factors at f_0 and the first harmonic tends to be larger for the schlieren signal (i.e. the harmonic is relatively weaker).

In the lower part of figure 5.3 we show the streamwise development of the N factors at the higher unit-Reynolds-number run 4119. A clear discrepancy exists between the development of the schlieren and PCB N factors. The disturbance at f_0 saturates at approximately $s = 0.8\,\mathrm{m}$ in the PCB measurements, while saturation in the schlieren measurements occurs between $s = 1.1\,\mathrm{m}$ and $s = 1.2\,\mathrm{m}$ (also seen in figure 5.2). Similar behavior is seen for the first harmonic. However, the measured frequencies of both the fundamental disturbance and the first harmonic agree well between the two measurement techniques. The difference in N factor saturation location may be linked to several causes. First, nonlinear growth close to saturation may not be uniform across the boundary-layer thickness, causing the PCB measurements made at the surface of the cone to differ from the schlieren measurements made off the model's surface. The integration effect inherent to the schlieren system may also play a role; as the breakdown process begins and features become increasingly three-dimensional, the schlieren signal will become unable to resolve them accurately. The assumption of negligible change in boundary-layer height may begin to break down in this region as well. Finally, the PCB sensors record pressure fluctuations while the schlieren signals measure density gradients,

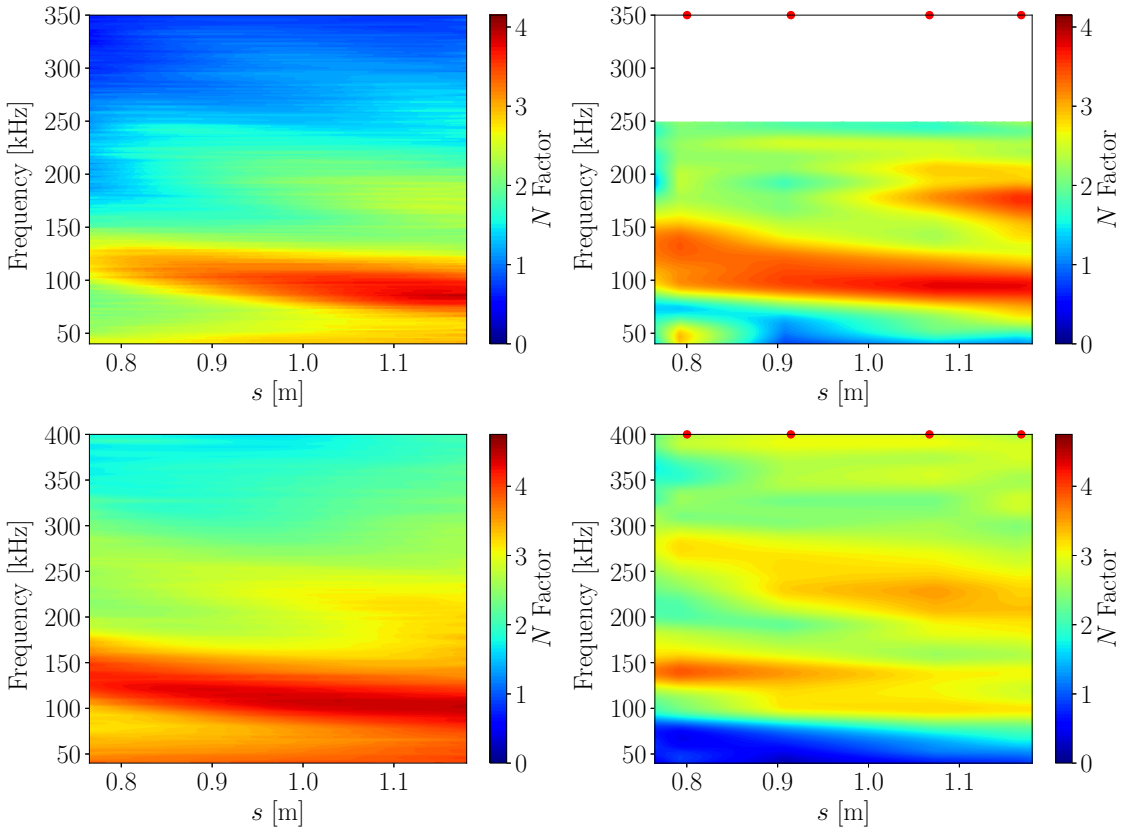

Figure 5.3: N factors as a function of frequency and streamwise location: run 4120 (top); run 4119 (bottom); calculated from schlieren visualizations (left); calculated from PCB measurements (right). Data above 250 kHz are omitted from the top-right plot due to noise in the PCB sensors. Red dots indicate streamwise locations of PCB sensors.

two measurements whose relationship is not clearly defined in the nonlinear-growth regime.

In figure 5.4 we show the bicoherence calculated from time-resolved density-gradient signals at two streamwise locations for runs 4120 and 4119 (no nonlinear interactions were present for run 4123). The bicoherence values were calculated using Hann windows of 256 points in length with 50% overlap. Focusing first on run 4120, at the upstream location ($s = 0.78$ m) strong sum and difference interactions are seen between higher harmonics up to $3f_0$. Additionally, interactions exist at

$f_0 + 0 \rightarrow f_0$ and $2f_0 + 0 \rightarrow 2f_0$ indicating that the power spectrum is being filled. The bicoherence reaches a peak value of $0.37 - 0.41$ in the $f_0 + f_0 \rightarrow 2f_0$ interaction and remains at this level until decreasing at approximately $s = 1.09\,\text{m}$. Further downstream, ($s = 1.14\,\text{m}$, top right) additional interactions are present, including sum and difference interactions between third and fourth harmonics ($4f_0$ and $5f_0$). The contours have also broadened in bifrequency space, indicating that the fundamental frequency disturbance and its harmonics are coupling with their sidebands.

We now turn our attention to run 4119 (lower plots, figure 5.4). At the upstream measurement location ($s = 0.81\,\text{m}$), a strong sum interaction exists at $f_0 + f_0 \rightarrow 2f_0$ and $2f_0 + f_0 \rightarrow 3f_0$, indicating disturbances at f_0 coupling to generate a harmonic at $2f_0$, and interaction of the harmonic content at $2f_0$ with disturbances at f_0 to generate a second harmonic at $3f_0$. A weak interaction also exists between $3f_0 + f_0 \rightarrow 4f_0$ and $2f_0 + 2f_0 \rightarrow 4f_0$ indicating slight amplification of a third harmonic. Difference interactions (lower-right quadrant) are also present between each of the higher harmonics. The interactions present at this upstream location are similar to those observed for the downstream measurement location of run 4120. In general, bicoherence is maximum at the most upstream measurement location for run 4119 with peak values of $0.25 - 0.3$ and decreases continuously downstream. For example, at $s = 0.88\,\text{m}$ (bottom right) bicoherence values for all interactions have decreased compared to $s = 0.81\,\text{m}$, and interactions involving a third harmonic have disappeared. No significant quadratic coupling is present by $s = 1.15\,\text{m}$ (not shown), where growth of the disturbances has saturated and the boundary layer is on the verge of breaking down; at this point the interactions are either no longer quadratic

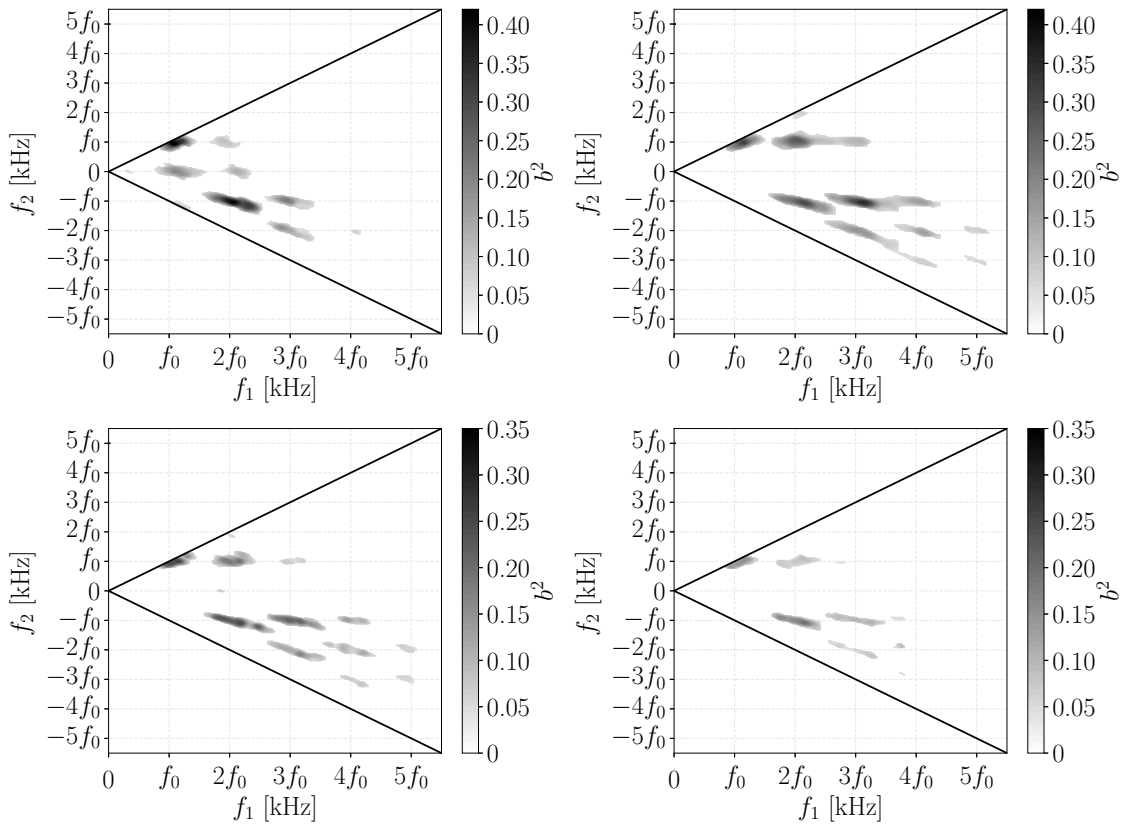

Figure 5.4: Bicoherence b^2 values calculated for run 4120 (top row) and run 4119 (bottom row) at locations: $s = 0.78$ m, $R = 1399$ (top left); $s = 1.14$ m, $R = 1692$ (top right); $s = 0.81$ m, $R = 1705$ (bottom left); $s = 0.88$ m, $R = 1782$ (bottom right). The black lines indicate planes of symmetry. The frequencies are represented by the fundamental disturbance frequency at the given streamwise location.

or the remaining fluctuations are random.

By examining the bicoherence plots shown in figure 5.4 in conjunction with the N factors shown in figures 5.2 and 5.3, we see that strong nonlinear interactions are present when the fundamental disturbance is still being amplified within the linear regime. The strongest nonlinear interaction generating the first harmonic appears to precede the highest values of N factor for the harmonic content, and the strength of the nonlinear interaction generating the first harmonic appears to be closely linked to the amplification rate (the slope of the N-factor curves) of the first harmonic. For

run 4120, the first harmonic is strongly amplified from the most upstream location until approximately $s = 1.05\,\mathrm{m}$, from which point the amplification rate decreases; this decrease in amplification rate coincides with a decrease in bicoherence values. Similarly, for run 4119, the N factor of the first harmonic increases over the entire measurement range, while both the amplification rate of the first harmonic and the bicoherence value describing that interaction are decreasing. Consistent with these observations, we also note that for run 4119, the first harmonic reaches a maximum N factor at a streamwise location where no significant nonlinear interactions are present. In addition, nonlinear interactions involving higher harmonics ($3f_0$, $4f_0$, $5f_0$) appear in the bicoherence plots while having little to no discernible power in the spectra.

5.1.2.2 Angle of Attack

The most comprehensive measurements of second-mode instability waves developing within the boundary layer of a sharp slender cone at angle of attack were performed by Stetson et al. (1985) and Marineau et al. (2014, 2017). Stetson et al. (1985) acquired hot-wire data at 2 and 4 degrees angle of attack in a Mach-8 freestream. Other than the anticipated shift in most-amplified frequencies due to the change in boundary-layer thickness and second-mode disturbance growth being delayed to higher local Reynolds numbers on the windward meridian, no significant changes in the stability characteristics of second-mode waves within the boundary layer, including the amplification rate, were observed. Marineau et al. (2014) used

PCB pressure sensors to acquire data in a Mach-10 freestream. They observed the same trend of backward movement of the transition front with increasing angle of attack on the windward meridian and attributed this behavior to the reduced initial amplitudes of the higher second-mode wave frequencies (from the freestream disturbance levels).

In the present study, the reconstruction was applied to produce time-resolved pixel-intensity signals with the model at 1, 2, and 3 degrees angle of attack for runs 4120 and 4119. All visualizations viewed the windward side of the cone (ray "N" in figure 2.5), and for the following analysis, angle of attack refers exclusively to the windward meridian. For the cone at angles of attack greater than 3 degrees, the boundary layer became too thin to extract reliable quantitative data from the schlieren measurements. Since the model pitched continuously, the definition for a specified angle of attack as $\pm 0.1^\circ$ results in $500-800$ images available for the reconstruction per angle of attack. The definition of angle was chosen as a tradeoff between error introduced from the cone continuously pitching and having a sufficiently long time series to compute frequency spectra. Computed wavepacket propagation speeds were found to lie in the same range observed for the zero-incidence waves. Sample visualizations are presented in figure 5.5.

The dimensionless most-amplified second-mode frequencies at 1, 2, and 3 degrees angle of attack are presented in figure 5.6. Good agreement is observed between the schlieren and PCB measurements and the LST results. A significant increase in frequency is observed with increasing angle of attack due to the decrease in boundary-layer thickness. Maximum N factors computed at 1 and 2 degrees angle

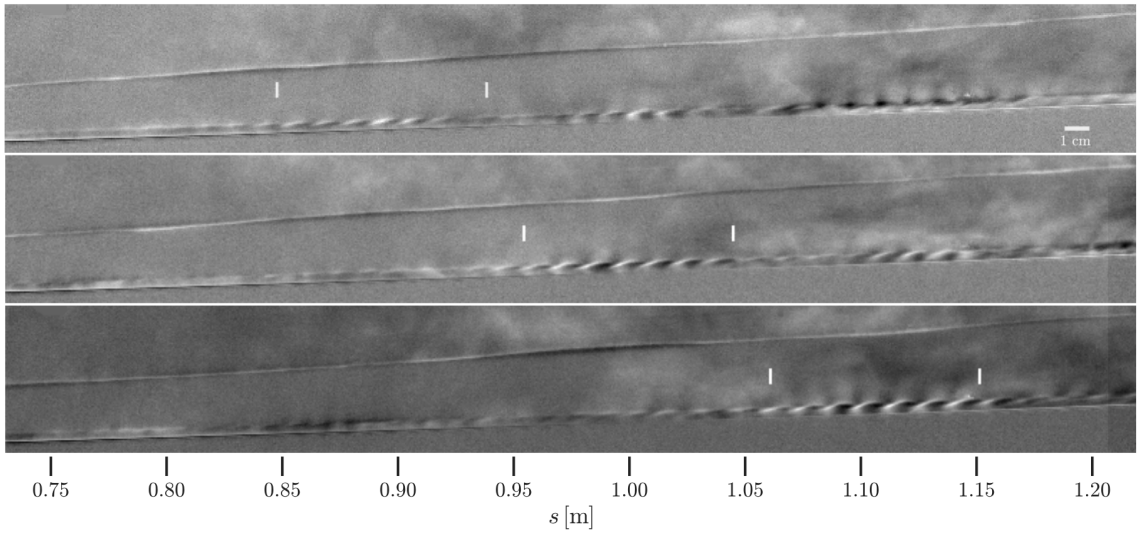

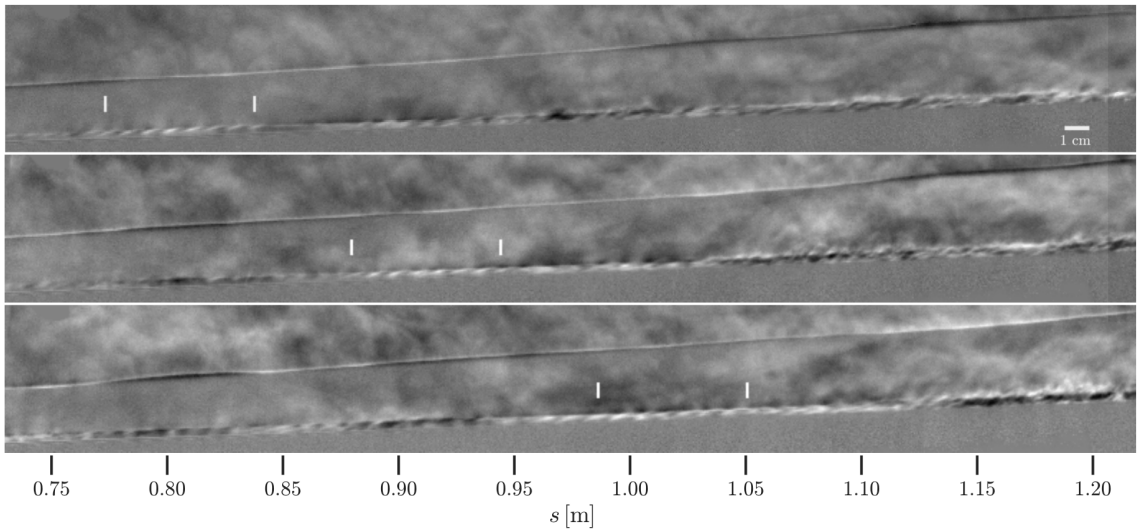

Figure 5.5: Enhanced image sequences showing the propagation and development of second-mode wavepackets on the windward side of the model at 2° angle of attack. Run 4120, every fifth image shown, $\Delta t = 76.9\,\mu s$ (top). Run 4119, every fourth image shown, $\Delta t = 55.5\,\mu s$ (bottom). In the upper part of each image, the shock from the cone nose tip is visible. The white markers indicate the approximate extent of a wavepacket in the first image and have been translated downstream in subsequent images using the mean wavepacket propagation speed.

of attack are presented in figure 5.7. No N factors are presented from the 3 degree angle of attack data as the boundary-layer is too thin (<6 pixels) to extract meaningful quantitative data. Several trends emerge from the data. First, similar to the zero incidence results, for a given angle of attack the transition N factor increases with increasing unit Reynolds number and, as mentioned in §4.2, this is believed to be a result of the freestream tunnel noise. Second, the LST-computed N-factor slope increases approximately 10% per degree increase in angle of attack, although this trend is not clearly confirmed by the experimental data. Table 5.4 provides a comparison between the schlieren-measured and LST-computed slopes at different angles of attack. In general, the schlieren slopes are within 10% of the LST, but no clear trend emerges with angle of attack. The previous hot-wire measurements at Mach 8 by Stetson et al. (1985) observed no major change of amplification rate with angle of attack, but their measurements again had high experimental scatter compared to the changes in amplification rates observed in the current LST results. Large scatter exists in the PCB measurements of the current dataset as well. While a slight increase in growth rate with angle of attack as indicated by LST results is possible, experimental noise eliminates the ability to confirm this trend in the experimentally obtained maximum N factors. Finally, we note that for a fixed unit Reynolds number, the transition N factor increases slightly with an increase in angle of attack.

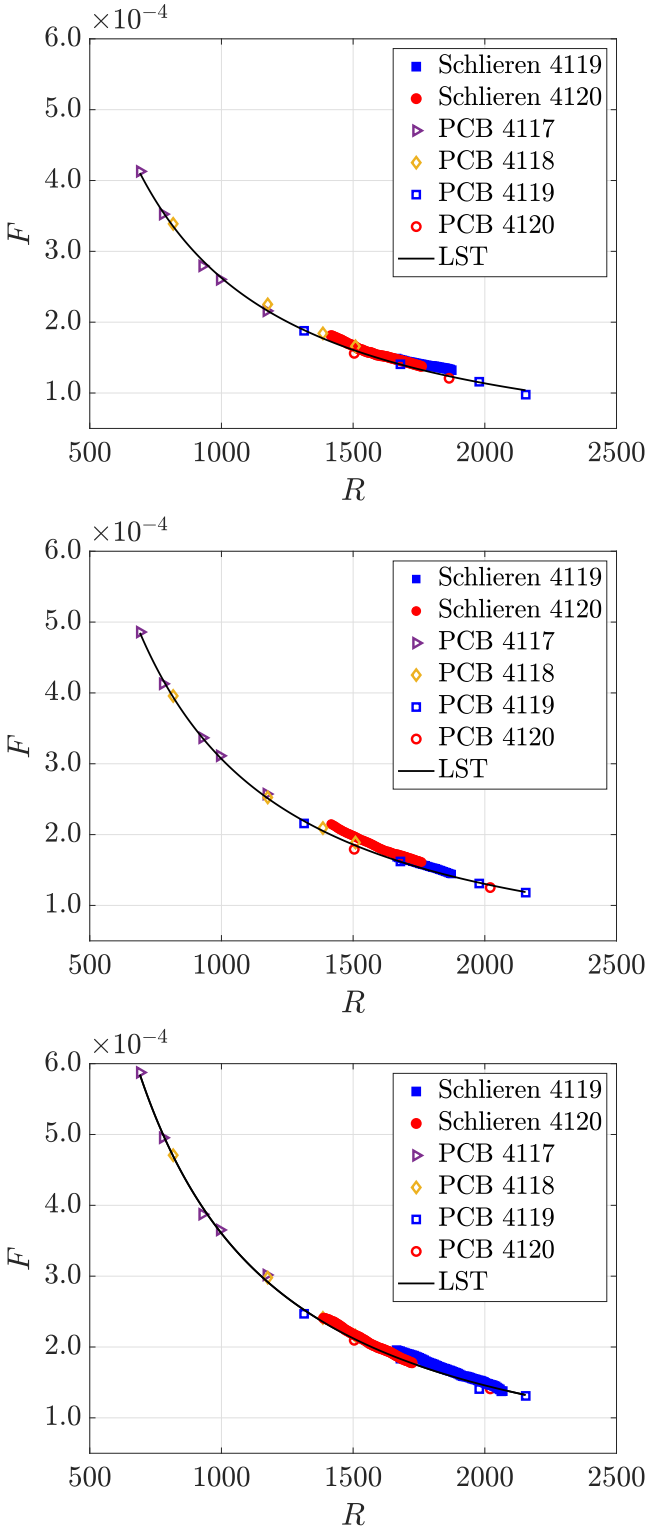

Figure 5.6: Dimensionless most-amplified second-mode frequencies at 1° AoA (top), 2° AoA (middle), and 3° AoA (bottom).

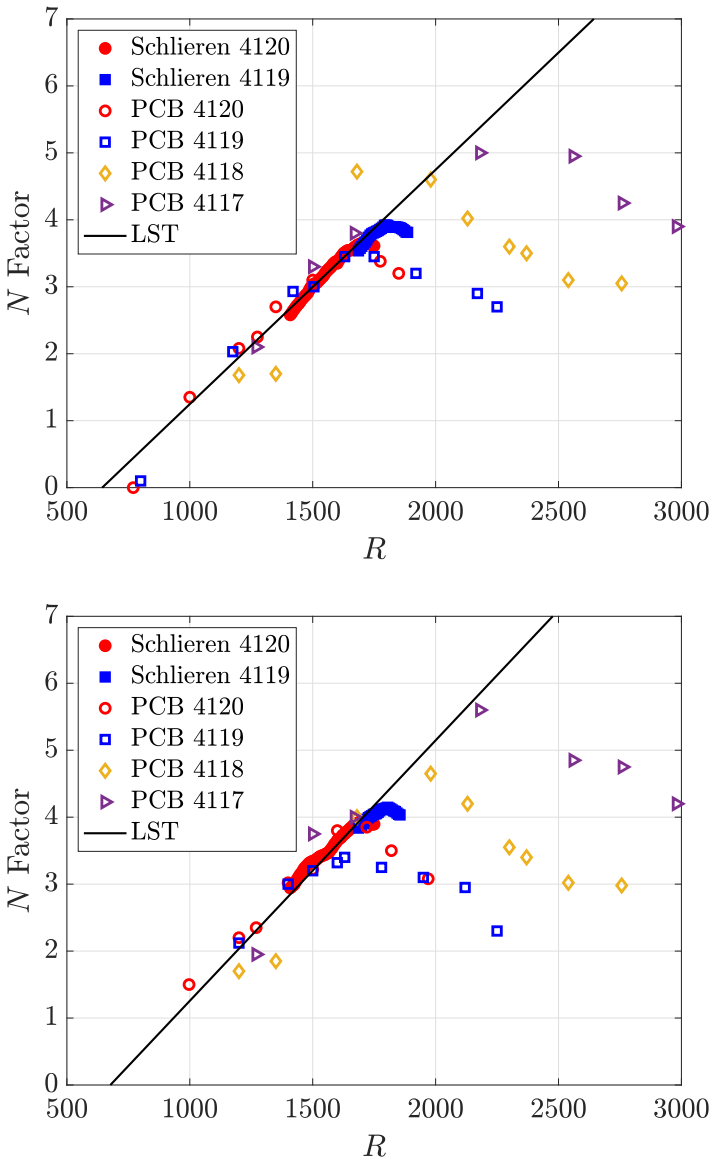

Figure 5.7: Maximum N factors at 1° AoA (top) and 2° AoA (bottom).

AoA [deg]	STABL	Schlieren	% Difference
0	3.1E-3	3.4E-3	+9.7
1	3.5E-3	4.0E-3	+11.4
2	3.9E-3	3.4E-3	−12.8
3	4.3E-3	NA	NA

Table 5.4: N-factor slopes ($\mathrm{d}N/\mathrm{d}R$) in the linear-growth regime at different angles of attack.

5.1.3 Individual Wavepacket Development

We now turn our attention to the development of individual second-mode wavepackets. The calibrated high-speed schlieren system used in the current study is particularly well suited to individual wavepacket analysis given the high temporal and spatial image resolution as well as even temporal spacing. Observations of the wall-normal development of individual wavepackets are made possible by the ability of the schlieren system to record data off the surface of the cone. The high frame rates allow $20-40$ sequential images to be captured for an individual wavepacket as it propagates across the field of view.

No single wavepacket is captured undergoing all stages of development within the visualization region at a single unit-Reynolds-number condition; however, general wavepacket development appears consistent across different conditions and angles of attack. Approximately 100 wavepackets per experimental condition with the cone at zero incidence were analyzed, and the wavepackets most representative of the mean behavior are presented. The following discussion focuses extensively on the visualizations recorded from runs 4120 and 4119 which, as demonstrated by the time-averaged results, contain waves from each stage of development.

In examining each case, the wall-normal coordinate is normalized by the local boundary-layer thickness computed using the schlieren visualizations. This is computed following the process outlined in Laurence et al. (2016). First, the post-shock surface conditions are computed using the inviscid Taylor-Maccoll solution and assumed to correspond to the edge conditions. These conditions are then used

to compute a similarity solution based on the Illingworth Transform and to identify the density-gradient profile at the downstream location of interest for a cone geometry. A numerical integration is performed across the line of sight to correct for the integration effect of the schlieren measurement system. The simulated profile is then compared to the experimentally measured intensity values from an average flow-on image and, if necessary, the theoretical value is stretched to match the experimental value. In most cases, the boundary-layer measured thickness matched the theoretical prediction within 10% resulting in a stretching factor of $1-1.10$.

5.1.3.1 Wavepacket Appearance

We begin by considering the wavepacket appearance. Figure 5.1 shows a wavepacket from run 4120 in its earliest stages of development. The waves initially take on a slanted appearance with a fairly constant inclination and are contained within the visual edge of the laminar boundary layer. In the linear-growth stage, the disturbance density gradients appear largest in the middle to upper portion of the waves, appearing similar to those seen in the low-enthalpy results reported by Laurence et al. (2016) and Casper et al. (2016) for a transitioning hypersonic boundary layer at lower freestream Mach numbers. As the waves propagate downstream they begin to take on a bent, curved-over shape. The peaks of the waves start to extend beyond the visual edge of the boundary layer and begin to fold over back towards the surface of the cone. Additionally, dark regions appear in the central portion of the wavepacket beneath the folded wave crests.

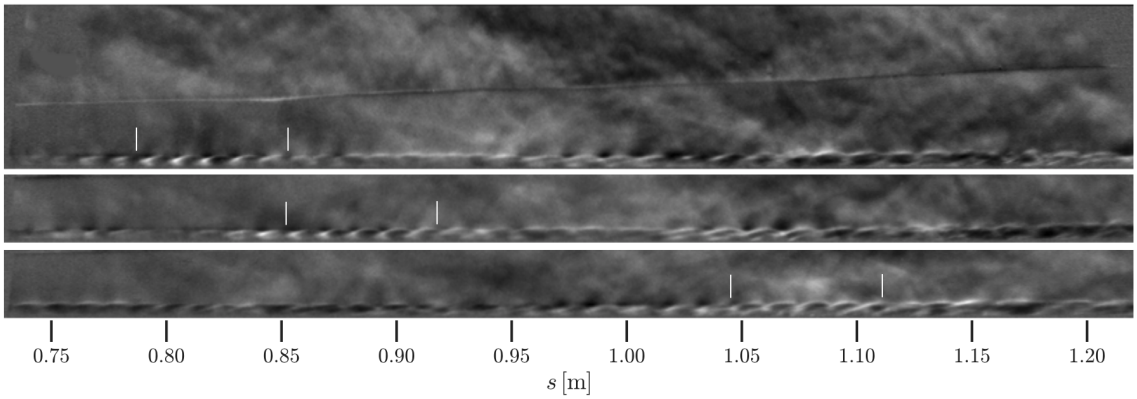

Figure 5.8: Enhanced image sequence showing the propagation and development of second-mode wavepackets from run 4119. The white markers indicate the approximate extent of a wavepacket in the first image and have been translated downstream in subsequent images using the mean wavepacket propagation speed.

The run 4119 waves retain this visual structure throughout the stages presented in figure 5.8, during which they are growing nonlinearly. Similar visual structure is observed for the nonlinear Mach-10 waves shown in figure 5.9. As the waves saturate in amplitude and begin to break down, the schlieren technique begins to lose its effectiveness as the wave structure in no longer uniform in the spanwise direction (Casper et al., 2014; Sivasubramanian and Fasel, 2014). Nonetheless, several observations can be made: first, waves that do persist to the far downstream portion of the intermittent region take on the appearance of a single connected periodic structure. Second, the visual onset of breakdown coincides with higher density content appearing across the vertical extent of the waves, until the structures take on a fully chaotic appearance indicative of complete breakdown to turbulence.

Bandpass-filtered versions of the images shown in figures 5.8 and 5.9, are presented in figures 5.10 and 5.11 to elucidate how different frequency content is distributed throughout the wave structure. Higher harmonic content lies in the

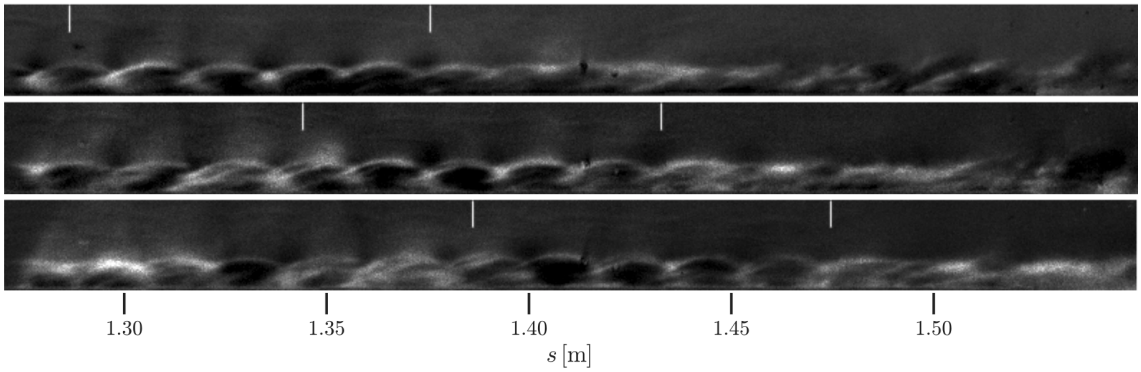

Figure 5.9: Enhanced image sequence showing the propagation and development of second-mode wavepackets from the Mach-10 freestream run 4017. The white markers indicate the approximate extent of a wavepacket in the first image and have been translated downstream in subsequent images using the mean wavepacket propagation speed.

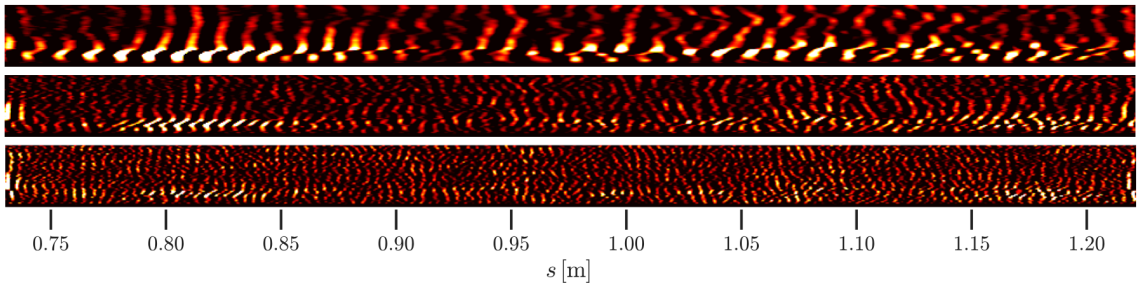

Figure 5.10: Figure 5.8 top image bandpass filtered around f_0 (top), $2f_0$ (middle), and $3f_0$ (bottom).

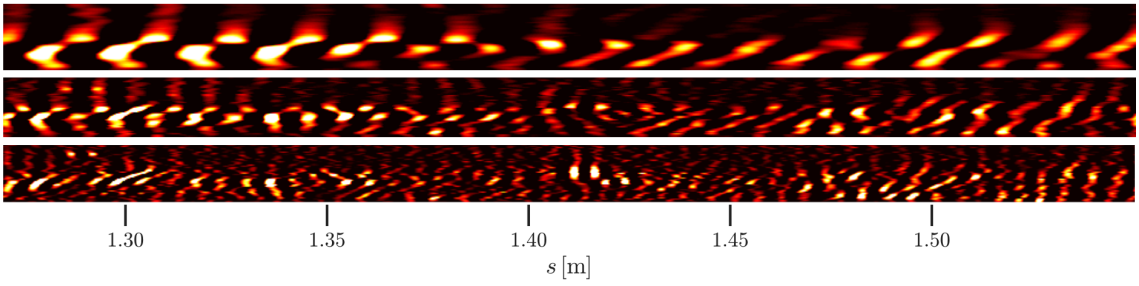

Figure 5.11: Figure 5.9 top image bandpass filtered around f_0 (top), $2f_0$ (middle), and $3f_0$ (bottom).

center of the wave at the same wall-normal location as the strongest fundamental content. The shape of the harmonic content generally resembles the fundamental content, with slightly lower minimum and maximum angles due to the location of the content in the center portion of the waves. We note that at the top of the waves near the edge of the boundary layer, fundamental frequency content appears to extend into the freestream at an inclination of $\approx 80°$ to the cone surface. This appears visually similar to the behavior anticipated for the case of the supersonic mode when the second mode synchronizes with the slow acoustic spectrum, resulting in the radiation of noise in the form of acoustic energy out of the boundary layer. Despite this mode being more commonly associated with cold-wall flows, Knisely and Zhong (2019) showed it to be theoretically possible in hot-wall flows (such as those examined here). For the current conditions, computational results provided by Bitter (private communication, November 2016) showed that the content at the boundary-layer edge is due to the shape of the density eigenfunction and not acoustic energy radiating into the freestream.

5.1.3.2 Wall-Normal Energy Distribution

In order to better understand the energy distribution throughout the waves at different stages of development, wall-normal power spectra are computed from the density-gradient signals generated from the individual waves. Time-reconstructed pixel-intensity signals are generated at wall-normal heights corresponding to the center of a pixel, with the length of the signal limited to a single wavepacket. The

calibration described in §3.2.3 is applied, and the power spectrum of the signal for each wall-normal height is computed and plotted.

The top left plot of figure 5.12 shows the spectra for the early developmental stage wavepacket in the top image of figure 5.1. The fundamental frequency disturbance power is primarily isolated to a single peak located at $y/\delta = 0.7-0.9$, and power appears in a first harmonic (frequency $\approx 2f_0$) at the same y/δ location. As the wavepacket propagates downstream it enters a more mature stage of development, with the harmonics growing slightly and a fundamental energy peak appearing at the outer edge of the wavepacket at $y/\delta = 1.1-1.2$. Rapid growth of the outer peak is observed, resulting in a distinct two-peak profile associated with the fundamental frequency content. This two-peak profile is a characteristic observed in most of the mature waves analyzed, and was reported in the wall-normal energy profiles observed by Laurence et al. (2016) and Grossir et al. (2014) in a Mach-8 and Mach-10 freestream, respectively. Contrary to Laurence et al. (2016) and Parziale et al. (2015), however, no fundamental energy peak is present at the wall for any of the wavepackets analyzed in this study.

Progressing to the run 4119 wavepacket profiles shown in figure 5.13, the mature waves share the same two-peak fundamental frequency profile. Strong harmonic content is present at $2f_0$, and at the $R = 1782$ station, weak harmonic content is present at $3f_0$ and $4f_0$. The waves retain this profile throughout the nonlinear growth stage until, as they approach the onset of transition, the wave amplitudes begin to decrease. By the last distribution shown in the bottom plot of figure 5.13, significant attenuation of the fundamental frequency content is observed and the

only higher harmonic content present is a weak first harmonic at $2f_0$.

The second-mode waves in the Mach-10 freestream run 4017 are notable for their harmonic content. The boundary layer is highly intermittent and the wavepackets appear in the latest stages of development. No calibration was performed for the Mach-10 schlieren setup; thus, it is important to note that the relative strength of the wall-normal PSD peaks only serve as a qualitative point of comparison. Figure 5.14 shows the wall-normal development of the wavepacket shown in figure 5.9. The two-peak profile is again present for the fundamental energy at $f_0 = 70\,\text{kHz}$ and a strong first harmonic is present at $2f_0$ with additional weaker content at $3f_0$. No demonstrable change in energy distribution occurs over the field of view or when compared to the Mach-14 waves, and the peaks at each frequency decrease in amplitude until the wavepacket breaks down to full turbulence.

Next, we consider the inclination of the structures in the $s-y$ plane at different stages of development. The fundamental structure angle is calculated by first bandpass filtering the signal reconstructed at each wall-normal location around the fundamental frequency of the second-mode disturbance. Cross-correlation coefficients for vertically separated signals are computed for various displacements, and the displacement corresponding to the highest valued coefficients is used to find the value of θ.

In figure 5.15 we show the computed angles for the wavepackets shown in figures 5.1, 5.8, and 5.9. In the earliest stage of development, (top plot, $R = 1567$) the fundamental structures begin by bending away from the wall, reaching a maximum inclination angle of approximately $140-150$ degrees at $y/\delta = 0.2-0.3$. The struc-

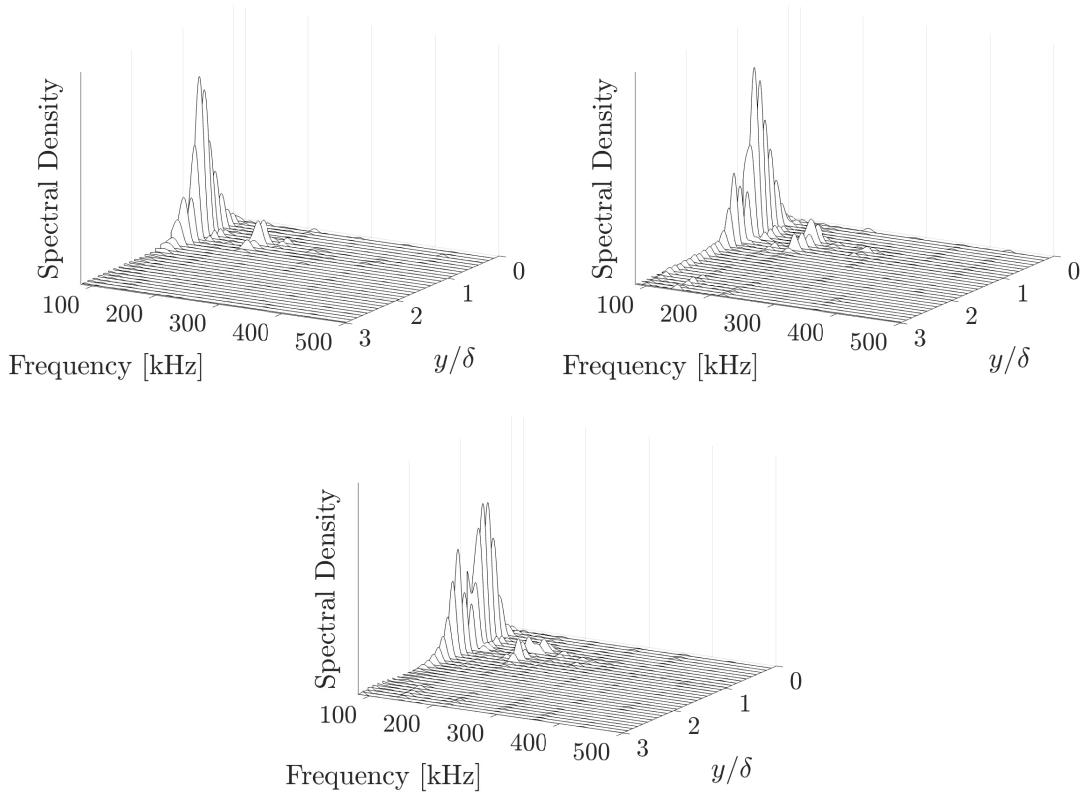

Figure 5.12: Wall-normal spectra for the run 4120 waves shown in figure 5.1 at $R = 1567$ (top left), $R = 1621$ (top right), and $R = 1660$ (bottom).

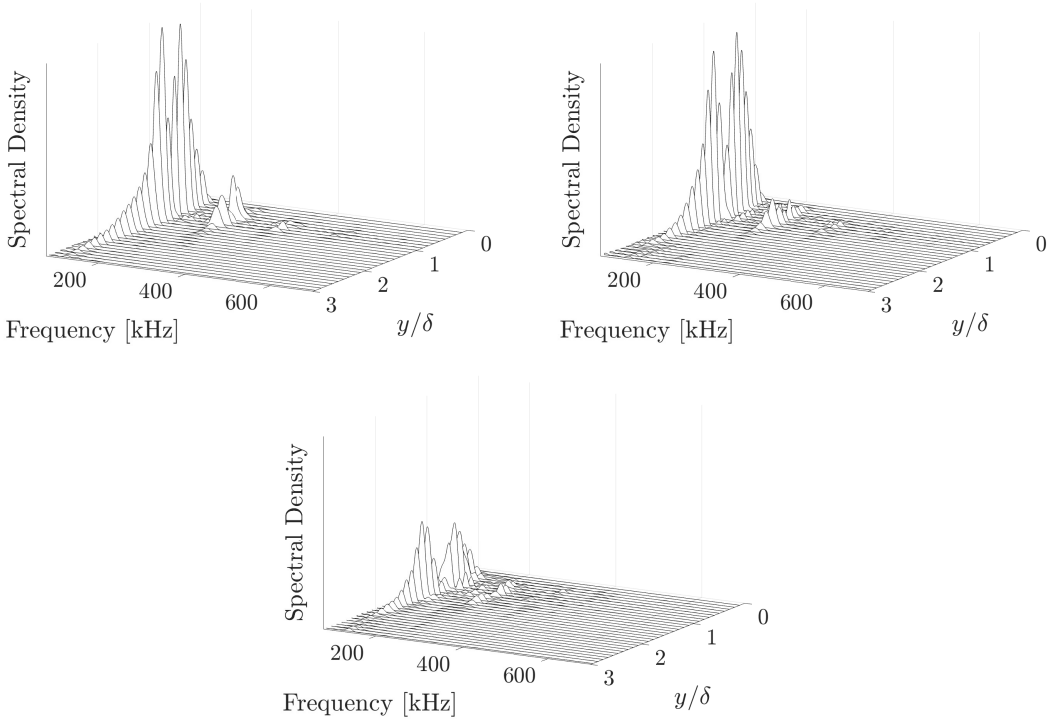

Figure 5.13: Wall-normal spectra for the run 4119 waves shown in figure 5.8 at $R = 1782$ (top left), $R = 1862$ (top right), and $R = 1990$ (bottom).

tures then slowly bend back towards the wall at a fairly constant rate until reaching a minimum angle of 18 degrees between $y/\delta = 1.0 - 1.1$. As the wavepackets enter more mature stages of development ($R = 1621$ and 1660), the structures, after bending away from the wall, bend more rapidly towards the wall before a small hump appears at $y/\delta = 0.75 - 0.80$. The hump reaches a maximum angle of approximately 60 degrees for the wavepacket at $R = 1621$. The appearance of this feature coincides with the onset of the development of the fundamental-energy two-peak profile present in the wall-normal power spectra, indicating that the structure tilts away from the surface of the cone in the wall-normal region between the two strongest regions of density gradient. This stability Reynolds number also roughly coincides with the location of deviation from the linear-growth regime in the time-averaged

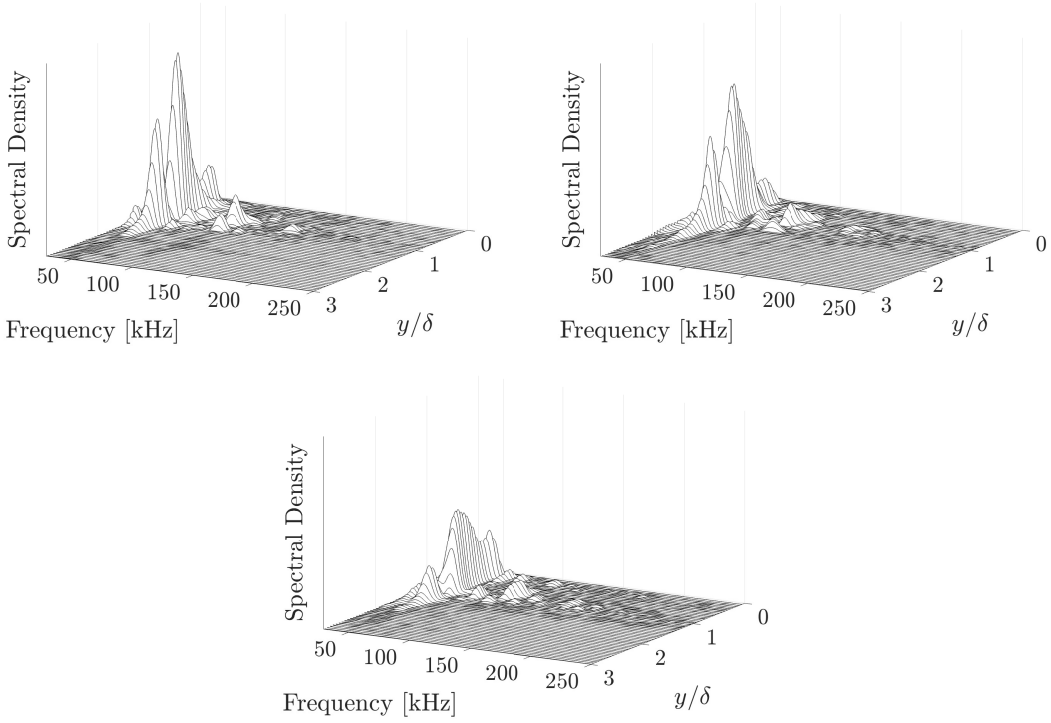

Figure 5.14: Wall-normal spectra for the run 4017 waves shown in figure 5.9 at $R = 1613$ (top left), $R = 1652$ (top right), and $R = 1676$ (bottom).

maximum N factors shown in figure 5.2. Moving further away from the cone surface, the structure rapidly begins to bend back towards the wall and reaches a minimum angle of $14-16°$ by $y/\delta = 1.0$.

Moving on to the middle plot of figure 5.15, we observe a similar overall shape for the fundamental structures of run 4119 with a slightly larger maximum angle of $150-160°$ at $y/\delta = 0.2-0.4$, and a slightly smaller minimum angle in the range of $8-10°$ at $y/\delta = 0.95-1.05$. Absent from any of the run 4119 wavepacket angles is the small hump at $y/\delta = 0.8$, despite the double-peak profile in the wall-normal distributions. Finally, the bottom plot of figure 5.15 shows the fundamental structure angles for the Mach-10 run-4017 wavepackets. The structures are similarly shaped to the other late-stage packets at Mach 14, exhibiting a maximum angle of $140-160°$

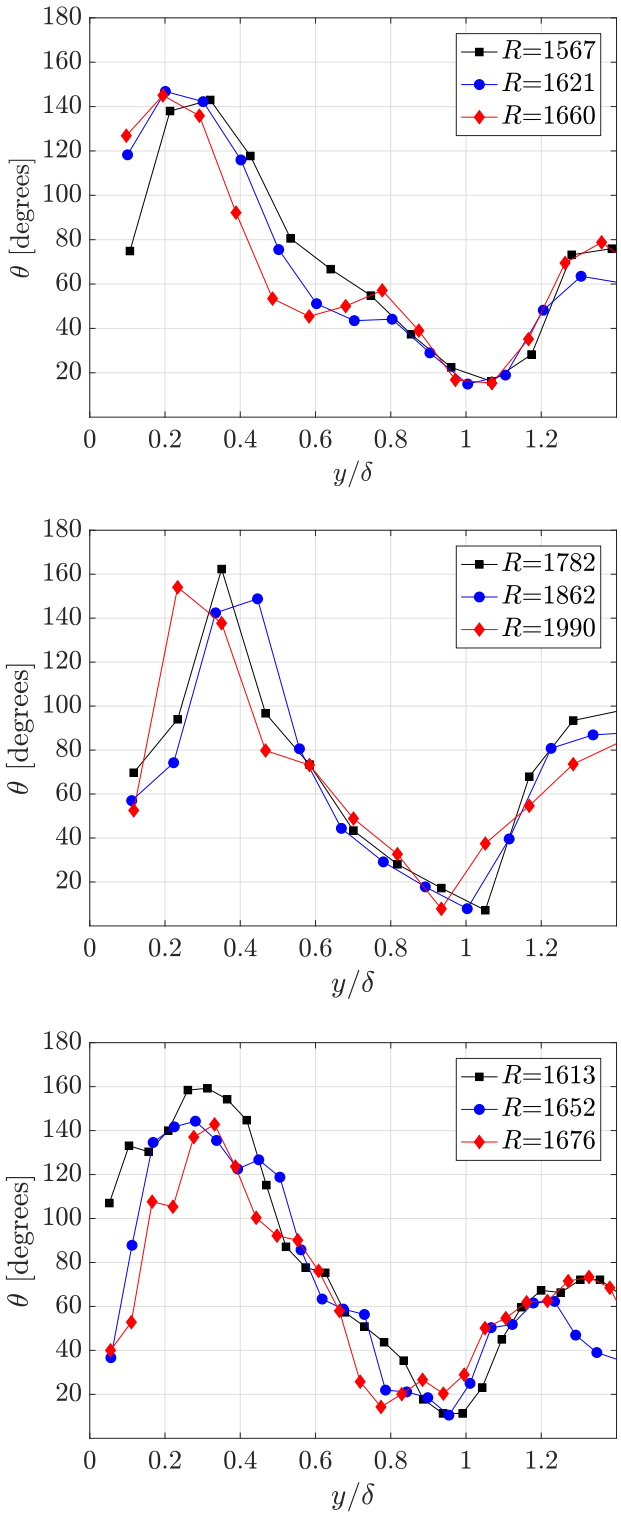

Figure 5.15: Fundamental structure angles for run 4120 (top), run 4119 (middle), and run 4017 (bottom).

at $y/\delta \approx 0.3$ and a minimum angle of $10-13°$ at $y/\delta \approx 1.0$.

In general, when harmonic content is present within a wavepacket, it is concentrated in the middle to upper portion of the wave, as demonstrated by the wall-normal energy distributions and bandpass-filtered images. The harmonic content also appears roughly centered in spanwise extent; this is clearly observed in the wavepacket in the left side of the filtered images shown in figure 5.10. The harmonic structures tend to take on the shape of the fundamental structures within the range of $y/\delta = 0.5-1.2$, but they do not tend to reach the same maximum or minimum structure angles of the fundamental features. Typically, the minimum value for the harmonic structure angles is $20-30°$.

5.1.3.3 Spanwise Pressure Traces

A non-uniform timing offset between the visualizations and the pressure traces eliminated the ability to make simultaneous observations on individual wavepacket development using both measurement techniques for the Tunnel 9 dataset. However, the pressure data can still provide information on the mean wavepacket circumferential extent. Figures 5.16 and 5.17 show pressure traces for representative second-mode wavepackets recorded by the spanwise PCB sensor array for runs 4119 and 4118 (the waves of runs 4123 and 4120 were too weak to analyze). The traces are presented in spatial streamwise coordinates by converting the pressure time signals using the mean wavepacket propagation speed. Both unfiltered traces and traces filtered around $f_0 \pm 10\,\mathrm{kHz}$ are presented; traces filtered around $2f_0 \pm 10\,\mathrm{kHz}$ are

also presented for run 4119.

Two methods are used to compute the wave extent. In the first, the coherence of the spanwise signals is computed for the fundamental and first-harmonic frequencies defined at the streamwise location of the spanwise array. Figure 5.18 shows the coherence values plotted as a function of circumferential separation for run 4119. Defining the feature width based on a coherence limit of 0.2, the circumferential scale is $2\delta - 2.5\delta$ for the fundamental frequency content and approximately 1.4δ for the first harmonic content. Too much intermittency is present in run 4118 to provide meaningful results, with the coherence level being everywhere below 0.2 between the nearest circumferentially offset sensors. The second method is implemented as follows. Pressure traces of individual waves are first identified and filtered around the frequencies of interest. A Gaussian is then fitted to the spanwise sensor traces at the streamwise location corresponding to the center of the pressure footprint. A cutoff criterion related to the maximum value of the Gaussian peak can then be used to define the feature width. The arbitrary nature of the cutoff criterion makes the absolute value of the feature widths measured by this method quantitatively meaningless; however, qualitative comparisons can be made for different unit-Reynolds-number conditions. Using a criterion of the full width at half maximum of the Gaussian fit, the normalized width (ξ/δ) of the higher unit-Reynolds-number run 4118 wave fundamental frequency content is approximately 30% less than the waves of run 4119. Overall, the results from both methods agree with previous hot-wire measurements of Kimmel et al. (1996) who reported second-mode circumferential scales to be 4δ or less and decrease with increasing unit Reynolds number. Additionally, because

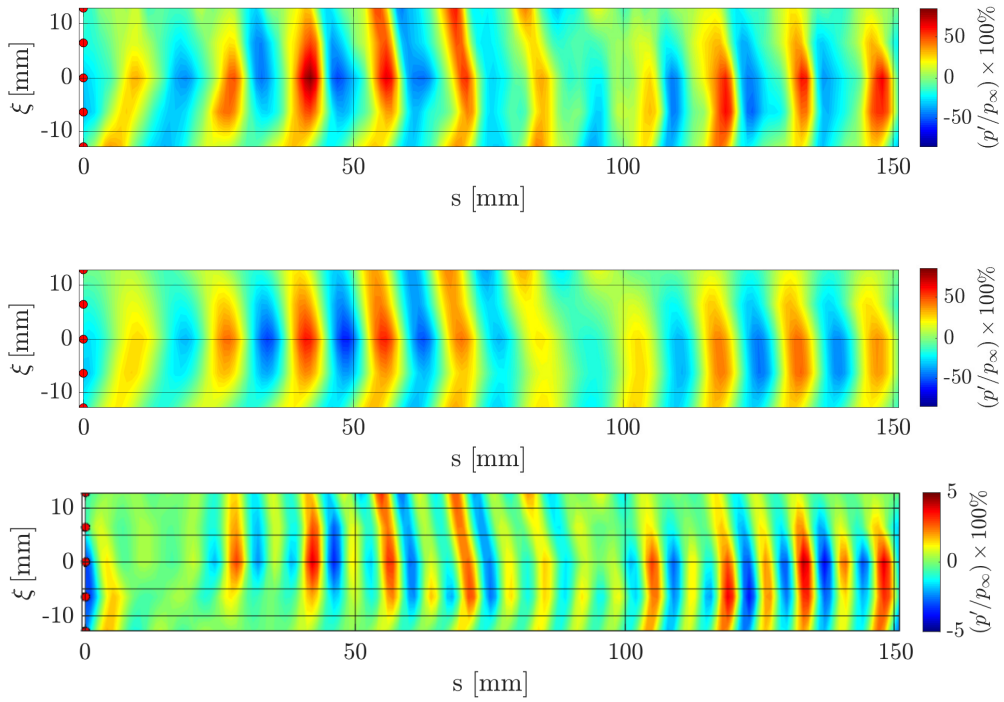

Figure 5.16: Run 4119 spanwise pressure distributions (with t converted to s through the mean propagation speed) of the unfiltered signals (top), signals filtered around $f_0 \pm 10\,\text{kHz}$ (middle), and signals filtered around $2f_0 \pm 10\,\text{kHz}$ (bottom). The red dots indicate the locations of the PCB sensors.

the second method computes the circumferential extent of individual waves and not the coherence of the entire time series, it can be concluded that the reduction in wave span with increasing unit Reynolds number is indeed a property of the waves and not a result of increased intermittency of the boundary layer.

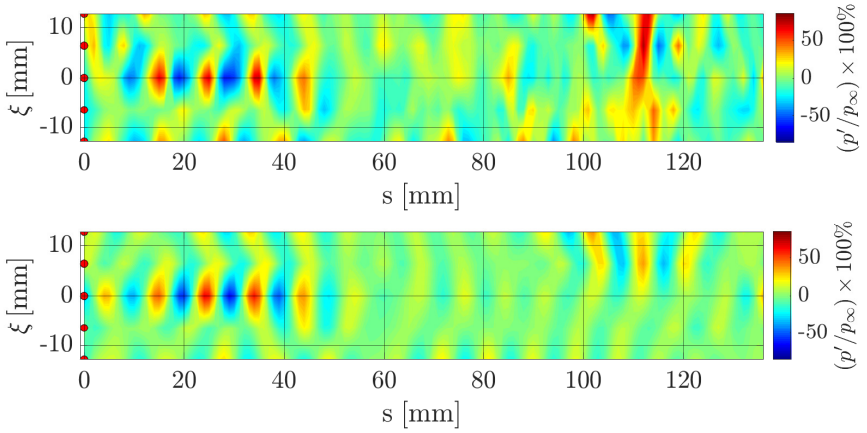

Figure 5.17: Run 4118 spanwise pressure distributions (with t converted to s through the mean propagation speed) of the unfiltered signals (top) and signals filtered around $f_0 \pm 10\,\mathrm{kHz}$ (bottom). The red dots indicate the locations of the PCB sensors.

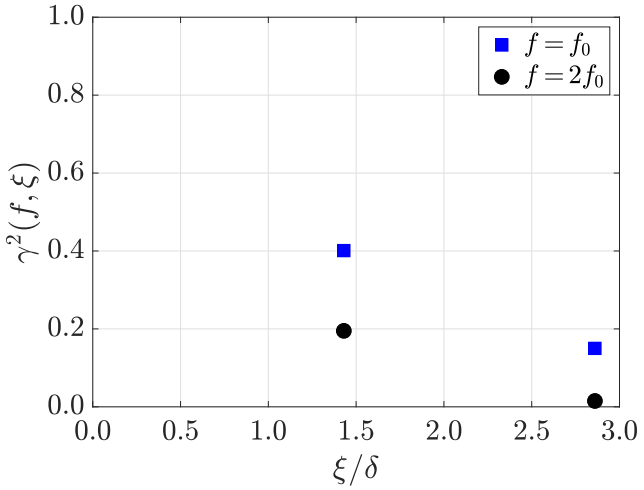

Figure 5.18: Spanwise pressure signal coherence computed for run 4119.

LT Run #	M_∞	Re_∞/m [1/m$\times 10^6$]	ρ_∞ [g/m^3]	T_∞ [K]	u_∞ [m/s]
17	6.14	4.90	18.9	54	903
9	6.14	7.11	27.4	54	904
30	6.14	9.31	35.8	54	903

Table 5.5: Computed freestream (subscript ∞) conditions for the AFRL LT sharp-cone experiments.

5.2 AFRL Ludwieg Tube Experiments[2]

5.2.1 Test Conditions

Data are presented for three experiments performed with the sharp-nose model configuration in the AFRL Ludwieg Tube. For all experiments, the cone model was installed at zero incidence ($\pm 0.5°$) to the freestream. The stagnation temperature is 450 K, resulting in a stagnation enthalpy of 0.46 MJ/kg; prior to the start of all experiments, the model is at room temperature resulting in a wall-to-stagnation temperature ratio of approximately 0.6. Additional information on the freestream conditions can be found in table 5.5. As previously described in §2.1.2, the Ludwieg Tube produces two 100-ms duration steady-flow test times. Data are collected and analyzed for the second of these two steady-flow periods and visualizations are generated using the calibrated high-speed schlieren system. Configuration details for the schlieren system are provided in table 5.6

[2]This material is adapted from Jagde et al. (2019)

LT Run #	Resolution [pixels]	Frame Rate [f.p.s]	Scale [pixels/mm]	Location s [mm]	Wave Behavior
17	1280×176	172,131	11.5	257 – 363	Linear Growth
9	1280×368	172,131	11.2	253 – 367	Linear to Nonlinear Growth
30	1280×320	234,636	6.9	185 – 369	Linear Growth to Breakdown

Table 5.6: Camera parameters used for different experimental conditions.

LT Run #	u_p [m/s]	95% confidence [m/s]	u_p/u_e	Wavepackets Analyzed
17	787	28	0.95	8906
9	778	53	0.94	10,000
30	804	36	0.97	7742

Table 5.7: Wavepacket propagation speeds.

5.2.2 Time-Averaged Results

Mean wavepacket propagation speeds are again computed using the same cross-correlation techniques applied to the Mach-14 dataset, and the calculated results are presented in table 5.7. The wave phase speeds are between $0.94u_e - 0.97u_e$. The speeds are slightly higher than those computed at Mach 14, but still within a reasonably expected range based on previous literature.

Vibration of the tunnel induced by the startup of the flow, combined with incomplete isolation of the schlieren optics from the facility floor, caused the knife edge to move during the steady-flow test period; in turn, this caused a darkening and brightening of the background intensity that was sinusoidal in time. Since the camera frame rate was significantly higher than the vibration frequency of approximately 20 Hz, the background intensity change is minimal between images. To account for this in the signal reconstruction, the image where the background intensity is the same as the flow-off conditions is identified and frames are identified

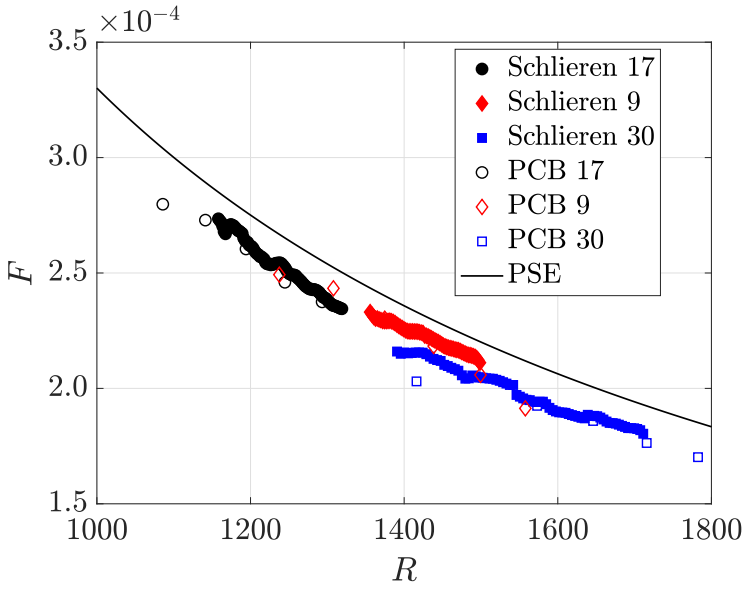

Figure 5.19: Dimensionless most-amplified second-mode frequencies.

on either side of this image for which the background is within ±5% of the flow-off background intensity. These images are then used to generate the reconstruction, providing 3 sets of approximately 2000 – 3000 useful images per experiment.

Figure 5.19 presents the dimensionless most-amplified second-mode frequencies for each unit-Reynolds-number condition along with the PSE results. Good agreement is observed between the frequencies measured using the schlieren visualizations and PCB sensors. Across the measurement region, the PSE computations give a 5% overprediction; considering the constant offset, this may be the result of a slight misalignment of the cone from zero incidence. Maximum N factors computed for these frequencies are presented in figure 5.20. The slope of the weighted least-squares linear fit of the schlieren-computed max N factors in the second-mode linear-growth regime is $\mathrm{d}N/\mathrm{d}R = 5.05 \times 10^{-3}$, approximately 10% higher than the slope of $\mathrm{d}N/\mathrm{d}R = 4.65 \times 10^{-3}$ computed from the PSE. In agreement with the pre-

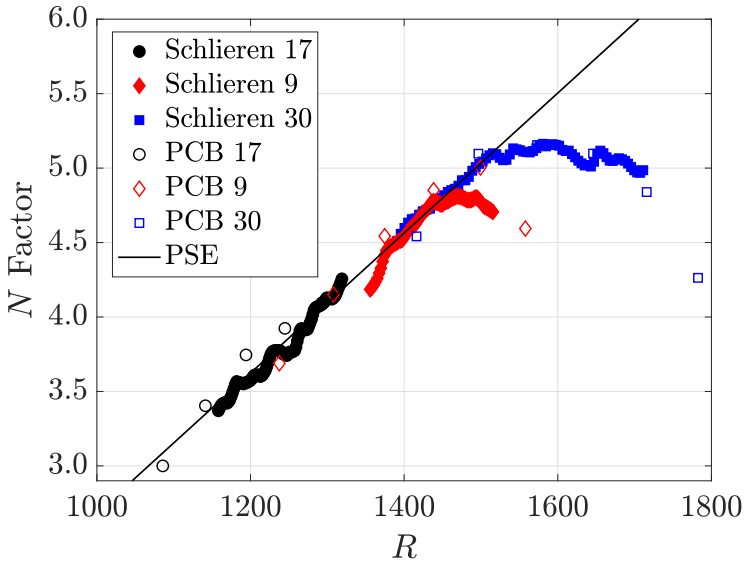

Figure 5.20: Maximum N factors.

dictions of Mack (1975), the slope is approximately 60% higher than that measured for the Tunnel 9 Mach-14 experiments, indicating a higher growth rate for the lower freestream Mach number. In addition to the linear growth for all conditions, nonlinear growth and saturation is observed for the run 30 and run 9 waves. Deviation from the linear-growth regime and saturation occurs at a lower stability Reynolds number for the run 9 waves; this is consistent with the Mach-14 results and predictions of Marineau et al. (2019).

N factors as a function of frequency and stability Reynolds number computed from the reconstructed schlieren signals are presented in figure 5.21. In dimensional terms, the most-amplified second-mode frequencies lie in the range 165 – 310 kHz. For the two higher unit-Reynolds-number conditions, higher harmonic content is present at a frequency of approximately twice the fundamental second-mode frequency, but in neither case is a second harmonic visible. The initially weak first-

harmonic content is amplified with increasing streamwise location, particularly once the waves enter the nonlinear-growth stage. No comparison to PCB data is available as the higher frequencies are outside of the range over which the sensors provide reliable data.

The nonlinear interactions leading to the harmonics visible in figure 5.21 are presented in the bicoherence plots of figure 5.22. Beginning with run 9, quadratic phase locking is observed in interactions at $f_0 + f_0 \rightarrow 2f_0$ as well as $2f_0 - f_0 \rightarrow f_0$. The interactions are initially weak, with b^2 values of 0.069 and 0.11, respectively. Moving from the upstream station to the downstream station, the two interactions become stronger, increasing to 0.092 and 0.14, and widen in bifrequency space. Consistent with the Mach-14 results, the interactions precede the maximum N-factor saturation and presence of harmonic power in figure 5.21. In the lower plots of figure 5.22, showing the bicoherence computed for run 30, the $f_0 + f_0 \rightarrow 2f_0$ and $2f_0 - f_0 \rightarrow f_0$ interactions are present, along with interactions involving a second harmonic at $2f_0 + f_0 \rightarrow 3f_0$, $3f_0 - f_0 \rightarrow 2f_0$, and $3f_0 - 2f_0 \rightarrow f_0$. The interactions observed for run 30 have significantly higher bicoherence values than those of run 9, reaching a maximum b^2 value of 0.34 for the $2f_0 - f_0 \rightarrow f_0$ interaction at $R = 1551$. Further downstream, the power of the phase-locked interactions decreases until the boundary layer becomes fully turbulent.

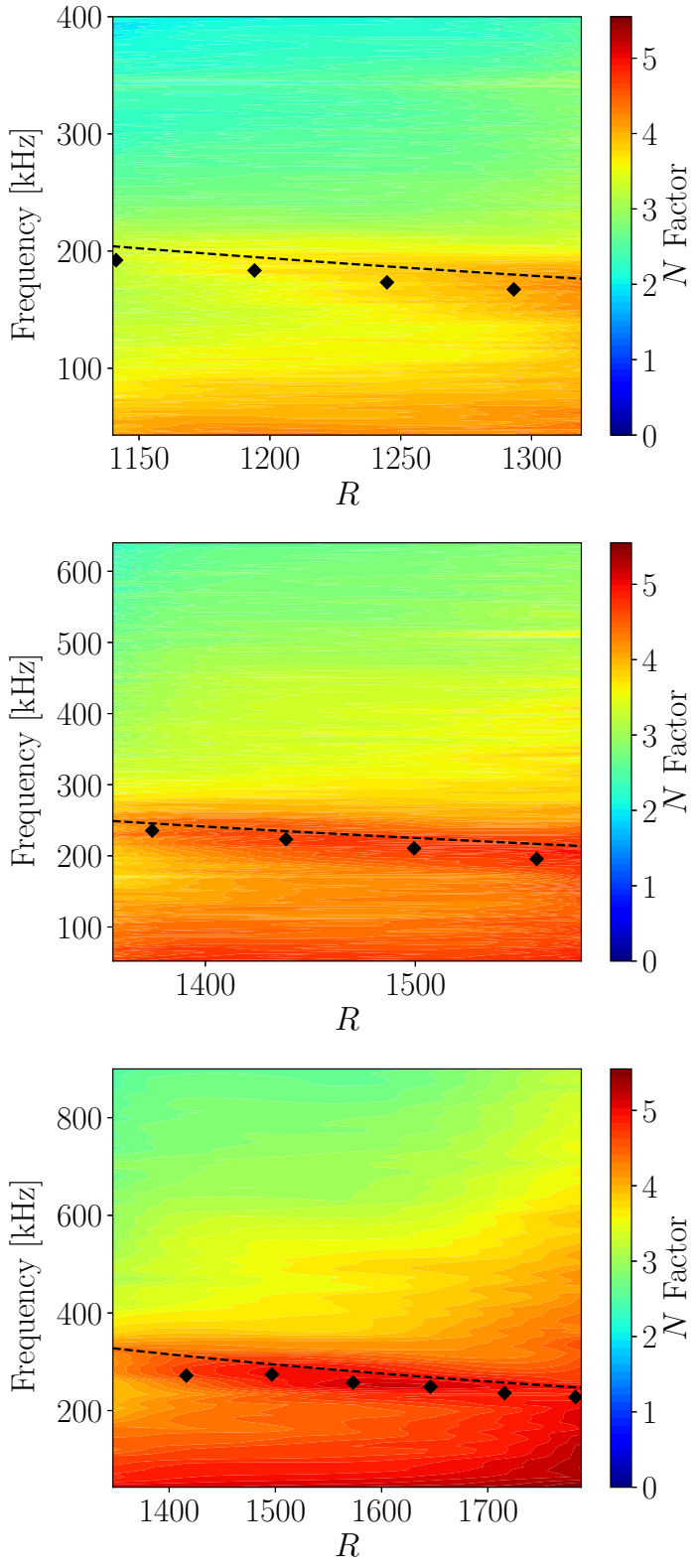

Figure 5.21: N factors as a function of frequency and R for run 17 (top), run 9 (middle), and run 30 (bottom). The dashed line indicates the PSE fit and the black diamonds indicate PCB measurements of f_0.

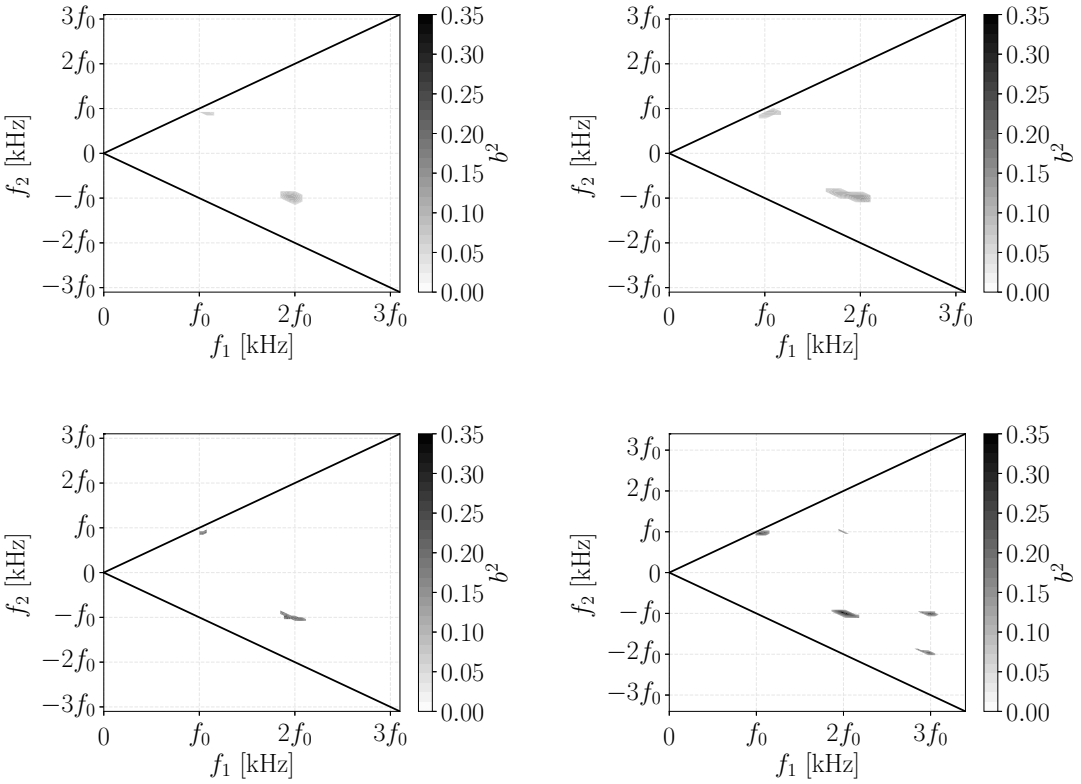

Figure 5.22: Bicoherence b^2 values calculated for run 9 (top) at $R = 1390$ (top left) and $R = 1475$ (top right), and for run 30 (bottom) at $R = 1484$ (bottom left) and $R = 1551$ (bottom right). The black lines indicate planes of symmetry. The frequencies are represented by the fundamental disturbance frequency at the given streamwise location.

5.2.3 Individual Wavepacket Development

5.2.3.1 Wavepacket Appearance

Sample images from runs 9 and 30 are presented in figures 5.23 and 5.24. Images from run 17 are omitted as the waves are extremely weak for extracting meaningful insights by visual inspection. In figure 5.23, the waves appear slanted and become curved by the most downstream location. Overall, the visual structure is similar to the earlier stage waves observed in the Tunnel 9 data. The run 30 waves shown in figure 5.24 take on a more highly curved appearance as is anticipated since this more mature stage coincides with the nonlinear-wave growth identified in the time-averaged measurements. The weak harmonic content seen in the filtered images of figure 5.25 again is concentrated about the center of the waves both in the wall-normal and streamwise coordinate.

5.2.3.2 Wall-Normal Energy Distribution

The following analysis focuses on the run 30 waves as they span the largest number of developmental stages. In its earliest stage of development, shown in figure 5.26 (top left), the wavepacket contains fundamental frequency content at 270 kHz concentrated between $y/\delta = 0.8 - 1.1\delta$. The fundamental content is significantly amplified by the next downstream station (top right), where we observe the appearance of the distinct double-peak profile. By $t_0 + 42.6\,\mu$s, the fundamental distribution has distinct peaks at 0.88δ and 1.08δ, and weak first harmonic content in the 520 kHz

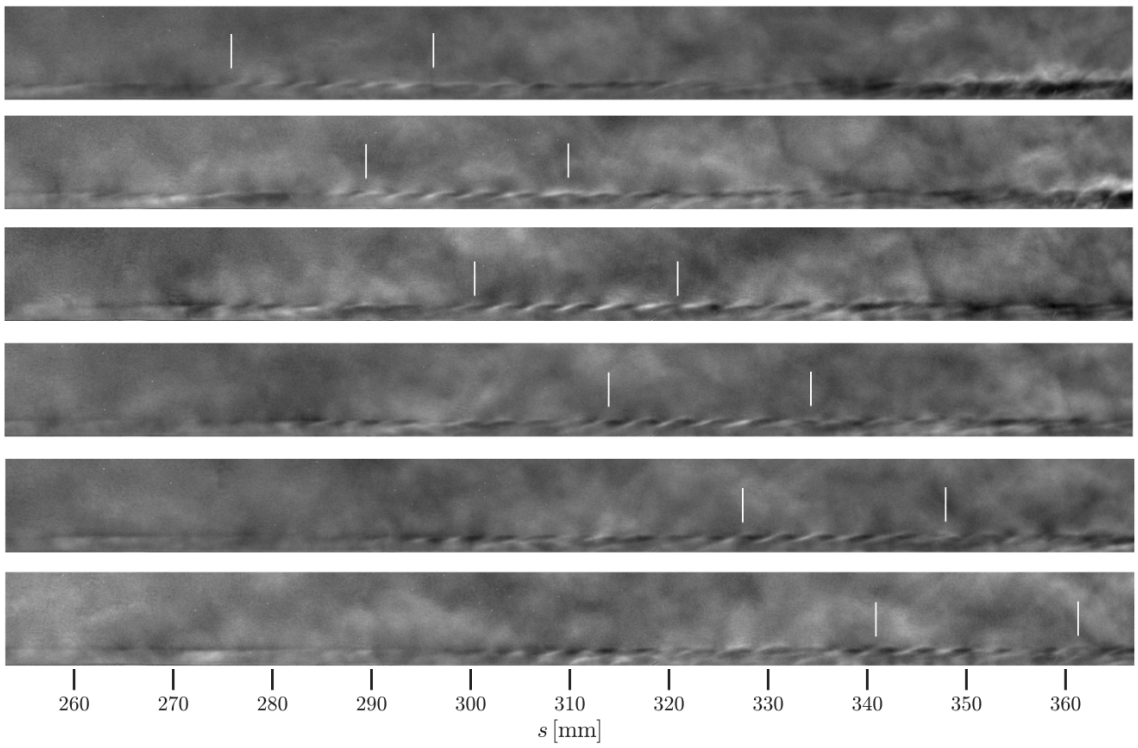

Figure 5.23: Enhanced image sequence showing the propagation and development of a wavepacket from run 9. The vertical white lines indicate the approximate extent of the wavepacket in the first image and have been translated downstream in subsequent images using the mean propagation speed. The top image corresponds to time t_0, with subsequent images separated by $\Delta t = 23.2\,\mu s$.

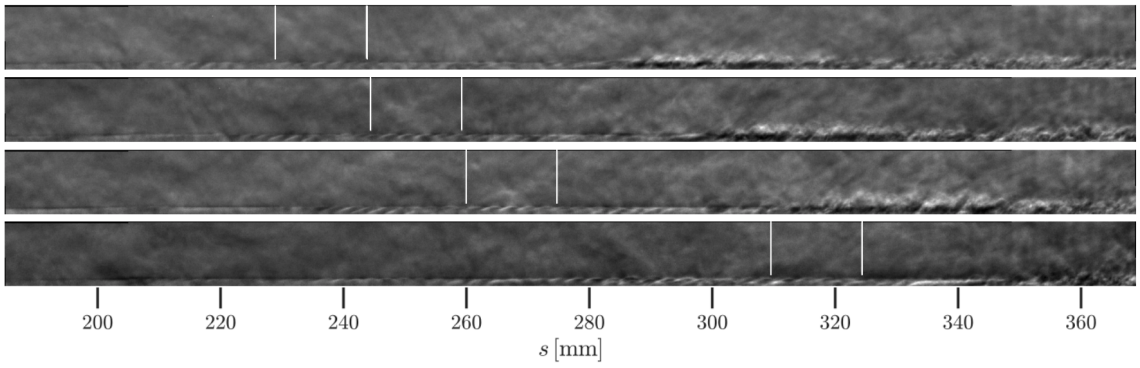

Figure 5.24: Enhanced image sequence showing the propagation and development of a wavepacket from run 30. The vertical white lines indicate the approximate extent of the wavepacket in the first image and have been translated downstream in subsequent images using the mean propagation speed. The top image corresponds to time t_0, with subsequent images occurring at times $t_0 + 21.3\,\mu s$, $t_0 + 42.6\,\mu s$, and $t_0 + 106.5\,\mu s$.

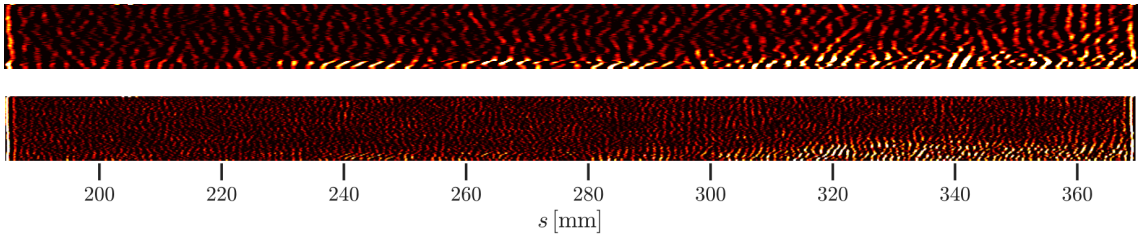

Figure 5.25: Figure 5.24 image captured at time $t_0 + 42.6\,\mu s$ filtered around f_0 (top) and $2f_0$ (bottom).

range becomes visible at the same wall-normal locations. Progressing further downstream (not shown), the fundamental and harmonic peaks decrease in power until no distinct peaks remain and the wavepacket is on the verge of full breakdown to turbulence. The observations are qualitatively consistent with the findings presented for mature second-mode wavepackets developing in a Mach-14 freestream; again, no near wall peak is observed in any of the present wavepackets.

The computed fundamental structure angles for the wavepacket shown in figure 5.24 are presented in the lower right plot of figure 5.26. The overall structure of the waves is similar to those at Mach 10 and 14, with the exception of the angle magnitudes in the near-wall region. Initially, the waves are bent towards the freestream with the maximum lying between $y/\delta = 0.2 - 0.4$, but the waves reach a maximum angle of roughly $120°$ in contrast to the maximum $140° - 160°$ observed for the higher Mach number conditions. Minimum angles lie in the range $8 - 16°$ at $y/\delta = 0.82 - 1.0$.

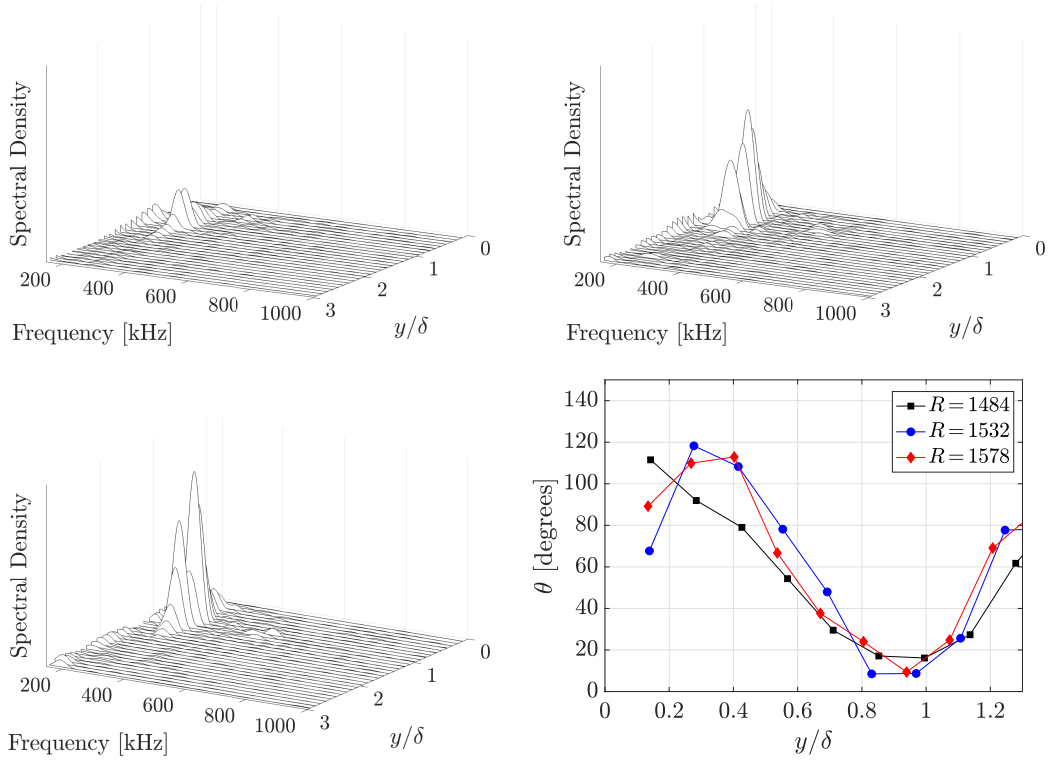

Figure 5.26: Run 30 wall-normal spectra for the waves shown in figure 5.24 computed at times: t_0, $R = 1484$ (top left); $t_0 + 21.3\,\mu s$, $R = 1532$ (top right); $t_0 + 42.6\,\mu s$, $R = 1578$ (bottom left). Fundamental structure angles (bottom right).

5.2.3.3 Spanwise Pressure Traces

The spanwise extent of the second-mode waves can be examined using the PCB sensor spanwise array composed of three PCB132B sensors located at $s = 316\,\text{mm}$ and centered on the ray of streamwise sensors. For each experiment, the coherence as a function of frequency is computed between each of the sensors in the array over the steady-flow period, generating coherence measurements for circumferential separations of 5.72 mm and 11.43 mm.

At the lowest unit-Reynolds-number condition run 17, the signal coherence at the fundamental second-mode frequency of 178 kHz is 0.52 at a circumferential separation of 5.72 mm and 0.28 at 11.43 mm. Using a coherence cutoff criterion of 0.2 to define the pressure disturbance width, the span of the second-mode pressure disturbance at the wall is slightly greater than 3.9δ, where δ is the local boundary-layer thickness. Using the same criterion, the higher-Reynolds-number condition runs 9 and 30 wave extents are between $5.72 - 11.43\,\text{mm}$ corresponding to $2.3\delta - 4.6\delta$ for run 9 and $2.6\delta - 5.2\delta$ for run 30. By fitting a Gaussian to the three circumferential measurement locations (using a coherence value of 1 at $\xi = 0$), the extents are more precisely estimated as 4.20δ for run 17, 3.16δ for run 9, and 3.11δ for run 30. While more densely spaced PCB sensors would be required to make higher-accuracy measurements of the second-mode wave spanwise extents, the results are again similar to the spanwise extents reported by Kimmel et al. (1996), showing the pressure footprint to be fairly limited in the circumferential direction.

5.3 AFRL High-Reynolds-Number Facility Experiments[3]

5.3.1 Test Conditions

Three experiments performed at different unit-Reynolds-number conditions are analyzed from the AFRL Mach-6 High-Reynolds-Number facility. The facility operates at significantly higher freestream unit Reynolds numbers and densities than either Tunnel 9 or the AFRL LT. This produces a more challenging environment for making boundary-layer transition measurements; namely, the high-density freestream produces an extremely thin boundary layer ($\delta = 300\,\mu\text{m} - 1.2\,\text{mm}$) on the cone resulting in second-mode frequencies in the megahertz range. At present, no surface instrumentation is capable of reliably resolving frequencies in this range. The previous studies of Stetson (1983) performed in this facility relied exclusively on mean surface measurements, and no experimental confirmation of second-mode instability waves was made prior to the current study. Data are analyzed for the sharp-nose configuration at stagnation pressures of $4.87 - 6.22\,\text{MPa}$, the lower end of the tunnel stagnation-pressure operational envelope. While data were collected at higher pressures, the boundary layer was too thin to extract meaningful results. Stagnation enthalpies were $\approx 0.58\,\text{MJ/kg}$, and the wall-to-stagnation temperature ratio was 0.54. Freestream conditions can be found in table 5.8.

A high-density freestream also presents unique challenges for the schlieren setup. The visualization region was limited to the most upstream portion of the

[3]This material is adapted from Jewell et al. (2018)

test section window as transition occurs near the front of the cone, and physical limitations constrain the relative location of the cone to the front of the optical access. Employing a free-standing lens to focus the image into the camera (see §3.1) resulted in a maximum of 7 pixels spanning the boundary layer, with a range of $4-7$ pixels for the different unit-Reynolds-number conditions. While the observed most-amplified second-mode frequencies are only weakly dependent on the wall-normal location of the signal reconstruction, wave amplitudes are highly sensitive as the density eigenfunction is a function of the wall-normal coordinate. Reduced pixel density within the boundary layer results in significant spatial integration, subsequently introducing error into the amplitude measurement. In addition to the difficulties associated with the magnification, in post-processing it was observed that the 10-m focal length calibration lens did not produce a sufficiently large density gradient to map the pixel intensities to density gradients, i.e., the highest intensity pixels in the flow-on schlieren images had higher counts than those in the brightest portion of the lens. A lack of a unique mapping for the highest pixel intensities leads to an inability to calibrate the images; consequently, the amplitudes presented only serve as qualitative assessments. Figures 5.27 and 5.28 show sample enhanced schlieren images, and table 5.9 presents the computed wavepacket propagation speeds. Note that, as the camera resolution is fixed to the maximum width of 1280 pixels, the extremely thin boundary layer does allow approximately $200\,\delta$ to be viewed in the streamwise direction. For all cases, the viewing location on the cone surface was $121.7-227.6$ mm, and the camera frame rate was 368,421 frames per second.

HRN Run #	p_0 [MPa]	M_∞	Re_∞/m [1/m$\times 10^6$]	ρ_∞ [g/m^3]	T_∞ [K]	u_∞ [m/s]
450	4.87	5.9	30.7	154	76.7	1038
452	5.53	5.9	35.1	176	76.7	1038
453	6.22	5.9	39.5	198	76.7	1038

Table 5.8: Reservoir (subscript 0) and computed freestream (subscript ∞) conditions for the AFRL High-Reynolds-Number facility tests.

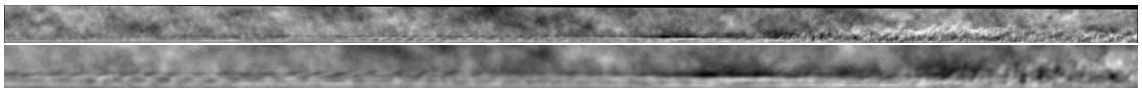

Figure 5.27: Sample images from run 450. Enhanced at original magnification (top). Enhanced, cropped, and enlarged to 4x magnification using interpolation (bottom).

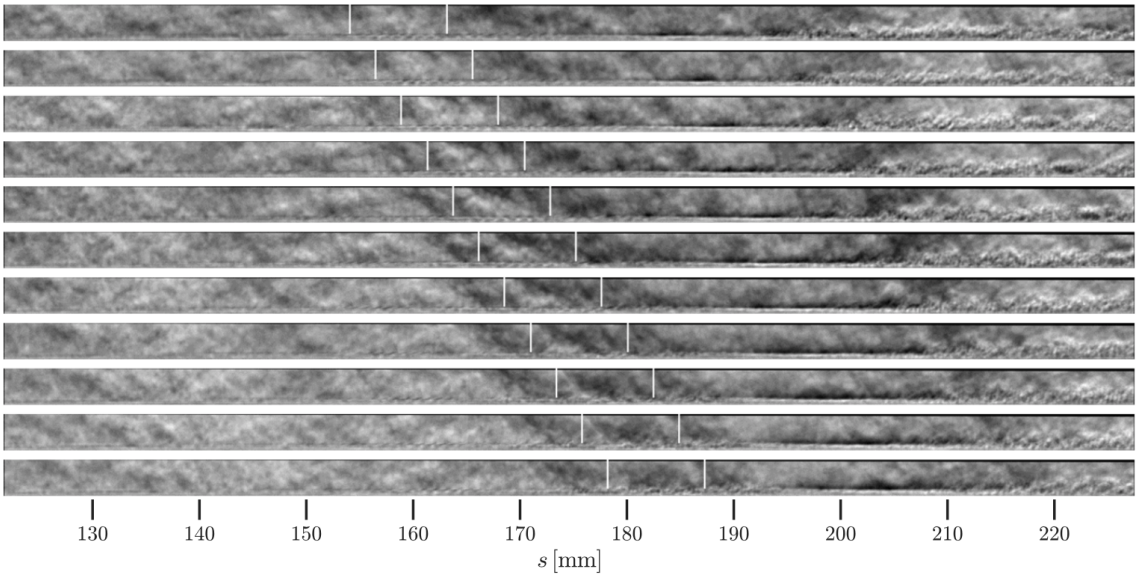

Figure 5.28: Enhanced image sequence from run 450 showing the propagation of a wavepacket. The vertical white lines indicate the approximate extent of the wavepacket in the first image and have been translated downstream in subsequent images using the mean propagation speed.

HRN Run #	u_p [m/s]	95% confidence [m/s]	u_p/u_e	Wavepackets Analyzed
450	890.8	53.0	0.92	5615
452	896.6	66.6	0.93	7010
453	892.2	54.0	0.83	7000

Table 5.9: Wavepacket propagation speeds.

5.3.2 Time-Averaged Results

Time-reconstructed pixel-intensity signals were generated using 5000 images (13.6 ms) from each experiment. A comparison between the schlieren-measured frequencies and PSE computations is provided in figure 5.29. Good agreement is observed for each unit-Reynolds-number condition. Figure 5.30 presents the log amplitudes of the pixel-intensity signals for each frequency and downstream location. The color scale in this case is arbitrary logarithmic units, as the calibration is not available to convert amplitudes to N factors. The most-amplified frequencies rise slightly in frequency with increasing unit Reynolds number over the three cases, ranging from a minimum of 757 kHz to a maximum of 1066 kHz. The transition front, visible as the region of broadband disturbances downstream of the narrowband second-mode instability, clearly moves forward with increasing unit Reynolds number. No higher harmonics are visible in the spectra of figure 5.30; this may be a consequence of the relatively low pixel counts in the extremely thin boundary layers, as the harmonics have been shown to be concentrated in the center of the waves and have limited vertical extent compared to the fundamental content.

Although no power is present in the spectra at higher harmonic frequencies prior to breakdown, nonlinear interactions in the form of quadratic phase locking can still be present. The bicoherence computed for run 453 is seen in figure 5.31. Two weak interactions are present: $f_0 + f_0 \rightarrow 2f_0$ and $2f_0 - f_0 \rightarrow f_0$. We note the extremely high frequencies associated with the first harmonic: at $s = 133.3$ mm, $2f_0 = 2120$ kHz. Both the sum and difference interaction only exist over a very small

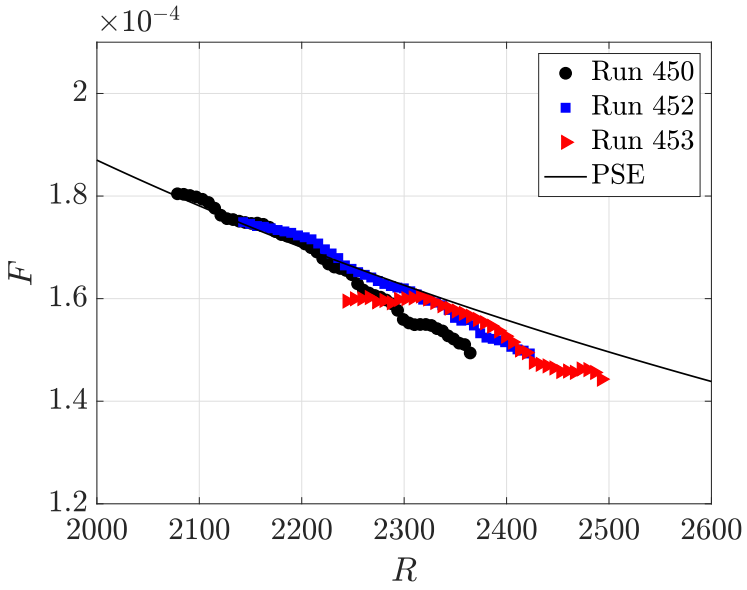

Figure 5.29: Dimensionless most-amplified second-mode frequencies.

streamwise distance, first appearing at $s = 133.3\,\text{mm}$ and completely disappearing by $s = 145.0\,\text{mm}$. The interactions are also notable for their weak b^2 values, reaching a maximum of only 0.18. In general, the interactions evolve similarly to those previously observed, increasing in b^2 value from the upstream to downstream station and spreading in bifrequency space, and then decreasing in value until no phase-locked interactions remain.

5.4 Error Analysis

There are a number of error sources associated with the calculation of the second-mode most-amplified frequencies and N factors from the schlieren images. We consider the two largest contributors to the error: the computed wavepacket propagation speed and identification of the second-mode peak frequency and amplitude.

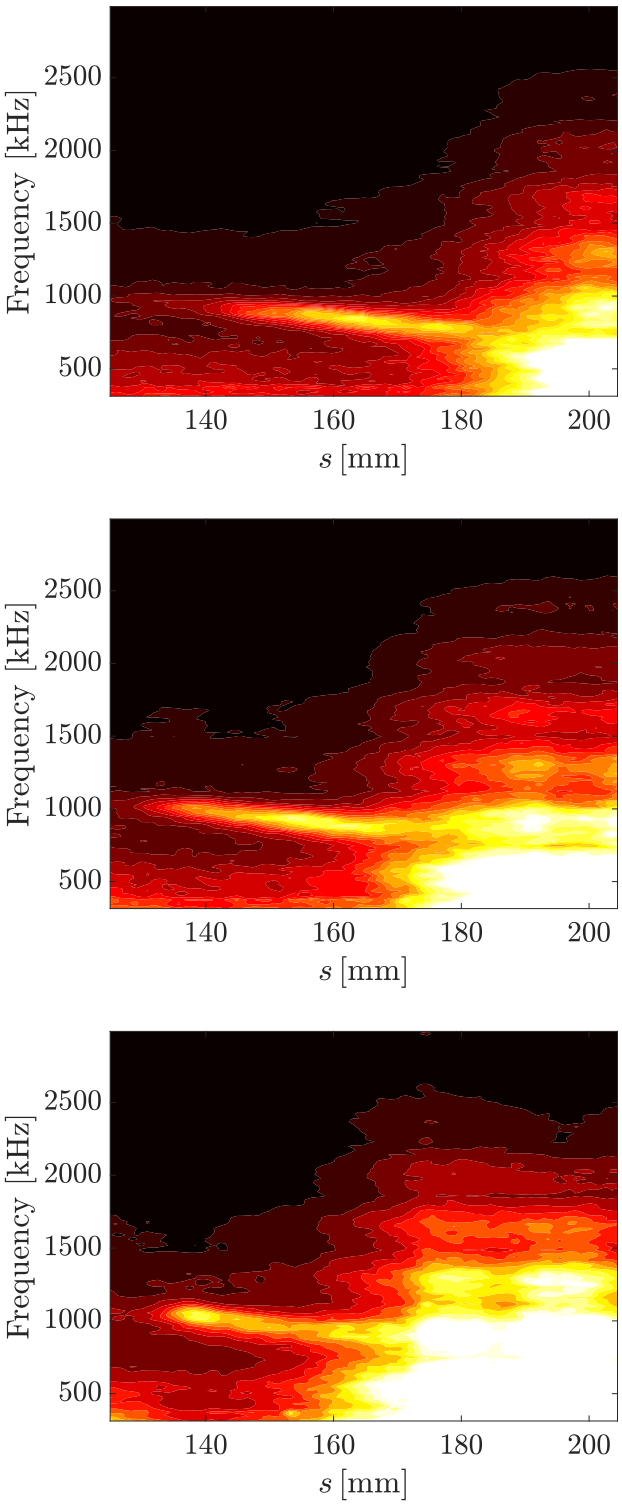

Figure 5.30: Logarithmic pixel intensity (arbitrary units) computed as a function of frequency and streamwise location for run 450 (top), run 452 (middle), and run 453 (bottom).

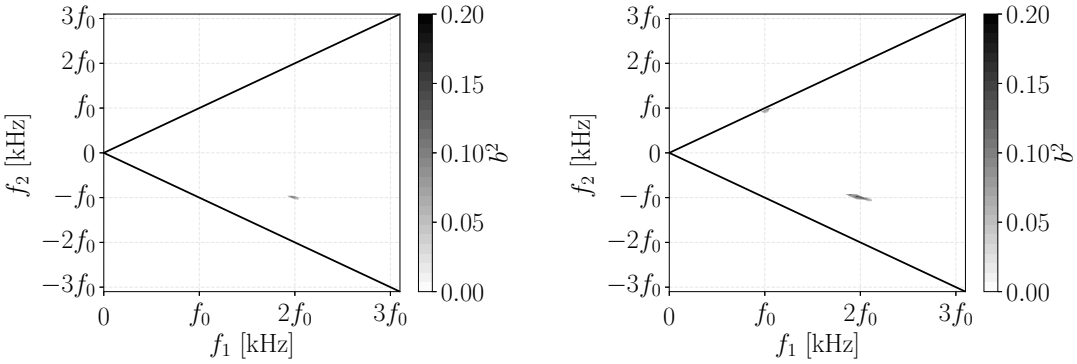

Figure 5.31: Run 453 bicoherence computed at $s = 133.3\,\text{mm}$ (left) and $s = 140.8\,\text{mm}$ (right).

Wavepacket propagation-speed error estimates based on a 95% confidence interval are provided for each experiment. This confidence interval serves as a quantification of the propagation-speed accuracy. For the purposes of this analysis, we will assume this confidence interval is also indicative of the measurement precision. To quantify the error associated with identifying the most-amplified frequency peak, a 95% peak-power threshold is defined. The left plot of figure 5.32 shows an example spectrum from AEDC T9 run 4119, with the vertical red lines identifying the frequency bounds correlating to where the second-mode peak reaches 95% of the maximum amplitude. The difference in frequency between the peak and 95% of the peak amplitude is on the order of $\pm\,4\%$ of f_0 for spectra computed upstream in the field of view and $\pm\,5\%$ of f_0 further downstream where the spectra spread slightly. In considering the extreme case, the wavepacket propagation-speed error is $\pm\,5\%$ and the error due to fitting the peak is also $\pm\,5\%$. This would result in an over or under prediction on the frequencies by roughly 7%. The right plot of figure 5.32 shows the normalized most-amplified frequencies with the error bounds plotted. It

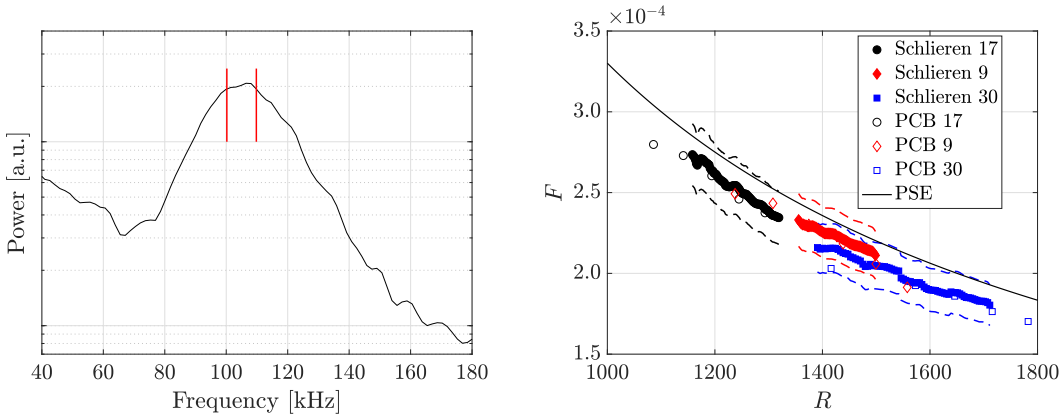

Figure 5.32: Spectrum with frequencies associated with 95% peak amplitude identified (left). Dimensionless second-mode most-amplified frequencies with error bounds computed for AFRL LT (right). The dashed lines indicate the maximum error bounds.

is important to note the agreement between the schlieren and PCB measurements, since the PCB sensors are not subject to the error associated with converting the spatial frequencies of the waves to temporal frequencies. Since good agreement is observed between the frequencies measured by both techniques, we conclude that the actual error associated with the schlieren measurements is likely significantly lower than the outlined extreme case. The peak identification is expected to have some impact on the measured amplitudes, but the assumption of constant initial amplitudes for all disturbance frequencies is expected to dominate the error associated with the computed N factors. As cited in §4.2.1, for the extreme case this is expected to introduce an error of $\Delta N \approx 0.4$.

Other contributions of error include model alignment and flow unsteadiness which can lead to discrepancies between the measurements and PSE solutions. The accuracy of the cone angle of attack is roughly 0.2° for AEDC T9 and the AFRL HRN and 0.5° for the AFRL LT. A parametric study of the influence of angle

of attack on stability characteristics is provided in Hofferth et al. (2013). They observed a change in f_0 of 6.5 – 8.4 kHz (2.5 – 3.2 % of f_0) for a 0.1° change in cone angle of attack, though caution in direct comparison is advised since their study used a flared-cone model. Using an average change of 2.8% in f_0 per 0.1° change in cone angle of attack, in the present work this introduces a maximum error into the most-amplified second-mode frequencies of 5.6% for the AEDC T9 and AFRL HRN results, and 14% for the AFRL LT results. STABL results are computed using the measured flow conditions from each experiment and as such the error should only be subject to the error in acquiring the freestream conditions.

5.5 Discussion

Using the results of this chapter, comparisons can be drawn between transition measurements acquired in each facility. The first clearly observed difference in the results are the most-amplified second-mode frequencies. Frequencies are lowest in Tunnel 9, lying in the 70 – 130 kHz range, are higher in the AFRL LT at 200 – 400 kHz, and highest in the AFRL High-Reynolds-Number facility, where they lie in the range 750 – 1100 kHz. Although this is expected due to the freestream unit-Reynolds-number effect on boundary-layer thickness, it is important to note as it plays an important role in explaining other observed behavior. A significant difference is observed in the slope of the maximum N factors between the Mach-6 and Mach-14 results. The measured slope, $\mathrm{d}N/\mathrm{d}R$, is approximately 60% higher in the AFRL LT at Mach 6 than in Tunnel 9 at Mach 14, indicating substantially

higher spatial amplification rates. Increasing saturation N factors with increasing unit Reynolds numbers are also observed in both the AFRL LT Mach 6 and Tunnel 9 Mach-14 results. Wave saturation amplitudes computed from the PCB sensors are comparable for the Mach-6 and Mach-14 waves at $\approx 30\%$ of the mean edge pressure. This result is somewhat unexpected based on the data compiled by Marineau et al. (2019): their data show weak variation of the maximum second-mode wave amplitudes at $M_e > 5.8$, but substantially lower values below that threshold. In the AFRL LT experiments, however, $M_e = 5.46$. The consequence of the comparable saturation wave amplitudes are higher saturation N factors in the Mach-6 results.

In considering the effect of Mach and unit Reynolds number on the development of waves in the nonlinear-growth regime, the relationships become less clear. Although quadratic phase locking is observed in the bicoherence plots for the Mach-6 data collected in both AFRL facilities, substantially more nonlinear interactions are observed at Mach 14, including those involving third and fourth harmonics at $4f_0$ and $5f_0$. No time-averaged results are available for the Tunnel 9 Mach-10 waves, but strong higher harmonics are visible in the wall-normal energy spectra. The reduced number of interactions in the Mach-6 High-Reynolds-Number facility results compared to the Mach-6 Ludwieg Tube results may be due to the reduced number of pixels across the boundary layer (4 versus $9-11$) which, as discussed in §5.3.1, has a significant spatial filtering effect. However, the impact of the second-mode most-amplified frequencies being 5–10 times higher may also play a role, where $2f_0 \approx 2.12\,\text{MHz}$ for the AFRL HRN run 453. With freestream noise levels scaling at roughly $f^{-3.5}$, the lower initial amplitude levels at higher harmonic frequencies may

fail to provide disturbance seed amplitudes for the harmonics to reach sufficiently large amplitudes relative to the fundamental frequency content to appear in the bicoherence analysis before the fundamental content begins to breakdown. However, the freestream noise will be at higher frequencies in the HRN facility due to the thin-wall boundary layers, and bulk viscosity effects may play a role at very high frequencies. The recorded most-amplified second-mode frequencies in the Mach-14 case are notably low at $70-90\,\mathrm{kHz}$ because of the ability to observe transition at low freestream unit Reynolds numbers enabled by the large model size. In these experiments, the higher harmonics at $2f_0$ $3f_0$, and $4f_0$ are still hundreds of kilohertz, a frequency range over which freestream noise amplitudes remain high. The number of nonlinear interactions and higher harmonics in the Mach-6 LT results falls somewhere between these two extremes. Finally, we note that the development of higher harmonics may also be a purely Mach number effect.

For individual second-mode wavepackets, minimal differences are observed between waves at similar stages of development at Mach 6, 10, or 14. Visual inspection shows qualitatively similar development from a rope-like appearance in the linear-growth regime to a highly curved appearance during late-stage nonlinear development to breakdown. Fundamental structure angles presented in figures 5.15 and 5.26 show similar shapes, but the Mach-6 waves have slightly lower angles of $115^\circ-120^\circ$ at $y/\delta=0.2-0.4$ versus $140^\circ-160^\circ$ for the Mach-10 and Mach-14 waves. Minimum wave angles are consistent across all Mach numbers in the range of 8°–15° at $y/\delta=0.85-1.0$. Similarity across Mach numbers applies to the wall-normal energy distributions as well, with the exception being the presence of harmonics

discussed in the previous paragraph. The double-peak structure of the fundamental energy content is observed for mature wavepackets of all three Mach-number waves. No near-wall fundamental energy peak, as observed by Laurence et al. (2016) at high enthalpy ($h_0 = 11.9\,\mathrm{MJ/kg}$), appears for any of the present waves at any Mach number, and it is noted that all the present experiments were performed at stagnation enthalpies of $2\,\mathrm{MJ/kg}$ or less.

Finally, we consider the spanwise pressure footprint of the second-mode waves. The two-dimensional nature of the waves is confirmed, and for each set of experiments, increasing the unit Reynolds number is observed to decrease the wave span normalized by the local boundary-layer thickness.

Chapter 6: Blunt-Nose Results

In this chapter, experimental data collected with nose tips of varying bluntness in the AFRL Ludwieg Tube and the AFRL High-Reynolds-Number facility are presented. Two regimes are explored: small nose-tip bluntness ($R_N \leq 1.524\,\text{mm}$) dominated by second-mode waves, and moderate to large nose-tip bluntness ($R_N > 1.524\,\text{mm}$) where nonmodal instabilities appear.

6.1 AFRL Ludwieg Tube Experiments[1]

6.1.1 Test Conditions

Table 6.1 presents the freestream test conditions along with cone nose-tip radii and the computed entropy-layer swallowing lengths. Visualization and surface pressure data are collected using the same experimental setup as the sharp-nose experiments. The DPLR mean flow solutions are used to compute the boundary-layer thickness. Nose tips of four different radii are tested: 0.508 mm, 1.524 mm, 2.540 mm, and 5.080 mm, or as a percentage of cone base radius ($R_N/R_b \times 100\%$), 1%, 3%, 5%, and 10%, respectively. Sample visualizations for each of the four nose-tip configurations are presented in figure 6.1, and the camera parameters are shown

[1]This material is adapted from Kennedy et al. (2019)

LT Run #	R_N [mm]	Re_∞/m [1/m$\times 10^6$]	ρ_∞ [g/m^3]	X_{SW} [m]	M_e
31	0.508	13.72	52.78	0.069	5.46
24	1.524	18.27	70.24	0.330	3.65
25	2.540	18.27	70.24	0.625	3.41
26	5.080	18.27	70.24	1.644	2.96
27	5.080	22.71	87.28	1.769	2.92

Table 6.1: Experimental conditions. X_{SW} and M_e are computed using the STABL software, and M_e refers to the edge Mach number at the center of the schlieren visualization region.

in table 6.2. Second-mode waves remain the most visible features within the schlieren visualizations for the 0.508 mm and 1.524 mm radius nose-tip configurations, though extremely weak nonmodal-growth features extending above the boundary layer are infrequently present in the section upstream of the entropy-layer swallowing length for the 1.524 mm case. For the 2.54 mm and 5.08 mm cases, elongated features appear between the computed boundary-layer and entropy-layer-edges, and second-mode waves within the boundary layer are no longer visible. The visualized features for a given model configuration and freestream condition appear to be a function of viewing location with respect to the entropy-layer swallowing length. Computational and experimental data (Laurence et al., 2012) have shown that both nonmodal-growth features and second-mode waves can exist in the vicinity of the entropy-layer swallowing length. Since our visualization region is physically constrained, and in no case captures enough of the cone to clearly visualize both behaviors at the same condition, the behaviors will be considered separately.

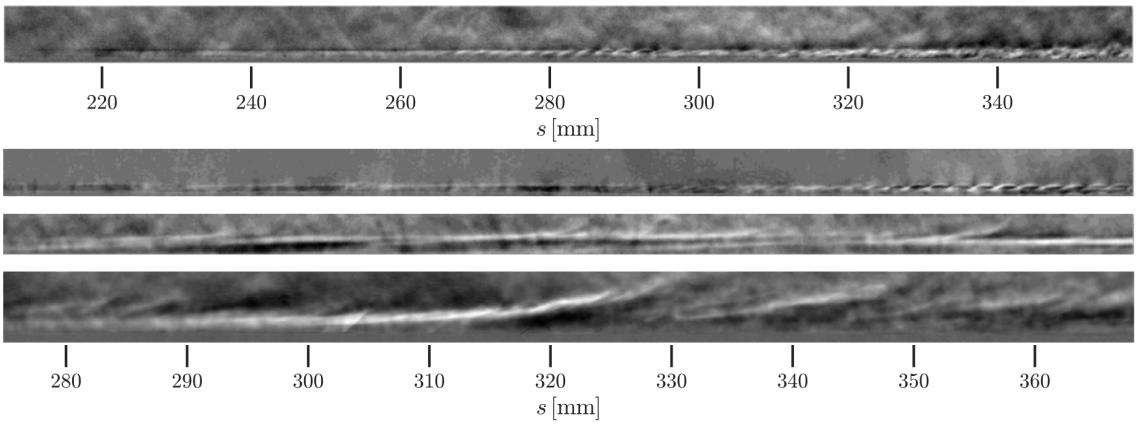

Figure 6.1: Enhanced schlieren visualizations generated by subtracting a mean flow-on image from the image of interest. Images correspond to nose-tip-radius configurations of 0.508 mm, 1.254 mm, 2.540 mm, and 5.080 mm (top to bottom).

LT Run #	Frame Rate [f.p.s]	Location s [mm]
31	287,671	207 – 358
24	368,421	275 – 368
25	368,421	275 – 368
26	234,637	275 – 368
27	234,637	275 – 368

Table 6.2: Camera parameters used for different experimental conditions.

6.1.2 Second-Mode Dominated Transition

For cone configurations with a nose-tip radius of 1.524 mm and less, the temporal reconstruction techniques outlined in §4.1 are applied. Figure 6.2 shows the most-amplified second-mode frequencies and their associated N factors for runs 31 and 24. Beginning with run 31, the frequencies computed by the PSE are observed to be $10-20\%$ higher than the PCB and schlieren frequencies across the entire measurement range. Good agreement is observed between the PCB and schlieren measurements in the upstream portion of the visualization region, but less so farther downstream. In the linear-growth regime, the slope of the N-factor curve computed from the schlieren is within 15% of that computed from the PSE. Deviation from the linear curve occurs at approximately $R = 1820$ for both the schlieren and PCB measurements, resulting in an overall maximum N factor of 6.2. The higher transition N factor here compared to any of the sharp-nose experiments is believed to be a combination of the higher unit Reynolds number and higher most-amplified second-mode frequencies resulting in lower initial disturbance amplitudes. Longer-wavelength oblique features similar to those observed by Casper et al. (2016) in schlieren visualizations over a 7° half-angle cone in a Mach-5 freestream also appear within the boundary layer, potentially introducing measurement error into the time-reconstruction technique. Turning to run 24, a significant difference is observed between the PSE frequencies and those measured from the PCB and schlieren data. Poor agreement was also found between the PSE solutions and N factors measured from the schlieren, likely due to the lower signal-to-noise ratio in the upstream por-

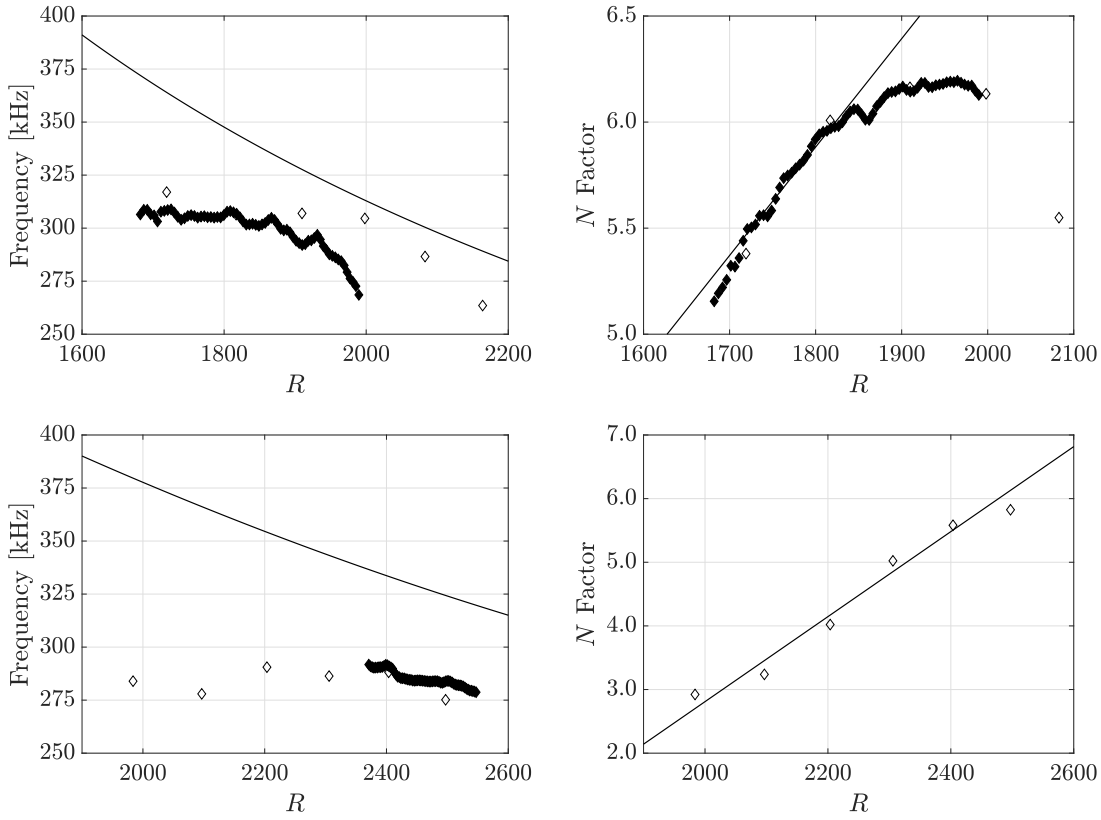

Figure 6.2: Most-amplified second-mode frequencies (left) and N factors (right) for run 31 (top) and run 24 (bottom). The filled symbols are schlieren measurements and the open symbols are PCB measurements. The black line is the PSE results.

tion of the viewing area, and thus the schlieren data are omitted from figure 6.2 (bottom right). It is noted that the entropy-layer swallowing length extends to 330 mm, just upstream of the furthest downstream PCB sensor and well past the start of the visualization region.

6.1.3 Nonmodal Growth

6.1.3.1 Visualized Features

The unsteady elongated features seen in the bottom two images of figure 6.1 first appear in the visualizations of the 2.54 mm nose-tip-radius configuration and are frequently present for the 5.08 mm nose-tip-radius configuration. The following characterization focuses on the latter case as the features are significantly more visible due to both the image magnification and viewing location. For both test conditions at this nose-tip bluntness, the predicted entropy-layer swallowing length is well past the end of the cone model, and no significant difference in visual structure is observed between the features of the two slightly different experimental conditions. In general, the features extend beyond the visual edge of the boundary layer and appear similar to the images captured by Grossir et al. (2019) using a cone with a nose tip of similar bluntness in a Mach-11.8 freestream. Unlike second-mode waves, no clear peaks appear in the PCB signal power spectra computed using the entire test time; however, as seen in figure 6.3, isolated segments of high-frequency (150 – 250 kHz) pressure content appear in the PCB signals. Matching the time stamps of these events in the PCB sensors to the visualizations reveals clearly visible elongated features believed to be associated with nonmodal growth. In this manner, we are able to identify images where features are present.

Mean observations are made by analyzing 15 clearly visible instability features present for runs 26 and 27. In agreement with what is anticipated from the amplifi-

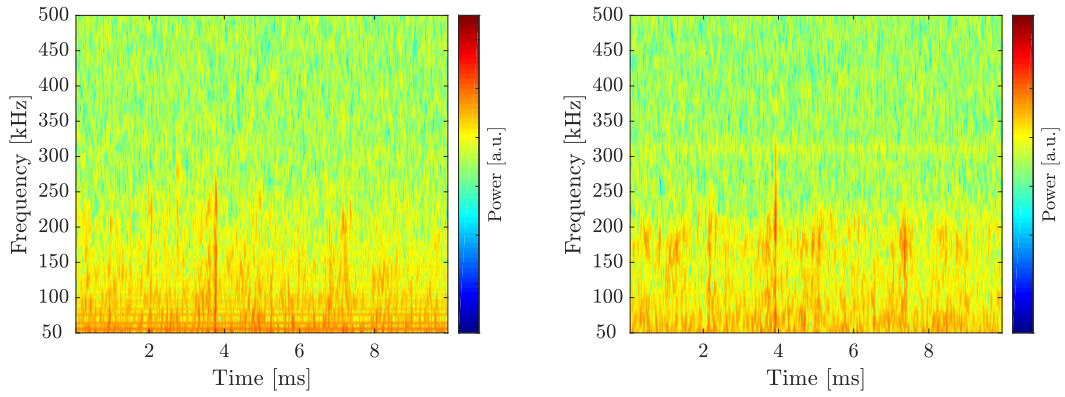

Figure 6.3: Spectrograms computed from PCB signals of run 26 at s=241 mm (left) and s=341 mm (right).

cation associated with nonmodal growth, feature development occurs slowly across the field of view, especially when compared to the rapid growth and breakdown of the second-mode instability waves. In presenting mean characteristics, we first consider the overall shape of a typical nonmodal-growth feature. Focusing on the isolated elongated features in figures 6.4 and 6.5, the features appear nearly parallel to the cone surface and gradually curve away from the surface. As the features propagate across the visualization region, the portion extending furthest into the freestream rotates downward towards the cone surface, resulting in a decrease in the inclination angle and flattening of the structure. The maximum inclination angle lies between $13-19°$ when the feature is at the most upstream end of the viewing area and decreases to $8-14°$ once the feature has propagated to the most downstream visible location. Figure 6.6 shows this evolution in feature shape by presenting the location of the maximum-intensity pixel within a single nonmodal feature using data extracted from four sequential visualizations from run 26. Select features such as that shown in the eighth image from the top in figure 6.4 also exhibit a region of

high curvature near the leading edge (downstream end). In the wall-normal direction, the features extend $2-3\delta$ above the cone surface, and the strongest density gradients are observed at a wall-normal height of $1-2.5\delta$. Qualitatively, both the experimentally observed tilting and wall-normal power distribution are consistent with the computational results of Paredes et al. (2019a) for the nonmodal growth of planar disturbances.

6.1.3.2 PCB Measurements

In figures 6.7 and 6.8 we show the PCB pressure traces associated with the image sequences presented in figure 6.4 and 6.5. Two distinct instability features are observed in the lower unit-Reynolds-number run 26 shown in figure 6.4; their associated pressure footprints are seen in the most upstream PCB sensor at $t-t_0=95\mu s$ and $t-t_0=240\mu s$. As the feature passes over the sensor, a slight rise followed by several higher-frequency (several hundred kHz) oscillations is characteristic of the pressure disturbance at the wall. A similar pressure disturbance with a frequency of 256 kHz is observed in the most upstream sensor in figure 6.8 for the run 27 disturbance. In figure 6.7, the two disturbances have a similar profile until $s=316$ mm, at which point the high-frequency content in the earlier disturbance is significantly amplified and that of the later disturbance is attenuated. By $s=341$ mm, the earlier disturbance contains extremely strong content with a frequency of approximately 182 kHz, and the later disturbance is almost completely attenuated. The rapid amplification of the earlier disturbance recorded at the two most downstream sensors

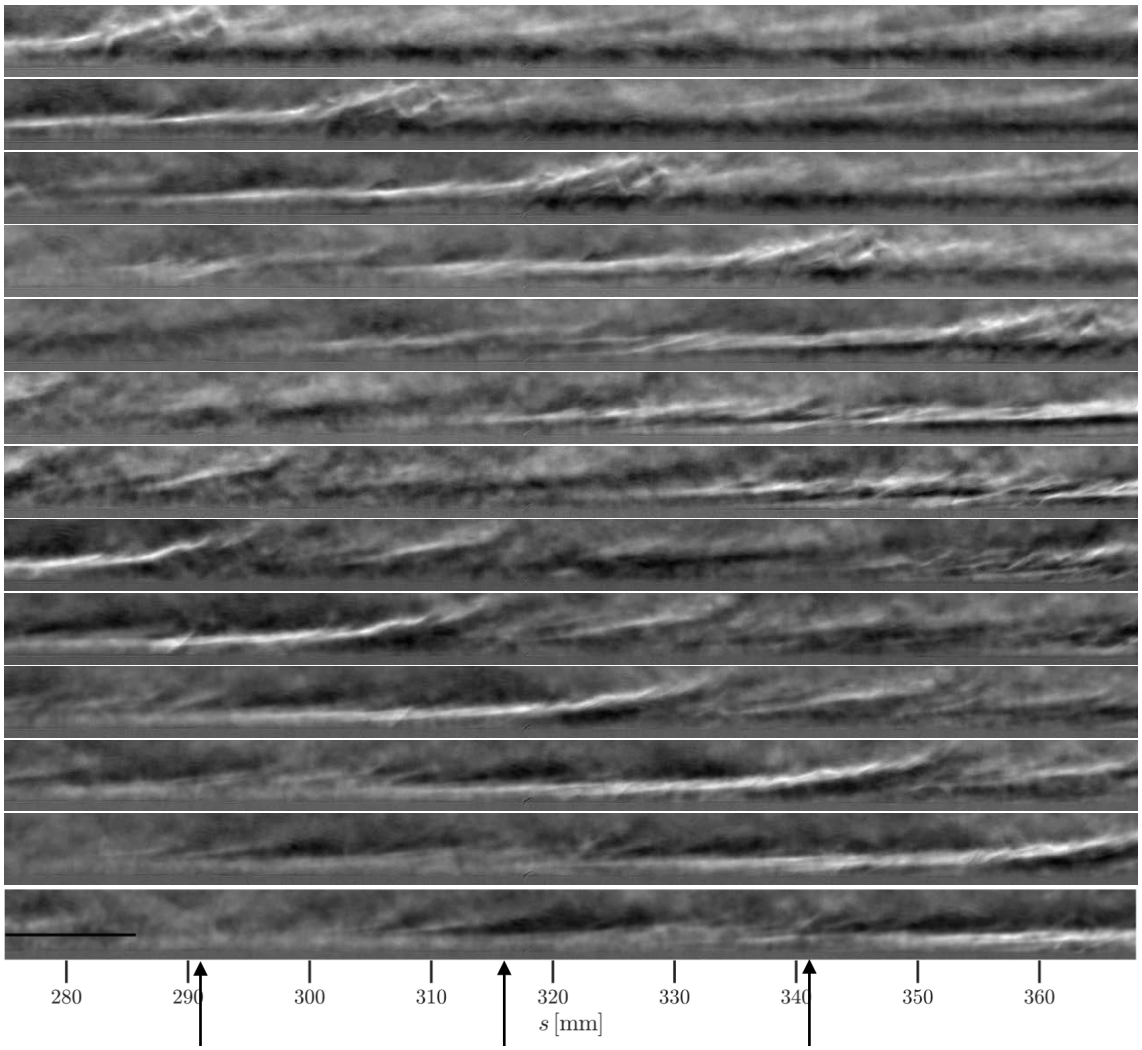

Figure 6.4: Run 26 ($R_N = 5.08\,\text{mm}$) enhanced visualization sequence. The top image corresponds to time t_0 with subsequent images separated by $21.3\mu s$ (i.e. every fifth image shown). Black arrows indicate the streamwise locations of the 3 most downstream PCB sensors, located at $s = 291\,\text{mm}$, $s = 316\,\text{mm}$, and $s = 341\,\text{mm}$. The black horizontal line in the final image indicates the computed boundary-layer thickness.

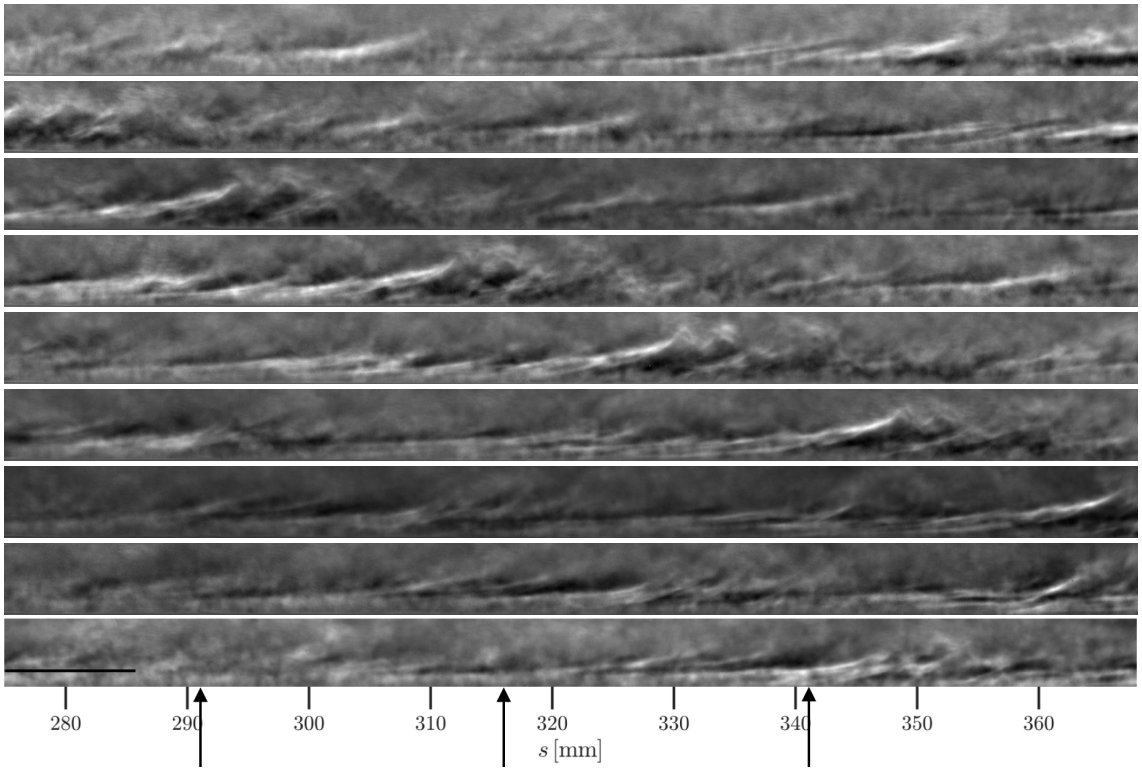

Figure 6.5: Run 27 ($R_N = 5.08\,\text{mm}$) enhanced visualization sequence. The top image corresponds to time t_0 with subsequent images separated by $21.3\mu s$ (i.e. every fifth image shown). Black arrows indicate the streamwise locations of the 3 most downstream PCB sensors, located at $s = 291\,\text{mm}$, $s = 316\,\text{mm}$, and $s = 341\,\text{mm}$. The black horizontal line in the final image indicates the computed boundary-layer thickness.

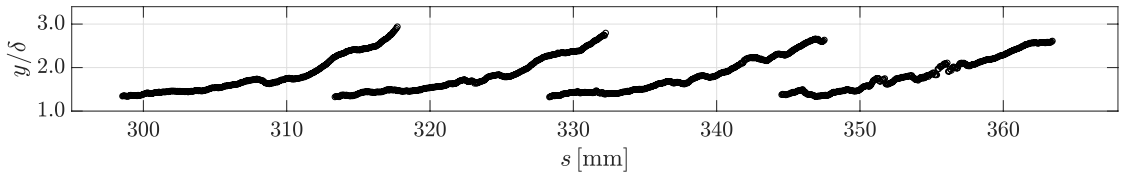

Figure 6.6: Individual nonmodal-growth feature structure as a function of streamwise location.

is an anomalous case; all other pressure disturbances appear similar in shape and magnitude up through the sensor at $s = 291\,\text{mm}$ and see minimal amplification in the more downstream sensors. Nonetheless, this unique disturbance is worth noting, as the feature appears visually similar to the other instability features. In general, the high-frequency pressure disturbances of run 27 have slightly higher frequencies than those of run 26. Given the inversely-proportional relationship between the second-mode fundamental frequencies and boundary-layer thickness, this may indicate the high-frequency pressure disturbances associated with the trailing edge of the nonmodal features are related to the second-mode.

In the bottom plots of figures 6.7 and 6.8, we show the pressure signals recorded by the PCB spanwise array associated with the two image sequences. In general, the isolated high-frequency pressure disturbances appear strongest on a single sensor in the array, with a weaker signature on one of the adjacent circumferentially offset sensors, and no discernible content on the other adjacent sensor. Beginning with run 26, the high-frequency disturbance at $t - t_0 = 200\,\mu s$ is strongest in the center sensor, with a weak pressure disturbance present in the sensors located on either side ($\xi = 5.72\,\text{mm}$ and $\xi = -5.72\,\text{mm}$). Weak content is also observed in the $\xi = -5.72\,\text{mm}$ and $\xi = 0$ sensor signals at $t - t_0 = 50\,\mu s$. Similar to the run 26 spanwise traces, the run 27 pressure disturbance at time $t - t_0 = 110\,\mu s$ is visible in both the $\xi = -5.72\,\text{mm}$ and $\xi = 0$ sensor, with minimal evidence of the disturbance in the $\xi = 5.72\,\text{mm}$ sensor. For both experiments, the coherence computed as a function of frequency identifies gives a magnitude-squared coherence estimate of $0.4 - 0.55$ for adjacent sensors. Limited coherence (~ 0.1) is observed between the $\xi = -5.72\,\text{mm}$

and $\xi = 5.72\,\text{mm}$ sensor signals, though ambiguity remains in defining the features associated with nonmodal growth using solely the pressure data due to the lack of a single distinguishing disturbance frequency. Normalized by the local boundary-layer thickness computed from the DPLR mean flow solution, this gives an estimate of spanwise extent of approximately $5-10\delta$.

While the PCB traces provide information on the pressure fluctuations in the near-wall region associated with individual features, the frequency at which the nonmodal instability features appear in the visualizations is also of interest. Extracting a dominant temporal frequency (for comparison to computational results), if present, from the visualizations requires computing both the mean feature propagation speed and spatial frequency. The mean propagation speed is computed by selecting a region of the feature located between the boundary-layer and entropy-layer edges and using a cross-correlation technique to identify the downstream propagation between sequential images. The average speed calculated over 162 image pairs from run 26 is 780 ± 90.1 m/s; values calculated for run 27 also lay within this range. The edge velocities computed for these two conditions using the DPLR mean flow solution are 761 m/s and 757 m/s, respectively. Slightly higher local experimental values are expected given that the structures extend beyond the boundary-layer edge. Inspection of the visualizations reveal a lack of clear spatial periodicity, and attempts at extracting a dominant frequency from the images failed to identify any frequency with confidence. Two possibilities exist: either the nonmodal instability features are not associated with a single dominant frequency, or the reduced schlieren contrast due to the entropy-layer combined with the integrated nature of the technique eliminates

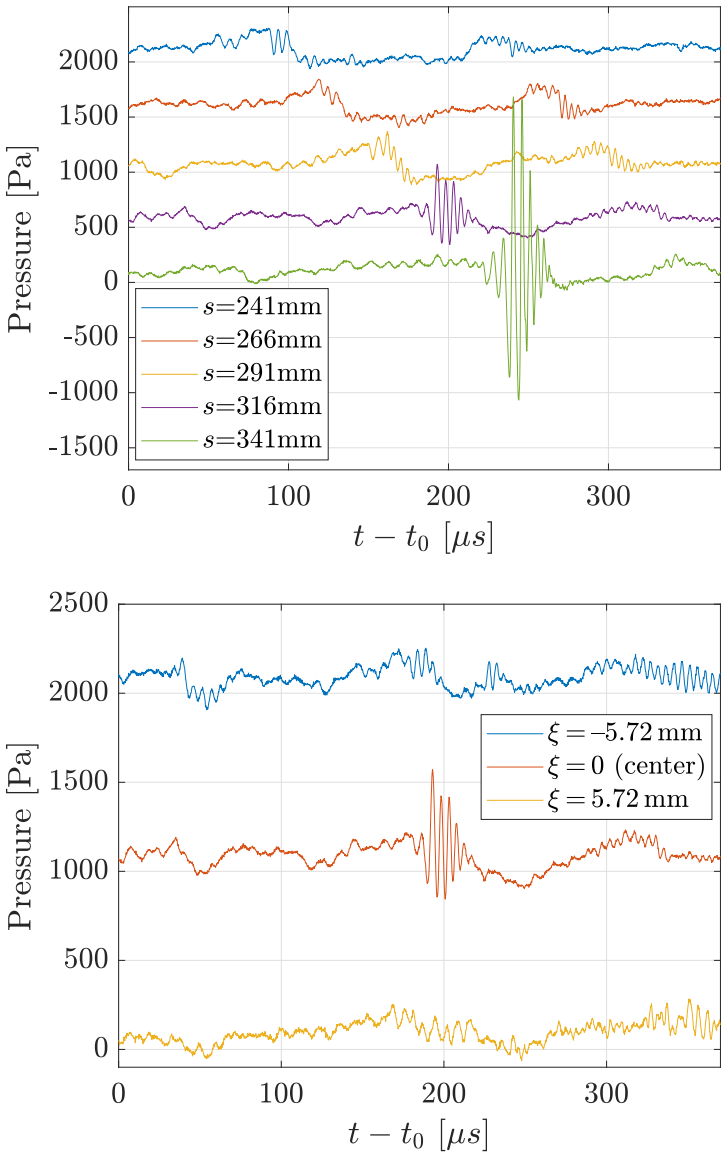

Figure 6.7: Run 26 pressure traces. PCB traces at increasing streamwise locations showing propagation of nonmodal features (top). Spanwise array pressure traces at $s = 316\,\text{mm}$ (bottom). The pressure traces are vertically offset proportional to the measurement coordinate.

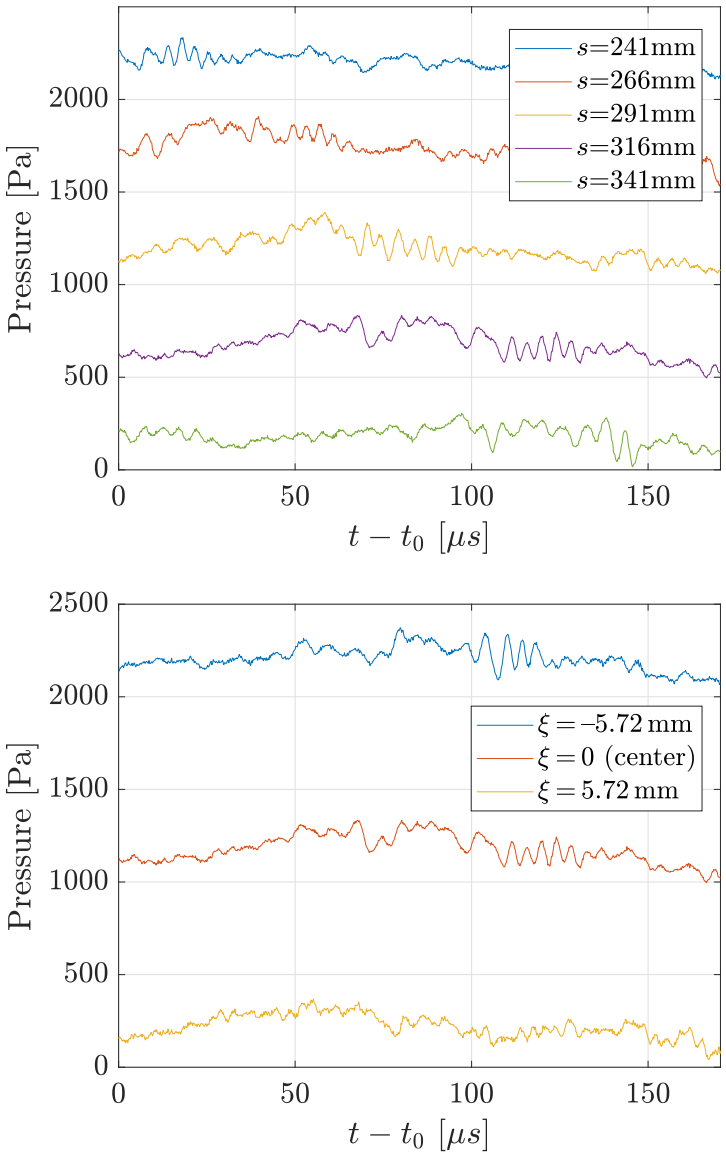

Figure 6.8: Run 27 pressure traces. PCB traces at increasing streamwise locations showing propagation of a single nonmodal feature (top). Spanwise array pressure traces at $s = 316$ mm (bottom). The pressure traces are vertically offset proportional to the measurement coordinate.

HRN Run #	R_N [mm]	p_0 [MPa]	M_∞	Re_∞/m [1/m$\times 10^6$]	ρ_∞ [g/m^3]	T_∞ [K]	u_∞ [m/s]
449	2.540	8.96	5.9	57.1	286	76.7	1038

Table 6.3: Typical facility reservoir (subscript 0) and computed freestream (subscript ∞) properties of the test conditions employed in the experiments in the AFRL High-Reynolds-Number facility.

the ability to consistently identify features. The computational results of Paredes et al. (2019b) predict the nonmodal features to exhibit amplification over a significantly broader range of frequencies than the second-mode, with the most-amplified frequencies lying in the 100 – 800 kHz range depending on the nose-tip radius and freestream conditions. Freestream noise levels, unique to each facility, may also play a significant role in which frequency disturbances become most amplified depending on their receptivity.

6.2 AFRL High-Reynolds-Number Facility Experiments

One experiment is presented from the AFRL High-Reynolds-Number facility using a cone at zero incidence with a blunt nose tip. An extremely limited number of visualizations appear to capture features similar to those observed in the AFRL LT. The schlieren setup was the same as described in §5.3.1. Table 6.3 shows the freestream conditions for the experiment presented.

An elongated feature propagating across the field of view is visible in the visualization sequence shown in figure 6.9. In addition to only having ≤ 5 pixels across the boundary-layer thickness, the low-density region generated by the entropy layer significantly reduced the schlieren contrast. Qualitatively, the disturbance

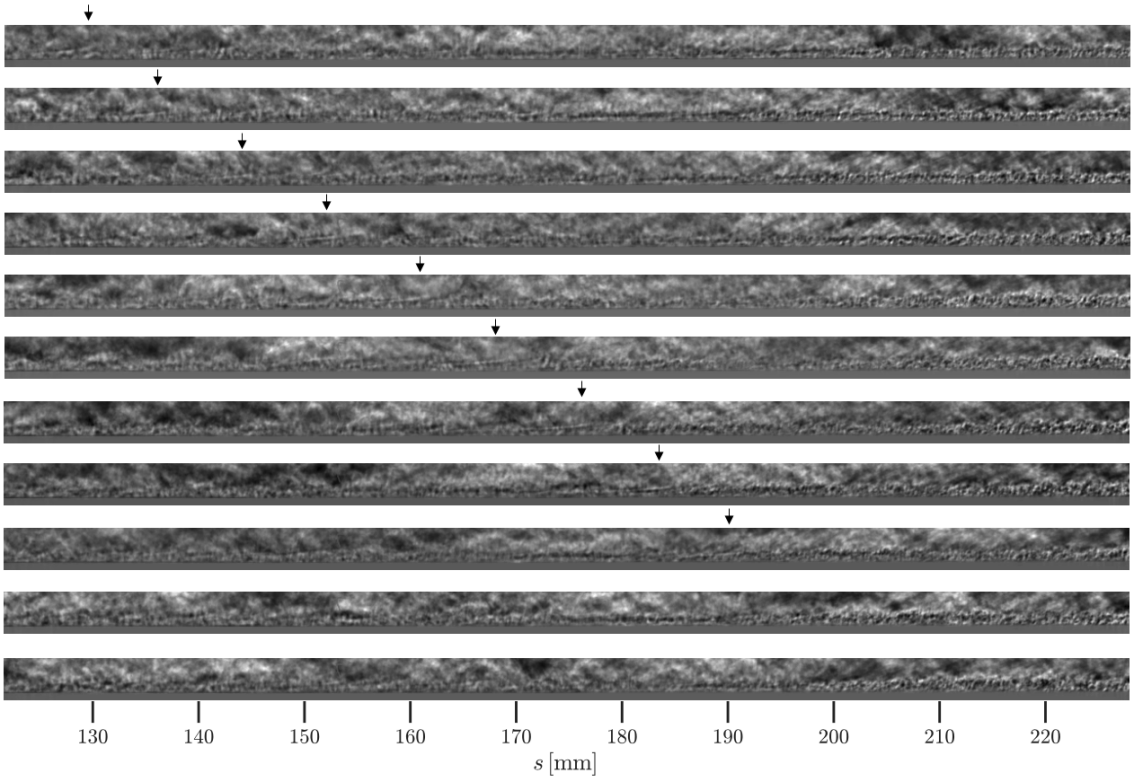

Figure 6.9: Schlieren sequence tracking an elongated feature. The black arrows identify the streamwise location of the feature in each frame before it breaks down to turbulence.

takes on the general characteristics described for those seen in the LT, extending out beyond the boundary-layer edge and being inclined downstream. At a minimum, the images confirm that similar instabilities are present in a facility with a different freestream noise profile and higher freestream unit Reynolds numbers.

Chapter 7: Conclusions

Understanding the laminar-to-turbulent transition of the boundary layer on the surface of a hypersonic vehicle is widely recognized as one of the key challenges associated with efficient high-speed vehicle design. The transition to turbulent flow increases skin friction and heat flux into the vehicle body. Thermal management is currently dealt with using massive thermal protection systems to dissipate the heat at the expense of increased mass and decreased efficiency. By better understanding the transition process and making more accurate predictions of transition location, this additional mass could possibly be reduced, leading to more efficient designs.

Previous analytical and experimental studies demonstrated the inviscid second mode to be the dominant instability mechanism leading to boundary-layer transition on slender geometries at small incidence at hypersonic Mach numbers. The second mode is characterized by fundamental frequencies of hundreds of kilohertz, and measurements of transition locations have been shown to be strongly linked to the freestream conditions. This dependence on freestream conditions has motivated the importance of measuring instability-wave properties rather than mean transition locations for the validation of computations. Extremely limited stability measurements are available in the literature at Mach 14 or above.

To investigate the effect of freestream conditions and nose-tip radius on second-mode instability-wave development, experiments were performed in three different hypersonic facilities: AEDC Tunnel 9, the AFRL Mach-6 Ludwieg Tube, and the AFRL Mach-6 High-Reynolds-Number facility. The freestream Mach numbers were 6, 10, and 14 and the facilities provided a range of unit-Reynolds-number conditions capable of producing natural transition on the model surface. A 7° half-angle slender cone with an interchangeable nose tip was chosen as the test geometry due to its canonical nature and use in an extensive amount of previous literature. PCB piezoelectric pressure sensors mounted on the surface of the cone provided supplementary high-speed pressure measurements.

A calibrated high-speed schlieren visualization system has been developed to enable non-intrusive time-resolved quantitative measurements of second-mode instability waves. By strategically optimizing the camera frame rate, field of view, and magnification, individual wavepackets were captured in multiple sequential images and provided off-wall data inaccessible by surface measurements. The system calibration was performed using a long-focal-length thin lens of known density gradient. It was shown that, when placed within the schlieren system, the lens provided a reference for generating a unique mapping of pixel intensity to density gradient. An analysis on the calibration procedure was performed to characterize the thin lens and quantify the sensitivity of the mapping to lens misalignment within the system. With careful identification of the vertical coordinate corresponding to the optical center of the lens, the calibration curve was shown to be relatively insensitive to slight optical misalignment of the lens. The calibration was shown to be easy to

implement with minimal to no modification of the schlieren system.

In order to convert the schlieren image data to a more desirable format for a time-averaged analysis, a time-reconstruction technique was developed. The technique exploits the slow evolution of the waves between sequential frames along with their roughly constant propagation speeds to reconstruct the pixel-intensity signal at a given location in space. The signals are typically generated at the wall-normal height of the maximum disturbance intensity and have a frequency resolution of $20-40$ times the camera frame rate. The high-frequency-resolution signals combined with the calibration allows for the measurement of second-mode instability wave amplitude growth and integrated amplification rates. For comparison, second-mode instability growth was computed using the parabolized stability equations as part of the STABL software suite. Good agreement was generally observed between the second-mode wave frequencies and amplitudes measured by the schlieren and PCB surface pressure transducers and those computed by the PSE results in the linear-growth regime in each experimental facility.

The time-averaged sharp-cone measurements revealed several key results. In line with the theory of Mack (1975), the slope of the second-mode maximum N-factor curves for the AFRL Mach 6 experiments was measured to be approximately 60% higher than the Tunnel 9 experiments. The Mach-6 waves attained higher transition N factors due to their lower initial amplitudes compared to the Mach-14 waves, a result that was not necessarily expected. For a given Mach number, higher freestream unit Reynolds numbers were associated with higher transition N factors due to the reduced initial amplitudes provided by the freestream noise.

Measurements acquired in the Mach-6 High-Reynolds-Number wind tunnel were the first experimental confirmation of second-mode transition in that facility, with the most-amplified second-mode frequencies measured in the range of $760 - 1060\,\mathrm{kHz}$. Of particular importance was the identification of the role of higher harmonics in influencing nonlinear wave growth. A bispectral analysis applied to the extremely high frequency resolution time-reconstructed schlieren signals revealed quadratic phase-locking of harmonic content with frequencies as high as $4f_0$ and $5f_0$. The maximum computed bicoherence of the interactions were shown to precede the maximum amplitudes of the content they described, indicating that the phase locking is more closely associated to the content amplification rate than absolute power. A larger number of interactions involving higher frequency content were observed at Mach 14 than at Mach 6; this was theorized to be a result of the different second-mode frequencies, although it may also be a Mach number effect. Increasing the angle of attack increased the second-mode most-amplified frequencies on the cone but had minimal effect on the experimentally measured N-factor slopes. Finally, besides the presence of harmonic content, the individual wave development remained fairly unchanged at different Mach numbers.

Increasing the radius of the cone nose tip resulted in the suppression of second-mode waves and downstream movement of the transition location on the cone surface. Second-mode waves no longer appeared in the visualizations for cone nose tips of $R_N \geq 2.058\,\mathrm{mm}$, for which the computed entropy-layer swallowing length was downstream of the visualization region. For the largest nose-tip radius, elongated features associated with nonmodal growth were clearly visible. The strongest insta-

bility feature content was concentrated primarily between the boundary-layer and entropy-layer edges. In general, the spatial evolution of the features was slower than the second-mode waves, consistent with their nonmodal character. Although the visualized features lacked the periodic structure of second-mode waves, simultaneously acquired surface pressure measurements revealed high-frequency content (i.e. characteristic of the second mode) associated with their trailing edge, suggesting a potential connection between the two instability mechanisms.

In considering extensions of the present work, we note that all the experiments were performed at low-enthalpy ($\leq 2\,\mathrm{MJ/kg}$) conditions. Given the demonstrated importance of wall-temperature effects on second-mode development (Bitter and Shepherd, 2015; Laurence et al., 2016) combined with the robustness of the calibrated schlieren measurement system, experiments conducted at high-enthalpy conditions would yield important computational validation results, particularly N-factor slopes, and could be used to characterize the acoustic radiation associated with the supersonic mode (Chuvakhov and Fedorov, 2016). Experiments performed in the AFRL LT with the cone installed at different angles of attack could provide additional meaningful information as well. Since the cone can be installed at a fixed angle of attack in the LT, the schlieren system can be optimized for each model configuration; this would allow meaningful data to be acquired at larger angles of attack than was possible in the T9 campaign, potentially revealing trends in the N-factor curves that did not appear clearly in the T9 data.

To improve the measurement technique, a combination of simultaneously acquired calibrated schlieren and FLDI should be considered. The FLDI system could

provide a quantitative measurement of density that can anchor the schlieren N-factor measurements and eliminate the need for the PSE results. For experiments conducted in lower freestream Mach numbers, where second-mode wavepacket propagation speeds are lower, use of a linear light source such as an LED can be considered within the schlieren system. Provided the light source produces sufficiently high-intensity, high-frequency pulses capable of freezing the flow, second-mode wave growth can be directly calculated from the pixel intensities as the schlieren response of the light rays would be linear. Finally, it may also be of interest to extend the calibration technique to be used in a focusing schlieren system. This would allow quantitative measurements from schlieren visualizations to be made of second-mode waves developing on geometries where a traditional schlieren system would fail due to its integrated nature, such as in the flat-plate experiments of Whalen et al. (2019) and Kegerise and Rufer (2016).

Appendix A: Integrated Wall-Normal Density-Gradient Profiles

We note that while the wall-normal spectra computed from the calibrated density-gradient signals provide information on the development stages of the wavepacket, the spectra computed from the density profiles may be more desirable information from the perspective of computational validation. This is particularly true when comparing to direct measurements of density such as the FLDI study performed by Parziale (2013). In order to compare the difference between the density gradient and density signals, the density-gradient distributions used to generate figure 5.13 are integrated downward from the known boundary-layer edge conditions to the cone surface. Figure A.1 presents the power spectra computed from the integrated signals at each wall-normal pixel height. A single fundamental peak is present in the integrated power spectra for all wavepackets in which a two-peak profile is present in the wall-normal density-gradient power spectra. Further, the fundamental peak of the integrated spectra occurs at the y/δ location corresponding to the wall-normal location of the valley between the two density-gradient fundamental peaks. In the case where a single peak is present in the density-gradient power spectra, a single peak is still present in the integrated signal spectra, but is located at a y/δ location further towards the boundary-layer edge. The peaks at the cone surface are believed

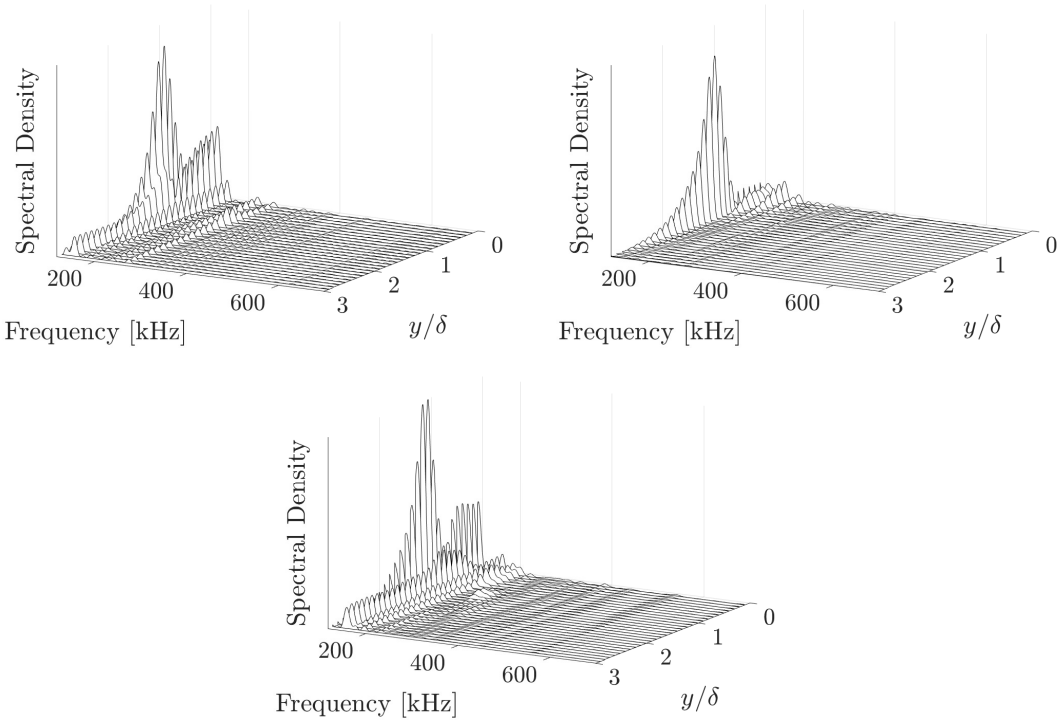

Figure A.1: Integrated wall-normal density-gradient profiles for run 4119 at $R = 1782$ (top left), $R = 1862$ (top right), and $R = 1990$ (bottom).

to be non-physical artifacts of the signal integration.

Appendix B: Schlieren Integration Effect

In this section we quantify the effect of the integrated nature of the schlieren system on the measurements. We begin by considering the effect of the cone curvature on a single wave centered on the spanwise PCB array in the AFRL LT experiments. For AFRL LT Run 9, a single wave is observed to have a circumferential extent of 3.16δ with $\delta \approx 1.4\,\text{mm}$ at the location of the spanwise array ($s = 316\,\text{mm}$). The angle, ϕ, that the wave covers on the cone surface, is defined in radians as

$$\phi = \frac{a}{R}, \tag{B.1}$$

where R is the radius of the cone at the downstream location of the spanwise array, and a is the arc length. Using $R = 38.5\,\text{mm}$ and $a = 2.21\,\text{mm}$ (one half of the wave width) to compute the change in height from the centerline to the edge of the wave, the resulting angle is $\phi = 3.29°$. We now compute the change in vertical height from the center to the edge of the packet, h, as

$$h = R\,(1 - \cos\phi), \tag{B.2}$$

which results in $h = 0.0635\,\text{mm}$, or $h = 0.045\delta$. Thus, the effect of cone curvature will have minimum impact on the measurement of a single wavepacket.

We now the consider the effect of two wavepackets present at the same streamwise location as the spanwise array, but with one wavepacket circumferentially offset from the center line of the streamwise ray by a distance equal to a single wave width as shown in schematic B.1. In this case, the arc length spanned between the two wavepacket centerlines is 6.32δ. Repeating the same analysis as above using the values $R = 38.5\,\text{mm}$ and $a = 8.85\,\text{mm}$, we arrive at a difference in center-line height of $h = 0.72\delta$. Referring to §5, in the linear-growth stage the strongest content of the most-amplified second-mode content is shown to be contained between approximately $0.7 - 0.85\delta$. Thus, any influence of the circumferential offset wavepacket would appear in the near-wall region of the schlieren visualization and is not anticipated to affect the signals reconstructed at the wall-normal location of the maximum disturbance intensity. In the case of a mature, nonlinearly evolving wave that has developed a peak at the outer portion of the boundary layer, the most-amplified content at the outer edge is located at a maximum height of 1.2δ. The influence of a circumferentially offset nonlinear wave could potentially appear in the centered wave at roughly 0.48δ, but again should have no effect on the reconstructed signal. Finally, we note that while an off-center nonlinearly-evolving wave can affect the individual wave wall-normal analysis, care is taken to perform the individual wave analysis on second-mode waves that are clearly centered on the center line of the cone and do not visually appear to be influenced by off-centered waves.

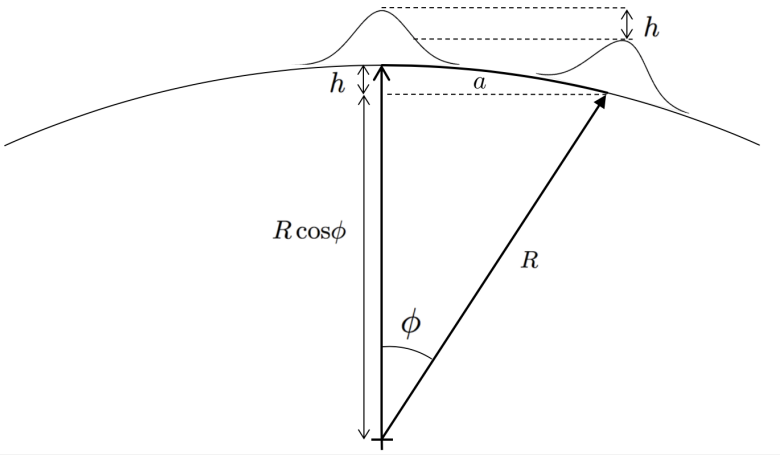

Figure B.1: Schematic of two waves present on the cone surface.

Bibliography

N.P. Bitter and J.E. Shepherd. Stability of highly cooled hypervelocity boundary layers. *Journal of Fluid Mechanics*, 778:586–620, 2015.

D.A. Bountin, A.N. Shiplyuk, and A.A. Maslov. Evolution of nonlinear processes in a hypersonic boundary layer on a sharp cone. *Journal of Fluid Mechanics*, 611: 427–442, 2008.

K.M. Casper, S.J. Beresch, and S.P. Schneider. Pressure fluctuations beneath instability wavepackets and turbulent spots in a hypersonic boundary layer. *Journal of Fluid Mechanics*, 756:1058–1091, 2014.

K.M. Casper, S.J. Beresch, J.F. Henfling, R.W. Spillers, B.O.M. Pruett, and S.P. Schneider. Hypersonic Wind-Tunnel Measurements of Boundary-Layer Transition on a Slender Cone. *AIAA Journal*, 54:8–17, 2016.

C.L. Chang, H. Vinh, and M.R. Malik. Hypersonic Boundary Layer Stability with Chemical Reactions using PSE. *AIAA Paper 1997-2012*, 1997.

N. Chokani. Nonlinear evolution of Mack modes in a hypersonic boundary layer. *Physics of Fluids*, 17:014102, 2005.

P. Chuvakhov and A. Fedorov. Spontaneous radiation of sound by instability of a highly cooled hypersonic boundary layer. *Journal of Fluid Mechanics*, 805: 188–206, 2016.

A. Demetriades. An experiment on the stability of hypersonic laminar boundary layers. *Journal of Fluid Mechanics*, 7(3):385–396, 1960.

A. Demetriades. Laminar Boundary Layer Stability Measurements at Mach 7 Including Wall Temperature Effects. AFOSR-TR-77-1311, 1977.

L. Duan, M.M. Choudhari, A. Chou, F. Munoz, R. Radespiel, T. Schilden, W. Schröder, E.C. Marineau, K.M. Casper, R.S. Chaudhry, G.V. Chandler, K.A. Gray, and S.P. Schneider. Characterization of Freestream Disturbances in Conventional Hypersonic Wind Tunnels. *Journal of Spacecraft and Rockets*, 56:2: 357–368, 2019.

G.E. Elsinga, B.W. van Oudheusden, F. Scarano, and D.W. Watt. Assessment and application of quantitative schlieren methods: Calibrated color schlieren and background oriented schlieren. *Experiments in Fluids*, 36:309–325, 2004.

A. Federov and A. Tumin. High-Speed Boundary-Layer Instability: Old Terminology and a New Framework. *AIAA Journal*, 49:1647–1657, 2011.

A. V. Federov. Transition and Stability of High-Speed Boundary Layers. *Annual Review of Fluid Mechanics*, 43:79–95, 2011.

A.W. Fiore and C.H. Law. Aerodynamic Calibration of the Aerospace Research Laboratories M=6 High Reynolds Number Facility. ARL-TR-75-0028, 1975.

K. Fujii, H. Noriaki, K. Tadao, T. Shoichi, N. Muneyoshi, I. Yukihiro, N. Akihiro, and O. Hiroshi. A Measurement of Instability Wave in the Hypersonic Boundary Layer on a Sharp Cone. *AIAA-2011-2871.*, 2011.

G. Grossir, F. Pinna, G. Bonucci, T. Regert, P. Rambaud, and O. Chazot. Hypersonic Boundary Layer Transition on a 7 Degree Half-angle Cone at Mach 10. *AIAA Paper 2014-2779*, 2014.

G. Grossir, F. Pinna, and O. Chazot. Influence of Nose-Tip Bluntness on Conical Boundary-Layer Instabilities at Mach 10. *AIAA Journal*, 57(9):3859–3873, 2019.

M.J. Hargather and G.S. Settles. A comparison of three quantitative schlieren techniques. *Optics and Lasers in Engineering*, 50:8–17, 2012.

J.W. Hofferth, R. A. Humble, and D.C. Floryan. High-Bandwidth Optical Measurements of the Second-Mode Instability in a Mach 6 Quiet Tunnel. *AIAA Paper 2013-0378*, 2013.

E.K. Jagde, R.E. Kennedy, S.J. Laurence, J.S. Jewell, and R.L. Kimmel. Visualizations of Boundary-Layer Transition on a Sharp Cone at Mach 6. *AIAA Paper 2019-3080*, 2019.

J.S. Jewell. *Boundary-Layer Transition on a Slender Cone in Hypervelocity Flow with Real Gas Effects*. PhD thesis, California Institute of Technology, 2014.

J.S. Jewell and R.L. Kimmel. Boundary-Layer Stability Analysis for Stetson's Mach 6 Blunt-Cone Experiments. *Journal of Spacecraft and Rockets*, 54:258–265, 2016.

J.S. Jewell, R.E. Kennedy, S.J. Laurence, and R.L. Kimmel. Transition on a Variable Bluntness 7-Degree Cone at High Reynolds Number. *AIAA Paper 2018-1822*, 2018.

H.B. Johnson. *Thermochemical Interactions in Hypersonic Boundary Layer Stability*. PhD thesis, University of Minnesota, 2000.

H.B. Johnson and G.V. Candler. Hypersonic Boundary Layer Stability Analysis using PSE-Chem. *AIAA Paper 2005-5023*, 2005.

H.B. Johnson, T.G. Seipp, and G.V. Candler. Numerical study of hypersonic reacting boundary layer transition on cones. *Physics of Fluids*, 10:2676–2685, 1998.

M.A. Kegerise and S.J. Rufer. Unsteady heat-flux measurements of second-mode instability waves in a hypersonic flat-plate boundary layer. *Experiments in Fluids*, 57:130, 2016.

J.M. Kendall. Wind-Tunnel Experiments Relating to Supersonic and Hypersonic Boundary-Layer Transition. *AIAA Journal*, 13(3):290–299, 1975.

R.E. Kennedy, S.J. Laurence, M.S. Smith, and E.C. Marineau. Hypersonic Boundary-Layer Transition Features from High-Speed Schlieren Images. *AIAA Paper 2017-1683*, 2017.

R.E. Kennedy, S.J. Laurence, M.S. Smith, and E.C. Marineau. Investigation of the second-mode instability at Mach 14 using calibrated schlieren. *Journal of Fluid Mechanics*, 845:R2, 2018a.

R.E. Kennedy, S.J. Laurence, M.S. Smith, and E.C. Marineau. Visualization of the Second-Mode Instability on a Sharp Cone at Mach 14. *AIAA Paper 2017-1683*, 2018b.

R.E. Kennedy, E.K. Jagde, S.J. Laurence, J.S. Jewell, and R.L. Kimmel. Visualizations of Hypersonic Boundary-Layer Transition on a Variable Bluntness Cone. *AIAA Paper 2019-3079*, 2019.

Y.C. Kim and E.J. Powers. Digital Bispectral Analysis and Its Applications to Nonlinear Wave Interactions. *IEEE Trans. Plasma Sci.*, 7:120–131, 1979.

R.L. Kimmel and J.M. Kendall. Nonlinear disturbances in a hypersonic boundary layer. *AIAA Paper 1991-0320*, 1991.

R.L. Kimmel, A. Demetriades, and J.C. Donaldson. Space-time correlation measurements in a hypersonic transitional boundary layer. *AIAA Journal*, 34:2484–2489, 1996.

R.L. Kimmel, M.P Borg, J.S. Jewell, K.Y. Lam, R.D. Bowersox, R. Srinivasan, S. Fuchs, and T. Mooney. AFRL Ludwieg Tube Initial Performance. *AIAA Paper 2017-0102*, 2017.

C.P. Knisely and X. Zhong. Sound radiation by supersonic unstable modes in hypersonic blunt cone boundary layers. I. Linear stability theory. *Physics of Fluids*, 31:024103, 2019.

S.J. Laurence, A. Wagner, and K. Hannemann. Time-Resolved Visualization of Instability Waves in a Hypersonic Boundary Layer. *AIAA Journal*, 50(1):243–246, 2012.

S.J. Laurence, A. Wagner, and K. Hannemann. Schlieren-based techniques for investigating instability development and transition in a hypersonic boundary layer. *Experiments in Fluids*, 55:1–17, 2014.

S.J. Laurence, A. Wagner, and K. Hannemann. Experimental study of instability growth and breakdown in a hypersonic boundary layer using high-speed schlieren visualization. *Journal of Fluid Mechanics*, 797:471–501, 2016.

L.M. Mack. Linear Stability Theory and The Problem of Supersonic Boundary-Layer Transition. *AIAA Journal*, 13:278–289, 1975.

E.C. Marineau, G. Moraru, D.R. Lewis, J.D. Norris, and Lafferty J.F. Mach 10 Boundary-Layer Transition Experiments on Sharp and Blunted Cones. *AIAA Paper 2014-3108*, 2014.

E.C. Marineau, G. Moraru, and D.T. Daniel. Sharp Cone Boundary-Layer Transition and Stability at Mach 14. *AIAA Paper 2017-0766*, 2017.

E.C. Marineau, G. Grossir, A. Wagner, M. Leinemann, R. Radespiel, H. Tanno, B.C. Chynoweth, S.P. Schneider, R.M. Wagnild, and K.M. Casper. Analysis of Second-Mode Amplitudes on Sharp Cones in Hypersonic Wind Tunnels. *Journal of Spacecraft and Rockets*, 56:307–318, 2019.

D. Marren and J. Lafferty. The Hypervelocity Wind Tunnel No. 9 - Continued excellence through improvement and modernization. *AIAA Paper 1998-631*, 1998.

D.J. Ort and J.J. Dosch. Influence of Mounting on the Accuracy of Piezoelectric Pressure Measurements for Hypersonic Boundary Layer Transition. *AIAA Paper 2019-2292*, 2019.

P. Paredes, M.M. Choudhari, and F. Li. Laminar-Turbulent Transition Upstream of the Entropy-Layer Swallowing Location in Hypersonic Boundary Layers. *AIAA Paper 2019-3215*, 2019a.

P. Paredes, M.M. Choudhari, and F. Li. Nonmodal Growth of Traveling Waves on Blunt Cones at Hypersonic Speeds. *AIAA Paper 2019-0876*, 2019b.

N.J. Parziale. *Slender-Body Hypervelocity Boundary-Layer Instability*. PhD thesis, California Institute of Technology, 2013.

N.J. Parziale, J.E. Shepherd, and H.G. Hornung. Observations of hypervelocity boundary-layer instability. *Journal of Fluid Mechanics*, 781:87–112, 2015.

S.R. Pate. Measurements and Correlations of Transition Reynolds Numbers on Sharp Slender Cones at High Speeds. *AIAA Journal*, 9(6):1082–1090, 1971.

J.L. Potter and J.D. Whitfield. Boundary-layer transition under hypersonic conditions. *AGARDograph*, 97:Part III., 1965.

E. Reshotko. Boundary Layer Stability and Transition. *Annual Review of Fluid Mechanics*, 8:311–349, 1976.

T. Roediger, H. Knauss, M. Estorf, S. Schneider, and B.V. Smorodsky. Hypersonic Instability Waves Measured Using Fast-Response Heat-Flux Gauges. *Journal of Spacecraft and Rockets*, 46(2):266–273, 2009.

N.R. Rotta. Effects of Nose Bluntness on the Boundary Layer Characteristics of Conical Bodies at Hypersonic Speeds. Technical report, New York Univ. NYUAA-66-66, 1966.

H. Schlichting. *Boundary-Layer Theory.* Springer, 2000.

P. Schmid. Nonmodal Stability Theory. *Annual Review of Fluid Mechanics*, 39: 129–162, 2007.

S.P. Schneider. Effects of High-Speed Tunnel Noise on Laminar-Turbulent Transition. *Journal of Spacecraft and Rockets*, 46:266–273, 2001.

G.B. Schubauer and H.K. Skramstad. Laminar-Boundary-Layer Oscillations and Transition on a Flat Plate. *NACA-TR-909*, 1948.

N.M. Shumway and S.J. Laurence. Methods for Identifying Key Features in Schlieren Images from Hypersonic Boundary-Layer Instability Experiments. *AIAA Paper 2015-1787*, 2015.

J. Sivasubramanian and H.F. Fasel. Numerical investigation of the development of three-dimensional wavepackets in a sharp cone boundary layer at Mach 6. *Journal of Fluid Mechanics*, 756:600–649, 2014.

K.F. Stetson. Nosetip Bluntness Effects on Cone Frustrum Boundary Layer Transition in Hypersonic Flow. *AIAA Paper 1983-1763*, 1983.

K.F. Stetson and R.L. Kimmel. On hypersonic boundary-layer stability. *AIAA Paper 1992-0737*, 1992.

K.F. Stetson, E.R. Thompson, J.C. Donaldson, and L.G. Siler. Laminar Boundary Layer Stability Experiments on a Cone at Mach 8, Part 1: Sharp Cone. *AIAA Paper 1983-1761*, 1983.

K.F. Stetson, E.R. Thompson, J.C. Donaldson, and L.G. Siler. Laminar Boundary Layer Stability Experiments on a Cone at Mach 8, Part 3: Sharp Cone at Angle of Attack. *AIAA Paper 1985-0492*, 1985.

W. Tollmien. Über die entstehung der turbulenz. translated as the production of turbulence. *NACA-TIM-609*, 49, 1929.

C.P. VanDercreek, M.S. Smith, and K.H. Yu. Focusing Schlieren and Deflectometry at AEDC Hypervelocity Wind Tunnel No. 9. *AIAA Paper 2010-4209*, 2010.

A. Wagner, K. Hannemann, and M. Kuhn. Experimental investigation of hypersonic boundary layer stabilization on a cone by means of ultrasonically absorptive carbon-carbon material. *Experiments in Fluids*, 54:1–10, 2013.

R.M. Wagnild, G.V. Candler, I.A. Leyva, J.S. Jewell, and H.G. Hornung. Carbon Dioxide Injection for Hypervelocity Boundary Layer Stability. *AIAA Paper 2010-1244*, 2010.

L.M. Weinstein. Large-Field High-Brightness Focusing Schlieren System. *AIAA Journal*, 31(7):1250–1255, 1993.

T.J. Whalen, R.E. Kennedy, S.J. Laurence, B. Sullivan, D.J. Bodony, and G. Buck. Unsteady Surface and Flowfield Measurements in Ramp-Induced Turbulent and Transitional Shock-Wave Boundary-Layer Interactions at Mach 6. *AIAA Paper 2019-1127*, 2019.

M.J. Wright, G.V. Candler, and D. Bose. Data-parallel Line Relaxation Method for the Navier-Stokes Equations. *AIAA Journal*, 36:1603–1609, 1998.